

2018-01-24

Characterization of the Near Plume Region of Hexaboride and Barium Oxide Hollow Cathodes operating on Xenon and Iodine

Zachary R. Taillefer
Worcester Polytechnic Institute

Follow this and additional works at: <https://digitalcommons.wpi.edu/etd-dissertations>

Repository Citation

Taillefer, Z. R. (2018). *Characterization of the Near Plume Region of Hexaboride and Barium Oxide Hollow Cathodes operating on Xenon and Iodine*. Retrieved from <https://digitalcommons.wpi.edu/etd-dissertations/44>

This dissertation is brought to you for free and open access by Digital WPI. It has been accepted for inclusion in Doctoral Dissertations (All Dissertations, All Years) by an authorized administrator of Digital WPI. For more information, please contact wpi-etd@wpi.edu.

Characterization of the Near Plume Region of Hexaboride and Barium Oxide Hollow Cathodes operating on Xenon and Iodine

by

Zachary Ryan Taillefer

A Dissertation

Submitted to the Faculty

of the

WORCESTER POLYTECHNIC INSTITUTE

in partial fulfillment of the requirements for the

Degree of Doctor of Philosophy

in

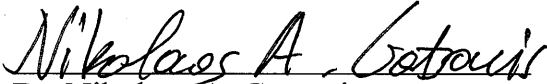
Aerospace Engineering

December 1, 2017

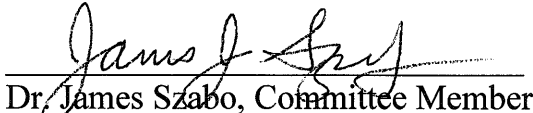
APPROVED:



Dr. John J. Blandino, Advisor
Associate Professor, Aerospace Engineering Program



Dr. Nikolaos A. Gatsonis
Professor, Aerospace Engineering Program



Dr. James Szabo, Committee Member
Chief Scientist for Hall Thrusters, Busek Co. Inc., Natick, MA



Dr. Michael A. Demetriou, Graduate Committee Representative
Professor, Aerospace Engineering Program

To my Grandmother...

“Understanding is a personal achievement, won only at the cost of constant intellectual struggle and reflection.” – Preface to *Statistical and Thermal Physics* by H. Gould and J. Tobochnik.

Acknowledgement

This research has been made possible through financial support from Busek Co. Inc., Worcester Polytechnic Institute (WPI), the Massachusetts Space Grant Consortium (MASGC), the National Aeronautics and Space Administration and the Department of Defense (DoD).

This experience has changed the trajectory of my career and my life, for that I am forever grateful to have been afforded this opportunity. I would not have been able to complete this work without assistance and support from a number of people. First and foremost, I would like to thank my advisor, Prof. John Blandino, for taking me on as a PhD candidate and his sustained support throughout the duration of this work. His guidance and seemingly limitless patience were directly responsible for my growth as a scientist, as a teacher and as a person, and the success of this research effort.

I would like to thank the members of my committee; Prof. Nikolaos Gatsonis and Prof. Michael Demetriou from WPI and Dr. James Szabo from Busek Co. Inc., for their time and valuable comments. Dr. Szabo, his guidance and commitment to experimental research demonstrated that persistence might be the best tool a researcher can have in their toolbox.

I am grateful to Vlad Hruby and the entire Busek Co. Inc. family for their support throughout my journey over the past six years. Special thanks to Lauren Lee for her continued support, guidance and encouragement throughout my time at Busek. Mike Robin, for all his help getting the cathode to operate on iodine and everything else iodine related. Chris Grenier for always keeping me honest and all his help machining parts and fabricating test setups. Dan Courtney, for his invaluable guidance and numerous discussions, and more specifically, his assistance with the uncertainty analysis for my measurements. There are so many others at Busek who always provided their assistance including, but not limited to, Surjeet Paintal, Larry Byrne, Chas Freeman, Bruce Pote, Yu-Hui Chiu and Lynn Olson.

During my time as a full time graduate student I would like to thank Barbara Edilberti, Barbara Furhman and Donna Hughes for all their help. I would like to thank WPI for three degrees, and all of the Fluids

and Plasma Dynamic Laboratory (FPDL) students and professors who I worked with throughout my years as a full time graduate student. I am grateful to Adriana Hera for her constant willingness to help me with my MATLAB code. And to Sergei Averkin, although our work together did not make it into my thesis, I appreciate all of our long lunchtime discussions and coffee breaks.

I am also grateful to Dan Asselin for getting me started in the FPDL at WPI and for his continued friendship. Although Dan moved on to another university to continue his PhD, he remained a constant source of support and encouragement, always lending an ear even though he was going through his own, similar struggles. It is difficult to overstate his contributions my growth personally and professionally.

Throughout this journey I have been fortunate to have the lifelong support of my friends and family. To my parents, thank you for everything from never missing a hockey game to helping me turn the garage into a science project construction site, you have been nothing but encouraging. My siblings, Jared and Amanda, you are two of the most inspiring people I know and are changing the world one young person at a time. You two have been more than encouraging, but rather a foundation for me to grow from—knowing that you would always be there to support me provided me great confidence.

To my grandmother, for whom this work is dedicated, I am forever indebted to you for all of the love, time and support you have given me throughout my entire life. You are the anchor that my entire support network is derived from, which gave me the ability to lead my best life. Thank you.

Table of Contents

Acknowledgement	iv
Table of Contents	vi
List of Tables	viii
List of Figures	x
List of Symbols	xv
Abstract	xviii
Chapter 1 Introduction	1
Chapter 2 Background	7
2.1 Electrostatic Propulsion	8
2.1.1 Ion Engines	8
2.1.2 Hall Effect Thrusters.....	10
2.2 Hollow Cathodes.....	12
2.3 Iodine as a Propellant for Electrostatic Thrusters	23
2.4 Plasma Physics.....	28
2.4.1 Electrodynamics and Single Particle Motion	28
2.4.2 Sheaths	32
2.4.3 Plasma Characteristics	38
2.4.4 Distribution Functions.....	39
2.4.5 Collision Processes	43
2.4.6 Iodine Literature Review	51
Chapter 3 Experimental Methods	60
3.1 Emissive Probes.....	60
3.1.1 Theory of Operation—Floating Point Technique	60
3.1.2 Uncertainty Analysis.....	63
3.2 Langmuir Probes.....	67
3.2.1 Theory of Operation.....	67

3.2.2	Plasma Density.....	70
3.2.3	Druyvesteyn Method.....	73
3.2.4	Second Harmonic Method	76
3.2.5	Uncertainty Analysis.....	78
Chapter 4	Experimental Instrumentation and Apparatus.....	84
4.1	Emissive Probe.....	84
4.2	Langmuir Probe	87
4.3	Hexaboride Cathode Experimental Setup	92
4.4	BaO Cathode Experimental Setups.....	95
4.4.1	BaO Cathode – Configuration 1.....	95
4.4.2	BaO Cathode – Configuration 2.....	100
Chapter 5	Results	103
5.1	Hexaboride Cathode Study	103
5.1.1	LaB ₆ Emitter	104
5.1.2	CeB ₆ Emitter	120
5.1.3	Discussion	124
5.2	BaO Cathode Study (Configuration 1).....	126
5.3	BaO Cathode Study (Configuration 2).....	137
5.3.1	Xenon Propellant.....	138
5.3.2	Iodine Propellant.....	141
5.3.3	Discussion	145
Chapter 6	Conclusions and Future Work.....	149
	References.....	152
	Appendix A.....	162
	Appendix B.....	178

List of Tables

Table 1: Typical operating parameters for thrusters with flight heritage [4].	12
Table 2: Physical properties of candidate propellants for electric thrusters [39].	24
Table 3: Collisional processes involving electrons in monatomic plasmas	44
Table 4: Reaction rates for a typical xenon plasma.	44
Table 5: Collisional processes involving electrons in diatomic plasmas	45
Table 6: Emissive probe measurement circuit uncertainty values based on linear regression analysis.	65
Table 7: Summary of ion collection theory criteria	73
Table 8: Voltage and current measurement uncertainty from linear least squares regression analysis	80
Table 9: Cathode properties and range of operating conditions	93
Table 10: Summary table for all cathode testing.	103
Table 11: Range of LaB ₆ cathode operating conditions.	104
Table 12: Test 1:1:1 - LaB ₆ cathode with 0.020" operating point for spot mode EEDF	115
Table 13: Calculated reaction rates for several electron-xenon processes.	117
Table 14: Plasma parameters for the LaB ₆ cathode (Test 1:1:1) operating in spot mode	119
Table 15: Plasma parameters for the CeB ₆ cathode (Tests 1:2:1 and 1:2:3) operating in spot mode.	123
Table 16: Reaction rate coefficients for the CeB ₆ cathode	124
Table 17: BaO cathode conditioning and starting procedures	127
Table 18: Complete BaO cathode testing summary.	129
Table 19: BaO cathode (Configuration 1) operating parameters on xenon and iodine.	131
Table 20: BaO cathode (Configuration 2) operating conditions on xenon and iodine	137
Table 21: Electron properties as calculated by several methods for xenon propellant	140
Table 22: Plasma density and ion collection theory criteria	140
Table 23: Reaction rate coefficients for the BaO cathode operating on xenon.	141
Table 24: Electron properties as calculated by several methods for iodine propellant.	143

Table 25: Plasma density and ion collection theory criteria	143
Table 26: Reaction rate coefficients for the BaO cathode operating on iodine	145

List of Figures

Figure 1: Schematic of a ring-cusp ion engine.....	9
Figure 2: Schematic of a Hall Effect Thruster [9]. Copyright P. Chabert and N. St. J. Braithwaite 2011..	11
Figure 3: Hollow cathode schematic [4]. Copyright 2008 John Wiley & Sons, Inc.....	13
Figure 4: Emission current density for various cathode insert materials.	16
Figure 5: Evaporation rates of LaB ₆ , tungsten and BaO-W [4]. Copyright 2008 John Wiley & Sons, Inc.	16
Figure 6: Pictures of the discharge cathode assembly at BOL (left) and after 30,000 hours of operation (right) [15].....	18
Figure 7: Illustration of xenon charge exchange collisions in the near keeper region of a hollow cathode [4]. Copyright 2008 John Wiley & Sons, Inc.	20
Figure 8: Ionization cross sections for iodine (I and I ₂) [43] and xenon [44]......	25
Figure 9: Charged particle trajectory in the presence of a uniform magnetic field top view (left) and side view (right) (adapted from [4] and [55])......	31
Figure 10: Two electronic potential energy curves showing the vibrational states associated with each electronic state [63]......	47
Figure 11: Potential energy diagram for dissociative electron attachment for products with low electron affinity [56].	48
Figure 12: Potential energy diagram for dissociative electron attachment for products with high electron affinity [62]. Copyright Alexander Fridman 2008.....	49
Figure 13: Dissociative electron attachment cross sections for several molecules as a function of energy [62]. Copyright Alexander Fridman 2008.....	50
Figure 14: Ionization cross sections of atomic iodine [43]. (Solid curve: single ionization; dashed curve: single and double ionization; open squares: experimental single ionization cross section by Hayes et al [67]; open diamonds: model potential cross section by Joshipura and Limbachiya [68]; open triangles:	

orthogonalized plane-wave Born cross sections by Bartlett and Stelbovics [69]; crosses: single ionization by Huo [70].)	52
Figure 15: Cross sections for single, double and triple ionization of I, and the total ionization cross section from 0 to 200 eV [67].	53
Figure 16: Ionization cross section of I ₂ [43]. (Solid curve: present work for single ionization; dashed curve: present work for single and double counting ionization; crosses: ECP(d) single ionization; open diamonds: model potential cross section by Joshipura and Limbachiya [68].)	54
Figure 17: Electronic excitation and ionization cross sections for molecular iodine (e ⁻ +I ₂) [66].	55
Figure 18: Dissociative electron attachment cross section for iodine [73] (Buchdahl [71] and Healy [72]).	56
Figure 19: Resonant capture peak for the formation of I ⁻ from iodine by electron impact (SF6 –for comparison) [74].	57
Figure 20: Potential energy diagram to illustrate the formation of I ⁻ from iodine by resonant capture [74].	58
Figure 21: Cross section for production of atomic halide ions from halogen molecules [75].	59
Figure 22: A schematic diagram of the sheath potential (V) and particle fluxes near an emitting surface [85].	63
Figure 23: Ideal single Langmuir probe trace.	68
Figure 24: Comparison of single Langmuir probe traces with various geometries (adapted from [88]).	69
Figure 25: Charged particle trajectory in the vicinity of the collecting probe for OML theory [89].	72
Figure 26: Second derivative of the probe current with respect to voltage, averaged (red) and with error bars.	81
Figure 27: Resulting EEDF with error bars on the experimentally measured distribution (error bars every 100 points for clarity).	83
Figure 28: Emissive probe schematic	84
Figure 29: Emissive probe setup	85

Figure 30: Emissive probe measurement circuit schematic [110]	86
Figure 31: SLP tip schematic	87
Figure 32: Single Langmuir probe and stage linear translation stages	89
Figure 33: Langmuir probe setup.....	90
Figure 34: Langmuir probe measurement circuit schematic.....	91
Figure 35: Hexaboride cathode electrical diagram	94
Figure 36: Hexaboride cathode setup showing SLP, translation stages, anode, emissive probe and cathode	95
Figure 37: Vacuum facility used for BaO cathode tests with iodine propellant.	96
Figure 38: Laboratory cathode and rectangular anode (left) used in iodine cathode tests and feed lines to cathode inside vacuum chamber comprising temperature controlled zone 3 (right).	97
Figure 39: Portion of iodine delivery system located outside vacuum chamber. Iodine reservoir (pot) and stainless (wrapped in thermal insulation) lines comprise temperature control zones 1 and 2, respectively.	99
Figure 40: Schematic showing iodine, xenon and nitrogen (purge) supplies, and electrical connections used in testing.	100
Figure 41: Laboratory BaO hollow cathode used for xenon and iodine comparison testing	101
Figure 42: Schematic of the iodine feed system and cathode.	101
Figure 43: BaO hollow cathode with iodine feed system.	102
Figure 44: Anode voltage for the LaB ₆ cathode.....	105
Figure 45: Plasma potential vs time (6 SCCM). $\phi_{mean} = 36.9 V$, $\phi_{rms} = 0.96 V$	106
Figure 46: Power Spectral Density Estimate for plasma potential (6 SCCM).....	106
Figure 47: Plasma potential vs time (1 SCCM). $\phi_{mean} = 46.2 V$, $\phi_{rms} = 8.4 V$	107
Figure 48: Power Spectral Density Estimate for plasma potential (1 SCCM).....	107
Figure 49: Plasma potential vs time (2 SCCM). $\phi_{mean} = 43.2 V$, $\phi_{rms} = 6.3 V$	108
Figure 50: Power Spectral Density Estimate for plasma potential (2 SCCM).....	108

Figure 51: Plasma potential vs time (3 SCCM). $\phi_{mean} = 40.2 V$, $\phi_{rms} = 5.26 V$	108
Figure 52: Power Spectral Density Estimate for plasma potential (3 SCCM).....	108
Figure 53: Plasma potential RMS for the LaB ₆ cathode.....	109
Figure 54: Relative plasma potential fluctuations in the near keeper region of a LaB ₆ hollow cathode operating on xenon.....	110
Figure 55: Typical Langmuir probe trace (blue) and trace with smooth function applied (red).....	112
Figure 56: Second derivative using the second harmonic method and numerical differentiation	113
Figure 57: Expanded second derivative zero-crossing.....	114
Figure 58: EEDF for LaB ₆ cathode operating in spot mode (6 SCCM) with 0.020” orifice (Configuration 1:1:1).....	115
Figure 59: Electron-xenon cross sections for elastic, excitation and ionization [44]	117
Figure 60: Linear fit to the square of the probe current	118
Figure 61: Comparison of the numerical simulation result with the plasma density along the axis of symmetry of the 20-HP cathode [116].....	119
Figure 62: CeB ₆ cathode plasma potential levels for various cathode tube orifice diameters operating on xenon.....	121
Figure 63: EEDF for CeB ₆ cathode operating in spot mode (6 SCCM) with 0.020” orifice (Test 1:2:1)	122
Figure 64: EEDF for CeB ₆ cathode operating in spot mode (2.5SCCM) with 0.040” orifice (Test 1:2:3)	123
.....	
Figure 65: BaO cathode operating on xenon propellant (left), mixture of xenon (middle) and iodine, and iodine vapor (right)	130
Figure 66: EDS interrogation locations.	132
Figure 67: EDS of Insert 1 (Test 2:1:1) along inner diameter (cut in half lengthwise).	133
Figure 68: EDS for Insert 2 (Test 2:1:2) on front face of emitter.	134
Figure 69: EDS for Insert 3 (Test 2:1:3) on inside edge of emitter.	135
Figure 70: EDS for Insert 4 (Test 2:1:4) on front face of emitter.	136

Figure 71: BaO hollow cathode in operation on xenon (left) and iodine (right).	137
Figure 72: Emissive probe voltage (plasma potential) for BaO cathode operating on xenon.....	139
Figure 73: Power Spectral Density (PSD) of plasma potential in BaO cathode plume operating on xenon	139
Figure 74: EEDF in BaO cathode plume operating on xenon	140
Figure 75: Emissive probe voltage (plasma potential) for BaO cathode operating on iodine	142
Figure 76: PSD of plasma potential in BaO cathode plume operating on iodine	142
Figure 77: EEDF in BaO cathode plume operating on iodine	143
Figure 78: Cross sections for several collisional processes for iodine.....	144
Figure 79: Lock-in amplifier front panel	179
Figure 80: Lock-in amplifier rear panel.....	179

List of Symbols

I_{sp}	Specific impulse
g	Acceleration due to gravity
T	Thrust
\dot{m}	Mass flow rate
m_p	Propellant mass
m_f	Final mass
v	velocity
c	Exhaust velocity
J_e	Electron current density
J_i	Ion current density
e	Elementary charge
k_b	Boltzmann's constant
n_0	Plasma density
n_i	Ion density
n_e	Electron density
n_n	Neutral density
T_e	Electron temperature
T_i	Ion temperature
\mathbf{E}	Electric field
\mathbf{B}	Magnetic field
q	charge
m	Electron mass
r_L	Larmor radius
v_{\perp}	Perpendicular velocity
v_{\parallel}	Parallel velocity
Z	Charge number
M	Ion mass
v_0	Bohm speed
b_0	Impact factor
f	Distribution function
C_{mp}	Most probable speed

\bar{C}	Average speed
$(\overline{C^2})^{1/2}$	Root mean square speed
v_d	Drift velocity
k	Reaction rate
A_p	Probe surface area
A_s	Sheath surface area
I_{si}	Ion saturation current
I_{se}	Electron saturation current
r_p	probe radius
A	AC signal amplitude
Q	Volumetric flow rate
V_K	Keeper voltage
I_K	Keeper current
V_A	Anode voltage
I_A	Anode current

Greek Symbols

η	efficiency
ϕ_w	Work function
ϵ_0	Permittivity of free space
ρ	Charge density
μ_0	Permeability of free space
ω_c	Cyclotron frequency
ϕ	potential
λ_D	Debye length
κ	Parameter in double sheath equation
λ	Mean free path
σ	Cross section
ϵ	energy
ϵ_d	Drift energy
τ	Mean time between collisions
ν	Collision frequency

ε_{aff}	Electron affinity
ε_{diss}	Dissociation energy
Γ	flux
Γ_i	Ion flux
Γ_e	Electron flux
ϕ_f	Floating potential
ϕ_s	Plasma space potential
ω	frequency
ϕ_m	Mean plasma potential
ϕ_{rms}	Root mean square plasma potential

Abstract

The use of electric propulsion for spacecraft primary propulsion, attitude control and station-keeping is ever-increasing as the technology matures and is qualified for flight. In addition, alternative propellants are under investigation, which have the potential to offer systems-level benefits that can enable particular classes of missions. Condensable propellants, particularly iodine, have the potential to significantly reduce the propellant storage system volume and mass. Some of the most widely used electric thrusters are electrostatic thrusters, which require a thermionic hollow cathode electron source to ionize the propellant for the main discharge and for beam neutralization. Failure of the hollow cathode, which often needs to operate for thousands of hours, is one of the main life-limiting factors of an electrostatic propulsion system. Common failure modes for hollow cathodes include poisoning or evaporation of the thermionic emitter material and erosion of electrodes due to sputtering. The mechanism responsible for the high energy ion production resulting in sputtering is not well understood, nor is the compatibility of traditional thermionic hollow cathodes with alternative propellants such as iodine.

This work uses both an emissive probe and Langmuir probe to characterize the near-plume of several hollow cathodes operating on both xenon and iodine by measuring the plasma potential, plasma density, electron temperature and electron energy distribution function (EEDF). Using the EEDF the reaction rate coefficients for relevant collisional processes are calculated.

A low current (< 5 A discharge current) hollow cathode with two different hexaboride emitters, lanthanum hexaboride (LaB_6) and cerium hexaboride (CeB_6), was operated on xenon propellant. The plasma potential, plasma density, electron temperature, EEDF and reaction rate coefficients were measured for both hexaboride emitter materials at a single cathode orifice diameter. The time-resolved plasma potential measurements showed low frequency oscillations (< 100 kHz) of the plasma potential at low cathode flow rates (< 4 SCCM) and spot mode operation between approximately 5 SCCM and 7 SCCM. The CeB_6 and LaB_6 emitters behave similarly in terms of discharge power (keeper and anode voltage) and plasma potential, based on results from a cathode with a 0.020"-diameter. Both emitters

show almost identical operating conditions corresponding to the spot mode regime, reaction rates, as well as mean and RMS plasma potentials for the 0.020" orifice diameter at a flow rate of 6 SCCM and the same discharge current.

The near-keeper region plasma was also characterized for several cathode orifice diameters using the CeB₆ emitter over a range of propellant flow rates. The spot-plume mode transition appears to occur at lower flow rates as orifice size is increased, but has a minimum flow rate for stable operation. For two orifice diameters, the EEDF was measured in the near-plume region and reaction rate coefficients calculated for several electron-driven collisional processes. For the cathode with the larger orifice diameter (0.040"), the EEDFs show higher electron temperatures and drift velocities. The data for these cathodes also show lower reaction rate coefficients for specific electron transitions and ionization.

To investigate the compatibility of a traditional thermionic emitter with iodine propellant, a low-power barium oxide (BaO) cathode was operated on xenon and iodine propellants. This required the construction and demonstration of a low flow rate iodine feed system. The cathode operating conditions are reported for both propellants. The emitter surface was inspected using a scanning electron microscope after various exposures to xenon and iodine propellants. The results of the inspection of the emitter surface are presented.

Another low current (< 5 A), BaO hollow cathode was operated on xenon and iodine propellants. Its discharge current and voltage, and plume properties are reported for xenon and iodine with the cathode at similar operating conditions for each. The overall performance of the BaO cathode on iodine was comparable to xenon. The cathode operating on iodine required slightly higher power for ignition and discharge maintenance compared to xenon, as evident by the higher keeper and anode potentials. Plasma properties in the near-plume region were measured using an emissive probe and single Langmuir probe. For both propellants, the plasma density, electron energy distribution function (EEDF), electron temperature, select reaction rate coefficients and time-resolved plasma potentials are reported. For both

propellants the cathode operated the same keeper (0.25 A) and discharge current (3.1 A), but the keeper and anode potentials were higher with iodine; 27 V and 51 V for xenon, and 30 V and 65 V for iodine, respectively. For xenon, the mean electron energy and electron temperature were 7.5 eV and 0.7 eV, with bulk drift energy of 6.6 eV. For iodine, the mean electron energy and electron temperature were 6.3 eV and 1.3 eV, with a bulk drift energy of 4.2 eV. A literature review of relevant collisional processes and associated cross sections for an iodine plasma is also presented.

Chapter 1 Introduction

In 1988, Stephen Hawking's "A Brief History of Time: From the Big Bang to Black Holes" was published, which has now sold over 10 million copies and been translated to 40 languages [1]. This underscores human curiosity in science, space and physics, and our place in the cosmos. Theoretical physics can only achieve scientific validation and verification through experimentation, which requires instrumentation to be delivered to regions of interest in space. As questions are answered and new, deeper questions are sparked, the demand for long-duration space missions to deliver scientific instruments to deep space and beyond will only grow. Sophisticated propulsion technologies are required to transport and control a spacecraft in deep space. Also, closer to Home, LEO and GEO spacecraft use is ever increasing, requiring more efficient thruster technology to keep pace.

For any space mission, the primary design parameter is the change in velocity, or delta- v (Δv), required to deliver the spacecraft to the final destination. The mission objective, propulsive method and target establish the delta- v requirement, which drives the propellant mass fraction, and subsequent propulsion system and spacecraft sizing. The overall mass of the spacecraft then determines the required launch vehicle size. Thus, propulsion system sizing and selection is critical to meet mission objectives.

In general, propulsion systems for space applications fall into two categories; chemical propulsion and electric propulsion. Chemical propulsion utilizes energy stored within the propellant to generate thrust. The internal energy is liberated through a chemical reaction (fuel + oxidizer) in a controlled fashion to generate the heated gaseous products of combustion. These hot gases then expand through a nozzle, converting thermal to directed kinetic energy to produce thrust. Chemical propulsion can provide a wide variety of thrust levels (milli-N to millions of N) and is not limited to use in a space environment. Since chemical propulsion can deliver a high thrust and operate in the atmosphere, it is used as the main propulsion type for launch vehicles.

An important propulsion performance parameter for propulsion systems is the specific impulse (I_{sp}). This represents the thrust produced per unit weight flow rate of propellant and has units of seconds in the SI system. The specific impulse (Eq. 2-12) for a monopropellant chemical propulsion system ranges from 150 to 250 sec and for a bipropellant system ranges from 300 to 470 sec [2]. A higher specific impulse means a larger momentum change can be imparted to the vehicle for a given mass propellant. The specific impulse is defined by

$$I_{sp} = \frac{T}{g\dot{m}} \quad (1-1)$$

where T is thrust, g is the constant acceleration due to gravity and \dot{m} is the propellant mass flow rate. In most cases, a high thrust corresponds to a lower specific impulse and lower exhaust velocity. Specific impulse is used to calculate the total velocity change, or delta- v , imparted on a spacecraft. This relationship is given by the *rocket equation* (1-2).

$$\Delta v = (gI_{sp}) \ln \left(1 + \frac{m_p}{m_f} \right) \quad (1-2)$$

Where m_p is the propellant mass and m_f is the final spacecraft mass. Chemical propulsion is inherently limited by the finite amount of stored energy per unit mass that can be liberated by a given reaction. This limits the amount of momentum change that can be imparted to the spacecraft and effective exhaust velocity ($c = gI_{sp} = T/\dot{m}$). Exhaust velocities for chemical propulsion in vacuum have an upper limit on the order of 6000 m/s corresponding to an I_{sp} of approximately 600 seconds [3]. For missions requiring large Δv 's a more efficient method of propulsion is necessary. Electric propulsion uses electrical energy to produce thrust. This can be achieved by using electric and magnetic fields to accelerate charged species (i.e. plasmas) or by using electric power to heat a neutral gas, which is then expanded in a nozzle to create thrust. In electrostatic thrusters, positively charged particles are accelerated to high exhaust velocities (10's of km/sec [4]) to produce low levels of thrust (0.001-2000 mN

[2]). Electric propulsion effectively decouples the stored chemical energy from the achievable exhaust velocity, which results in larger Δv 's than chemical propulsion for an equivalent change in mass.

Electric propulsion is a mission enabling technology for many missions characterized by a large delta- v , including orbiters, where deceleration and capture is required at the target. These would include missions to outer planets and their moons, and missions to asteroids and other near earth objects (NEOs) of interest. These missions would require Δv 's on the order of 10^4 to 10^5 m/sec [3]. Commercial uses also exist for electric propulsion and include orbit maintenance and orbit transfer for communication satellites, the majority of which reside in geosynchronous orbit (GEO), but populate other orbits such as low earth orbit (LEO) and polar orbits. Electric propulsion, specifically a high power cluster of Hall Effect thrusters (HET), which is a common type of electrostatic thruster, has been baselined for the NASA Asteroid Redirect Mission (ARM), which would capture and return an asteroid to trans-lunar orbit [5].

Electric propulsion covers a broad range of thrusters which use electric power to enhance or produce thrust—these are broken up into three categories based on acceleration method; electrothermal, electrostatic and electromagnetic. The focus of this thesis is electrostatic thrusters which use an electric field to accelerate ions from a plasma discharge to produce thrust. To initiate the plasma discharge and neutralize the expelled ions, electrons are supplied by thermionic electron emitters known as hollow cathodes. Hollow cathodes operate on a small fraction of the total propellant used by the main thruster to maintain a hot, electron emitting surface (thermionic emitter). Since the thruster cannot operate without a functioning hollow cathode, the sustained operation of the cathode is critical when considering the thruster, and subsequent mission, lifetime. Some common cathode failure modes have been established including electrical shorting, component erosion and poisoning of the thermionic emitter.

Common thermionic emitter materials include, but are not limited to, barium oxide (BaO) impregnated tungsten and lanthanum hexaboride (LaB_6). BaO is notoriously susceptible to poisoning by exposure to oxygen and will evaporate quickly at elevated operating temperature (1200°C), leading to potentially

short cathode lifetimes. Despite these drawbacks BaO cathodes have a long, successful flight heritage. LaB₆ is much less susceptible to poisoning and has a much lower evaporation rate at higher temperature, which allows operation at higher discharge currents than BaO. Failure modes independent of emitter type include component erosion and electrical shorts. Electrical shorts are straightforward and can be caused by mechanical failure due to shock and vibration during launch and degradation from thermal cycling. Component erosion is typically caused by evaporation and sputtering. Some areas of the cathode can exceed the evaporation temperature for the materials used, causing them to evaporate. Since the cathode operates with a small plasma discharge inside and must be near the main plasma discharge it is subject to high energy ion bombardment, leading to sputtering.

Some of the most commonly used electric thrusters rely on the ionization of a propellant in a gaseous state to generate the charged particles used to create thrust. In general, the critical criteria driving gaseous propellant selection for electric thrusters include molecular weight and ease of ionization (a large first ionization cross section at relatively low electron energy). Historically, the propellants have been limited to heavier noble gases (xenon, krypton) and other condensable propellants have been used including mercury, zinc, bismuth and cesium. Noble gases, such as xenon and krypton, are attractive because they are non-reactive, relatively heavy and easy to ionize. Because mercury is hazardous to humans, its use was abandoned due to the high risk associated with terrestrial testing. Metals such as zinc and bismuth have very high melting temperatures (419.5°C and 271.4°C, respectively) and even higher boiling points (907°C and 1564°C, respectively), making them difficult to incorporate into electric thruster architecture. Iodine however, sublimates from a solid to vapor (I₂) at modest pressures (2.8 Torr) and temperature (50°C), and is relatively heavy (126.9 amu for atomic iodine). This allows iodine to be stored as a solid at low pressure on the spacecraft, which dramatically reduces tank mass. Xenon is typically stored at very high pressure, which requires a thick-walled tank. This can contribute significantly to the spacecraft dry mass. Replacing that dry mass with propellant by using a propellant that can be stored at low pressure will directly increase the attainable Δv without increasing launch costs.

Iodine does have several drawbacks, which need to be addressed and overcome in order before its use as a viable propellant can be realized. Iodine is a member of the halogen group, thus it is highly reactive and corrosive to many spacecraft materials; however, the high vapor pressure prevents it from condensing on most spacecraft surfaces. Materials and surfaces in direct contact with iodine vapor must be made of iodine compatible materials. Iodine reactions are exacerbated at high temperature (500°C), especially those found inside hollow cathodes (greater than 1000°C). For iodine to be considered a viable alternative to state-of-the-art cathode propellants it is imperative to understand these material interactions, especially within the cathode, which is vital to electrostatic thruster operation.

This thesis presents work using three thermionic emitter materials and two propellants in hollow cathodes. To investigate the effect of orifice diameter on the near-keeper region of the plume of a hollow cathode a nominal ¼-inch cathode was used with both LaB₆ and CeB₆ emitters and xenon propellant. The plume properties for a single orifice diameter were measured for both the LaB₆ and CeB₆ emitters. The orifice diameter was varied and plume properties measured as a function of flow rate using the CeB₆ emitter. A nominal 1/8-inch cathode with BaO emitter was used to investigate the use of iodine propellant in a hollow cathode. A nominal ¼-inch cathode with BaO emitter was operated on both xenon and iodine propellants, and plume properties were measured in the near-keeper region for both propellants.

This extends prior work in the areas of cathode plume investigations and alternative propellants for electric thrusters. Specific areas of improvement include the use of new hexaboride emitter materials, near-keeper measurements for low power hollow cathodes and alternative propellants in hollow cathodes. Although LaB₆ has a long history in Russian hollow cathodes, it has only recently been adopted in the U.S for laboratory testing. Other hexaborides such as CeB₆ have some advantages over LaB₆, but have not been investigated as extensively as LaB₆. The plume studies increase the understanding of the plume properties in the near-keeper region, which has implications on performance, lifetime and erosion mechanisms. Iodine has several advantages as an alternative propellant to xenon for electric thrusters;

however it has not been used with a typical thermionic emitter used by electrostatic thrusters. Demonstrating its use with a hollow cathode would dramatically expand the applicability and viability of iodine as an alternative propellant for space missions.

This thesis is organized as follows. In Chapter 2, the relevant background is provided which is necessary for understanding of the field, diagnostic techniques used, and results. In Chapter 3, the experimental methods are described. Chapter 4 describes the experimental setups including the hollow cathodes, test facilities and diagnostic tools. In Chapter 5, the results are presented, divided into three subsections. The results and implications thereof are discussed in Chapter 6, with some considerations given to future work.

The present work fills the following knowledge gaps in current cathode research:

1. Extend hexaboride emitter use to low power cathodes, including LaB_6 and CeB_6
2. Improve the understanding of mechanisms that contribute to keeper electrode and orifice erosion
 - a. Characterize operation mode sensitivity to orifice diameter, flow rate and discharge current
 - b. Measure near-keeper electron energy distribution function (EEDF) and plasma properties in the near-keeper plume
 - c. Calculate the reaction rates for known collisional processes in the near-keeper
3. Investigate the compatibility of a typical hollow cathode emitter with alternative, condensable propellants, such as iodine
4. Improve the understanding of near-keeper plume region plasma for a cathode operating on iodine propellant
 - a. Measure the EEDF and plasma properties in the near-keeper region to determine dominant collisional processes for both xenon and iodine propellant
 - b. Calculate the reaction rates for known collisional processes in the near-keeper region

Chapter 2 Background

Robert H. Goddard first discovered the fundamental concepts of electric propulsion (EP) in 1906 [6]. It was initially believed that acceleration of electrons was the future for electric propulsion; however, with the recognition that light particles, like electrons, would have very high specific impulse and terrible system performance, it was realized that the acceleration of the ion was the practical choice.

Electric propulsion systems can be categorized by their acceleration method, which results in three categories; electrothermal, electromagnetic and electrostatic. Electrothermal propulsion uses electricity to resistively heat the working gas, increasing its enthalpy. This energy is then recovered as directed kinetic energy when the gas expands through a nozzle. Because the increase in energy is not limited by the chemical structure of the propellant, electrothermal thrusters can achieve higher specific impulse than chemical thrusters. Examples of electrothermal thrusters are the arcjet and resistojet.

Electromagnetic propulsion uses an electromagnetic force to accelerate plasma (ions and electrons) generated in a high-current discharge to produce thrust. The high current in these discharges result from the drift of charged particles. These currents interact with the magnetic field through the so-called Lorentz force. Examples of electromagnetic thrusters include the pulsed plasma thruster (PPT) and the magnetoplasmadynamic (MPD) thruster.

In electrostatic thrusters, ions are accelerated by a strong electric field created by either a set of electrodes as in a gridded ion thruster, or a strong potential gradient in the plasma as in a Hall Effect Thruster (HET). Many different methods have been used to generate the plasma in ion thrusters, including RF excitation and electron bombardment. For electron bombardment ion engines as well as Hall Effect thrusters, the electron source is a critical component. These are required not only to generate the plasma, but to neutralize the exhaust beam. Electrostatic thrusters are the focus of this chapter as ion engines and Hall Effect thrusters typically use hollow cathodes as electron sources. This chapter describes electrostatic propulsion, two flight-qualified thruster types, hollow cathode discharge physics and relevant plasma

physics topics. The chapter also reviews the history of alternative propellants for electric propulsion, with specific focus on condensable propellants for electrostatic thrusters.

2.1 Electrostatic Propulsion

To achieve thrust, electrostatic propulsion utilizes a strong electric field to accelerate ions to high exhaust velocity. Typically, an inert propellant (noble gas) is supplied to a discharge “volume” where the gas can be ionized by electron bombardment. This can either be a physically defined “discharge volume” or a region of the plasma where ionization occurs. The plasma ions are then electrostatically accelerated. The ion extraction and main discharge confinement methods distinguish the ion thruster types into two main types; ion engines and Hall Effect thrusters.

2.1.1 Ion Engines

A gridded ion thruster has three main components—the plasma generator, ion accelerator and beam neutralizer. A diagram of an electron bombardment ion thruster is shown in Figure 1. The plasma is created in the discharge volume by high-energy electron bombardment. The primary electrons for the main discharge are provided by a hollow cathode, which is described in Section 2.2. The primary electrons are accelerated to the positively biased anode along the walls of the discharge chamber. A set of permanent magnets are used to generate a so-called “ring cusp field”, which inhibits electron mobility to the anode, increasing electron residence time and the efficiency of ionization. Multi-aperture grids are used to uniformly accelerate the ions, generating a focused beam to produce thrust. The positively charged thrust beam must be neutralized to prevent spacecraft charging. The electrons to neutralize the beam are generated by a second hollow cathode outside the discharge chamber and downstream of the grids.

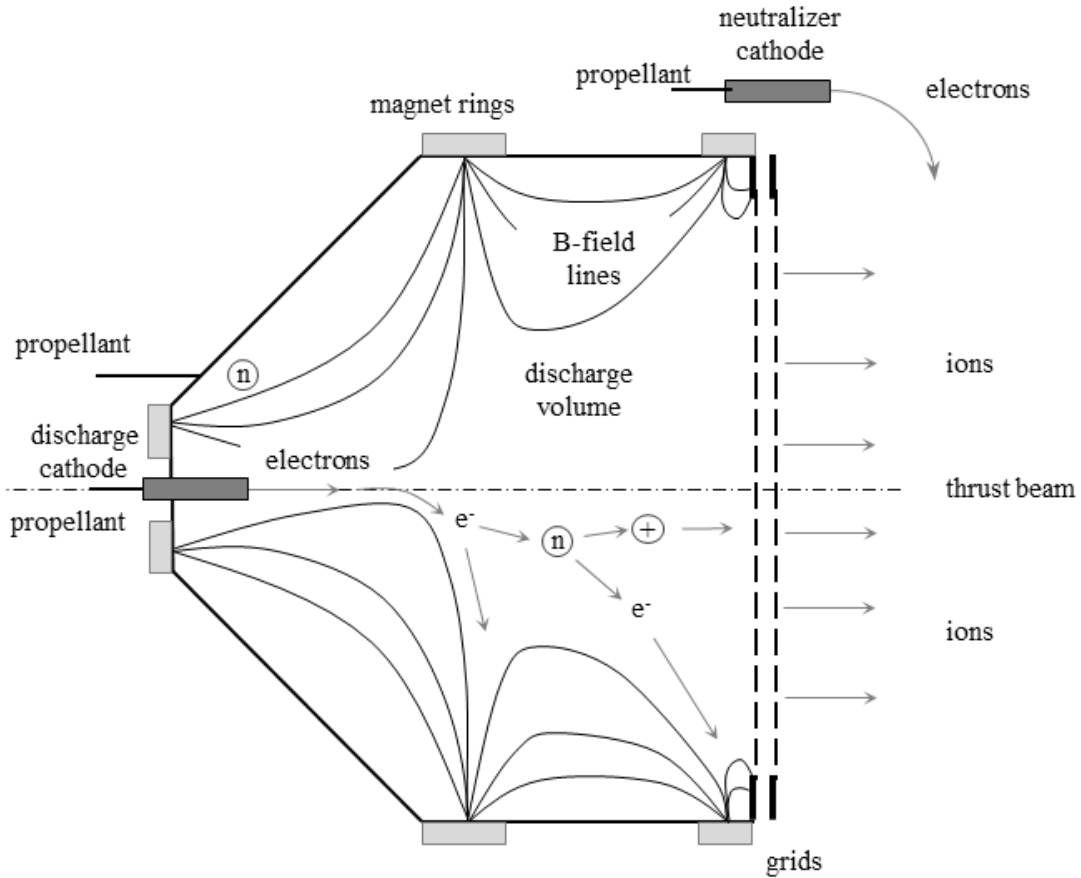


Figure 1: Schematic of a ring-cusp ion engine.

Ion engines have a rich flight heritage. Gridded ion engines were first demonstrated in the 1960s with a suborbital flight on SERT I [7] and an orbital flight on SERT II [8]. One of the first science missions using an ion engine for primary propulsion was on the NASA technology-demonstration mission Deep Space 1 (DS-1), with some of the ion engines being flown for station keeping applications for satellites in GEO [4]. More recently, the DAWN mission used an ion engine for primary propulsion to visit two large asteroids, Vesta and Ceres. Both DS-1 and DAWN used the NASA Solar Technology Application Readiness (NSTAR) ion engine. Among electric thrusters, ion engines are one of the most efficient and offer a relatively high I_{sp} . Table 1 provides typical ion engine performance data compared with other thruster types.

2.1.2 Hall Effect Thrusters

The method for generating and confining the plasma discharge is a bit more complex in a Hall Effect thruster than an ion engine, but the ions are still electrostatically accelerated. The Hall Effect thruster consists of an annular anode at the base of a cylindrical channel, a primarily radial magnetic field across the channel and an external hollow cathode. The neutral propellant is injected into the thruster through the circular anode so that it is evenly distributed throughout the cylindrical channel. The anode is electrically biased, which generates a primarily axial electric field between the cathode and anode. The hollow cathode provides the primary electrons used to initiate the plasma discharge. The electrons are attracted to the electrically biased anode, but their axial mobility is reduced by the radial magnetic field. The radial magnetic field and perpendicular electric field ($\mathbf{E} \times \mathbf{B}$) “trap” the electrons causing them to travel in the azimuthal direction around the channel, generating the Hall current from which the thruster gets its name. This enhances propellant utilization since the electron residence time in the channel increases, resulting in many collisions before the electrons can reach the anode. The ions are accelerated away from the thruster by the axial electric field generated by the anode and enhanced by the space-charge of the plasma, which creates the thruster beam. The beam space charge is neutralized by primary electrons emitted by the hollow cathode, a fraction of which are attracted to the beam and neutralize it. The electrons diffusing across the magnetic field lines, traveling along a helical path around the annular channel due to the *Lorentz Force* (2-8) are known collectively as the *Hall current*. Figure 2 shows the schematic cross section of a typical Hall Effect thruster and illustrates the Hall current generated by the crossed electric and magnetic fields.

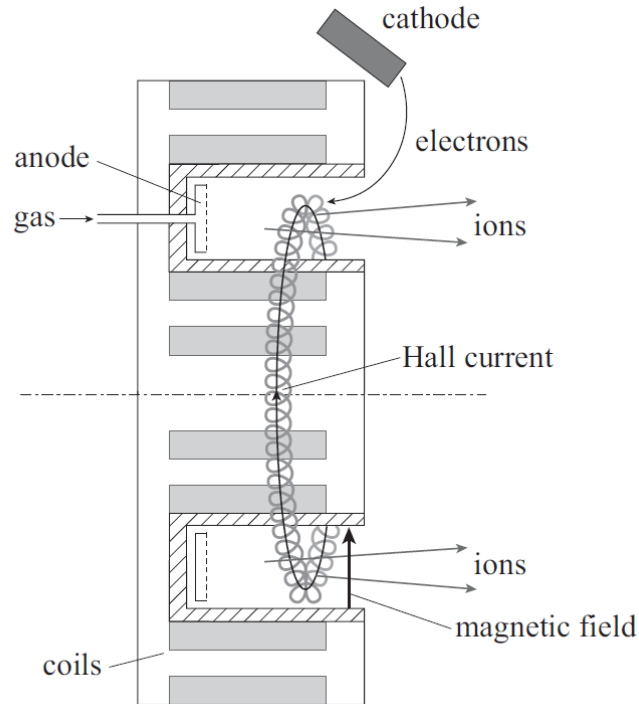


Figure 2: Schematic of a Hall Effect Thruster [9]. Copyright P. Chabert and N. St. J. Braithwaite 2011

The first U.S. Hall Effect thruster to fly in space was the BHT-200 on TacSat-2 for a technology demonstration mission in 2006. HETs have been used longer and more extensively by Russia than the U.S., mainly in station-keeping operations [4]. Hall Effect thrusters produce a higher thrust for a given power level compared to ion engines; as a result they have a lower I_{sp} . Typical Hall Effect thruster performance is compared to other standard propulsion types in Table 1 below. For a detailed history of ion engines and Hall Effect thrusters see *Fundamentals of Electric Propulsion, Chapter 9* [4].

Table 1: Typical operating parameters for thrusters with flight heritage [4].

Thruster Type	Specific Impulse (sec)	Input Power (kW)	Efficiency Range (%)	Propellant(s)
Cold Gas	50-75	—	—	N ₂ , NH ₃ , Freon, He
Chemical (monopropellant)	150-225	—	—	N ₂ H ₄ , H ₂ O ₂
Chemical (bipropellant)	300-450	—	—	Various
Resistojet	300	0.5-1	65-90	N ₂ H ₄
Arcjet	500-600	0.9-2.2	25-45	N ₂ H ₄
Ion Engine	2500-3600	0.4-4.3	40-80	Xenon
Hall Effect Thruster	1500-2000	1.5-4.5	35-60	Xenon
PPTs	850-1200	<0.2	7-13	Teflon

2.2 Hollow Cathodes

In early electrostatic thrusters, tungsten filaments were used to provide seed electrons for the discharge and thrust beam neutralization; however, due to the high operating temperature (~2600K) required for sufficient emission current density ($>1 \text{ A/cm}^2$), filaments were prone to failure [4]. A more efficient, robust, low power electron source is the hollow cathode with thermionic insert. As mentioned in previous sections, hollow cathodes are the standard electron source in current ion engines and Hall Effect thrusters. The cathode consists of a thermionic insert or emitter, cathode tube with restricting orifice, a heating element and keeper electrode. A schematic of a typical cathode is shown in Figure 3.

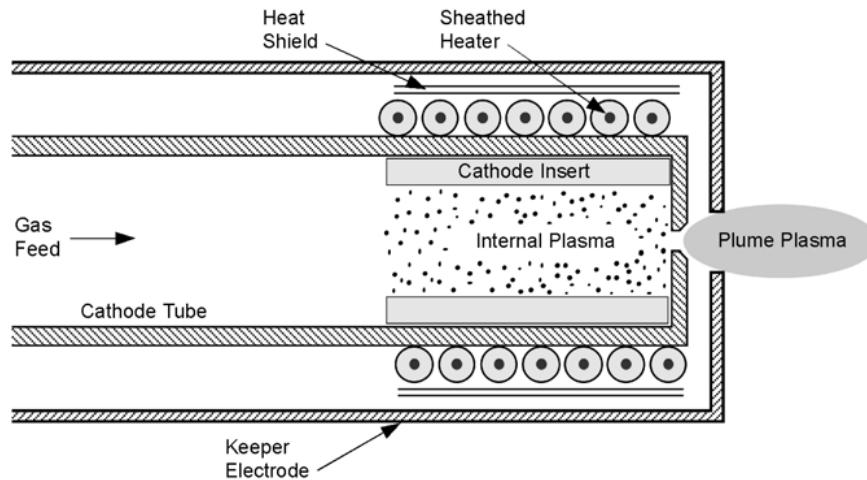


Figure 3: Hollow cathode schematic [4]. Copyright 2008 John Wiley & Sons, Inc.

The cathode tube houses the insert, and is wrapped with a coiled heater. The heater typically consists of a swaged tantalum wire with mineral insulation between the inner conductor and a grounded outer sheath. The insert can be made of several low work function materials, including barium oxide (BaO), lanthanum hexaboride (LaB_6), cerium hexaboride (CeB_6) and electride (C12A7). The cathode tube provides an orifice that restricts the propellant flow and maintains a static pressure in the insert region of a few torr (1-50 Torr) [4]. The keeper electrode extracts electrons from the insert plasma and “starts” the cathode with electric field penetration to the insert surface and aides in the maintenance of the internal plasma.

The heater is used to elevate the insert to emission temperatures. Propellant is fed through the cathode tube and ionized by the electrons leaving the insert surface. The keeper electrode is positively biased with respect to the cathode tube and extracts electrons from the internal plasma. Once an internal plasma has been established and has electrically coupled to the keeper, the heater can be turned off. The heat from the plasma is sufficient to sustain insert surface temperatures required for continuous thermionic electron emission. During thruster operation, the keeper may also be turned off and the positive space-charge in the beam serves as a virtual anode to provide extraction of electrons from the internal cathode plasma. The heat from the plasma is transferred to the insert by three mechanisms; electron, ion and

resistive/orifice heating. Electron and ion heating is a result of electrons or ions, respectively, falling through the plasma sheath and impacting the insert surface.

The electrons for the internal plasma are thermionically emitted from a low-work function material whose current density can be calculated using the modified Richardson-Dushman equation:

$$J = DT^2 e^{-e\phi_w/k_b T} \quad (2-1)$$

where D is a material-specific constant, T is the material temperature in kelvin, e is elementary charge, k_b is Boltzmann's constant and ϕ_w is the work function. A key feature of the hollow cathode is the presence of an internal plasma sheath at the surface of the emitter (between the "cathode insert" and "internal plasma" in Figure 3), which effectively lowers the material's work function due to the strong electric field. This phenomenon, known as the Schottky effect, is described by Equation 2-2.

$$\phi_{eff} = \phi - \sqrt{\frac{e|E|}{4\pi\epsilon_0}} \quad (2-2)$$

Here, ϕ_{eff} is the effective work function, ϵ_0 is the permittivity of free space and $|E|$ is the magnitude of the electric field. The magnitude of the electric field, based on an analysis of the double sheath that will form can be calculated using the following equation [10].

$$|E| = \sqrt{\frac{nkT_e}{\epsilon_0}} \left(2 \sqrt{1 + 2 \frac{eV_p}{k_b T_e}} - 4 \right)^{1/2} \quad (2-3)$$

The Schottky effect should be combined with the modified Richardson-Dushman equation when calculating emission currents from specific cathode geometries, but is not necessary for order-of-magnitude estimates. Figure 4 shows the emission current density, calculated using the Richardson equation for several common emitter materials. As a general rule, 10 A/cm² is a good guideline current

density for a sustained hollow cathode discharge [4]. Based on Figure 4, that guideline gives an emitter temperature of $\sim 1200^{\circ}\text{C}$ and $\sim 1600^{\circ}\text{C}$ for BaO and hexaboride emitters, respectively.

In a dispenser cathode, the insert is a porous tungsten matrix impregnated with BaO:CaO:Al₂O₃ mixture, typically in a stoichiometric ratio of 4:1:1 or 6:1:2. This material is able to provide useful current densities ($\geq 10 \text{ A/cm}^2$) at relatively low surface temperatures – 1000 to 1200°C [11]. Barium oxide (BaO) hollow cathode theoretical lifetimes are heavily influenced by the low work function thermionic emitter chemistry and evaporation of the emissive material from the porous refractory metal. Low energy electrons are liberated from a barium-on-oxide monolayer on the surface of porous tungsten through heating. The porous tungsten is impregnated with a BaO:CaO:Al₂O₃ mixture which provides the barium monolayer through chemical reactions. Barium and barium oxide continuously evaporate from the emitter surface at emission temperatures, but are replenished at the surface by the impregnate. The replenishment requires two processes: barium is generated by a reaction with tungsten and the barium must diffuse to the surface. Once the emitter can no longer supply enough electrons to the discharge, either from an increase in the emitting surface work function or sufficient barium evaporation, the cathode will no longer function. Figure 5 shows the evaporation rates of two emitter types and tungsten as a function of current density. LaB₆ evaporation rates are, in general, based on the temperature of emitter and simple evaporation of the material off of the emitter surface. LaB₆ performs better than BaO at higher current densities since it does not rely on any chemical reactions to evolve the low work function material via evaporation and deposition.

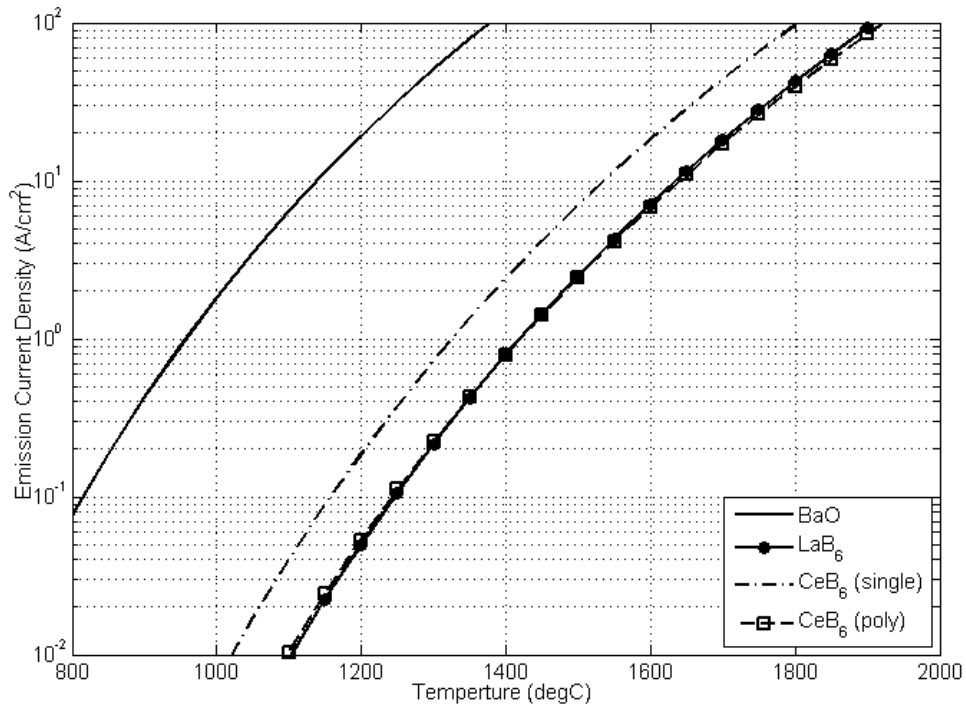


Figure 4: Emission current density for various cathode insert materials.

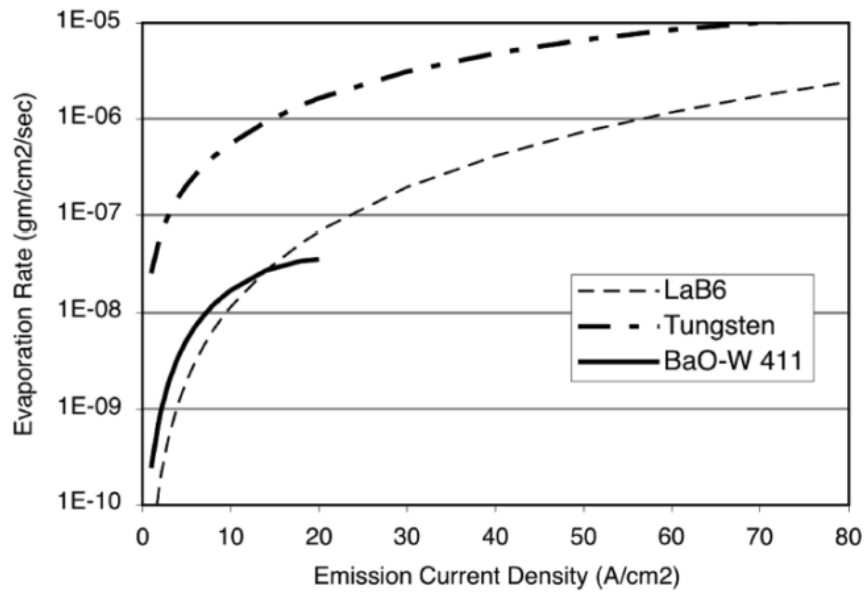


Figure 5: Evaporation rates of LaB₆, tungsten and BaO-W [4]. Copyright 2008 John Wiley & Sons, Inc.

BaO-W emitters are susceptible to oxygen poisoning, which imposes special handling requirements during testing and spacecraft integration [4]. This becomes crucial in the laboratory environment where trace amounts of oxygen and water vapor can leak into the cathode feed system, destroying the cathode. Leak checking and other measures can be taken, but it still remains a risk. This also requires, expensive, very high purity (99.999+%) propulsion grade xenon, which can be quite expensive for some universities and small labs. LaB₆ can tolerate up to two orders of magnitude higher partial pressures of oxygen and water vapor than BaO in the working gas [12]. This allows for lower grades of xenon (or even alternative propellants) to be used and mitigates the risk of failure on orbit from inadvertent exposure to oxygen during preliminary ground testing or in flight (much less likely).

LaB₆ does however suffer from boron diffusion at high temperatures where LaB₆ operates. Typically, hollow cathode tubes and orifices are made from refractory metals, which will absorb the boron, embrittling the material and ultimately leading to breakage and failure. LaB₆ is also prone to fracture due to thermal and/or mechanical shock. To prevent boron diffusion into surrounding refractory metals fine grain carbon is used between the LaB₆ emitter and any refractory metals. LaB₆ and graphite also have similar coefficients of thermal expansion (CTE), which reduces the thermal stresses on the LaB₆ from thermal cycling [12].

As the hollow cathode is the electron source for the electrostatic thruster, it is a principle point of failure and its lifetime is one major factor in the total lifetime of the thruster, and subsequent mission. Other common failure modes for cathodes besides poisoning and evaporation of the low work function emitter material include tungsten migration (in BaO cathodes) [13], and erosion of the cathode orifice and keeper electrode [4].

Erosion of the cathode orifice and keeper electrode were identified as principle failure modes in the subsequent analysis of the extended life test (ELT) of the spare NSTAR ion engine used in NASA's Deep Space 1 (DS-1) mission [14]. DS-1 was NASA's first mission using ion engines as the primary

propulsion system. A spare propulsion unit was made and used for ground-based life testing, operating almost continuously for a total time exceeding 30,000 hours. Post-test analysis included a rigorous investigation of the discharge and neutralizer hollow cathodes.

The cathode was periodically investigated during the ELT, and beginning around 5000 hours, erosion of the keeper electrode due to sputtering was observed. Erosion of the keeper electrode persisted throughout the remainder of the ELT to the point where the entire face of the keeper had been eroded away, exposing the cathode tube and heater to ion bombardment. Ultimately, an electrical short between the keeper electrode and cathode body developed [15]. Figure 6 shows the discharge hollow cathode assembly at the beginning and end of the ELT.

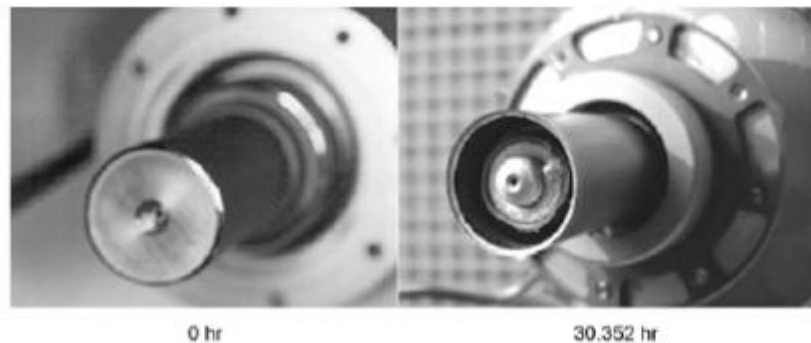


Figure 6: Pictures of the discharge cathode assembly at BOL (left) and after 30,000 hours of operation (right) [15].

The findings following the ELT launched an investigation into the possible erosion mechanisms since the erosion rates of the keeper electrode were much higher than expected. Based on cathode models and experimental analysis at the time, ion energies in the cathode plume were thought to be too low for the sputter rates observed. Several proposed mechanisms for the accelerated erosion rates emerged after the ELT. Since sputtering is the process where material is removed by particle (ion) impact with the surface, these mechanisms naturally focused on identifying sources of high energy ion production.

One proposed mechanism for the generation of high energy ions is the existence of a potential hill just downstream of the keeper exit plane, in the “near keeper plume” [16]. It is reasonable to assume a

potential hill could exist due to the expansion of the high density plasma as it exits the cathode/keeper and resulting relative speeds of ions and electrons. The existence of a potential hill just downstream of the keeper exit has been confirmed by several investigators including Katz [17] and Herman [18].

It is well established that hollow cathode operate in two distinct modes; plume mode and spot mode. Spot mode is characterized by quiescent operation and relatively low power. In spot mode the plasma potential and discharge power (anode voltage) is quite stable. Plume mode is characterized by relatively large fluctuations in the plasma potential and higher-than-nominal discharge power. The onset of plume mode is gradual and can be induced if the required current is too high for a given propellant flow rate. Thus, plume mode can be induced in the laboratory either by reducing the cathode flow rate for a fixed discharge current, or increasing the discharge current at fixed flow rate. In plume mode, large oscillations in the plasma potential have been observed, well exceeding the discharge voltage and even coupling to laboratory discharge power supplies [19]. The spot-to-plume mode transition, for a given cathode discharge current or flow rate can be adjusted by changing the cathode orifice diameter. This adjustment can lower the flow rate where plume mode is induced for a given discharge current, or vice versa—it will not eliminate the possibility of operation in plume mode entirely.

Due to the large fluctuations in the plasma potential, operation in plume mode can lead to the production of high energy ions with energies well above the discharge voltage. The potential hill and plasma potential fluctuations alone were not enough to explain the high-energy ion population necessary for the observed erosion rates [4]. It is postulated by Katz [20] that this mechanism for high energy ion production could be enhanced by charge-exchange collisions occurring at the cathode exit in the near-keeper plume.

This charge exchange process is illustrated below in Figure 7. There exists a large on-axis potential dip downstream of the hollow cathode exit driven by high neutral density. Xenon ions “see” this potential structure and are accelerated down the potential well. It is likely, due to the high neutral density, that

these ions will collide with neutrals, some of these collisions could be charge exchange (CEX) collisions. In a CEX collision the incident ion retains much of its initial kinetic energy after the collision; however, charge is exchanged resulting in a fast neutral and slow ion. In this scenario, to explain the radial high-energy ions the fast neutrals are assumed to undergo another charge exchange collision as they move radially, where they are “reionized” maintaining the energy gained from falling through the original potential well, plus the energy from the plasma potential where they were reionized. It is also possible that the fast neutral continues on after the first CEX and impacts the keeper face, but these would not be relatively high energy impacts.

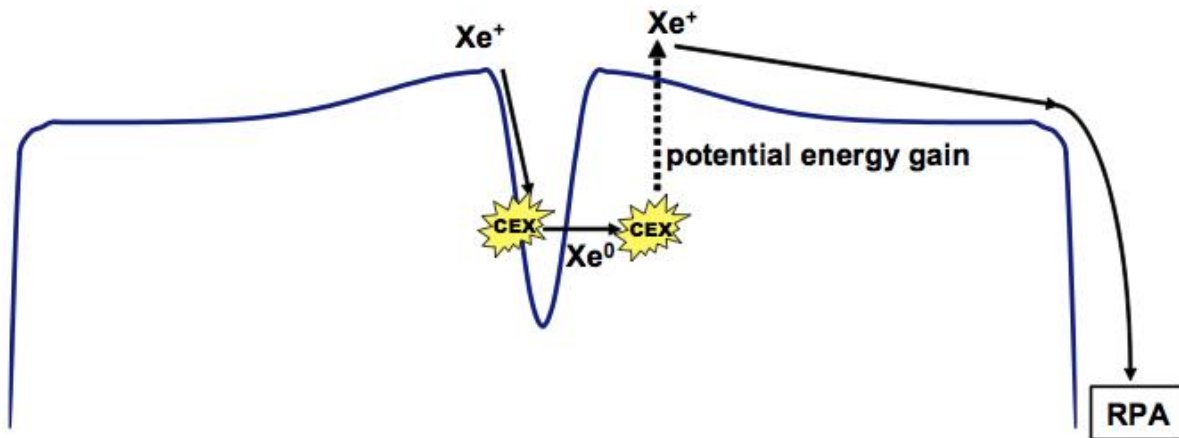


Figure 7: Illustration of xenon charge exchange collisions in the near keeper region of a hollow cathode [4]. Copyright 2008 John Wiley & Sons, Inc.

Although this mechanism could explain the population of radially-directed, high-energy ions measured in experiments, Katz [20] admits that most of these ions will not impact the keeper face, since they are traveling radially. Therefore, potential hills/wells and CEX collisions are still not enough to explain the large, high-energy population of ions responsible for the observed accelerated erosion rates.

Despite extensive research over the past two decades into mechanisms for high-energy ion production in cathode plumes, a definitive cause is still unknown. Another proposed mechanism to explain the observed accelerated erosion rates is ion-acoustic turbulence (IAT) in the hollow cathode plume. Instabilities leading to IAT are commonly found in plasmas and when the relative velocity of ions to

electrons exceeds the local ion speed. In the plume of a hollow cathode, counter-streaming electrons and ions can generate plasma potential oscillations and complex potential structures, such as a double layer, and IAT instabilities. These plasma potential oscillations can manifest themselves as ion-acoustic waves and lead to the production of high energy ions. Large amplitude plasma potential oscillations downstream of the hollow cathode have been measured [21]. In 2013, Mikellides [22] and Jorns [23] published companion papers demonstrating the existence of IAT in the plume of a 100-A LaB₆ hollow cathode. Mikellides [22] provided results from a 2-D Orificed Cathode (OrCa2D) model, which found that the conditions for the enhancement of current-driven instabilities and IAT were satisfied in the plume of the simulated hollow cathode. Jorns [23] published complimentary experimental results demonstrating the existence of IAT in the plume of the hollow cathode. The dispersion and amplitude of axial modes just downstream of the keeper were measured using two probes, at fixed distance apart, biased to a potential corresponding to the ion saturation regime. The onset of IAT was observed at high discharge currents (>50 A) and the character of the oscillations agree with weak turbulence theory, which suggests that the amplitude of the spectrum should decrease with flow rate but increase with discharge current [23]. Additionally, the growth of the IAT was shown to correlate with the appearance of a high-energy tail in the ion energy distribution. It was determined that energetic ion production is enhanced by IAT, where the plasma waves are driven unstable at the expense of energy in the electron drift velocity while the waves in turn transfer energy to the ions through collisional and nonlinear processes [23].

Also investigated was the presence of anomalous collisions in the cathode plume. Mikellides et al. determined, while attempting to model the NSTAR cathode plume that an anomalous collision frequency was required to match their simulation results to experimentally-observed steady state plasma parameters [24, 25]. The measured anomalous collision frequency as measured by Jorns [23] closely matched the required collision frequency required to match simulation results to experimental data, suggesting that anomalous collisions play a significant role in the hollow cathode plume plasma. This anomalous

collision frequency is believed to play a role in the coupling of cathodes to HET discharges and the onset and magnitude of “breathing mode” [26].

Recently, Yanes et al. [27] continued the experimental investigation of high energy ion production via IAT and measured the IAT both axially and radially in the plume of the HERMeS thruster LaB₆ hollow cathode. Since IAT is exacerbated in plume mode and the transition to plume mode can be influenced by cathode geometry such as cathode orifice diameter, the relationship between orifice diameter and plume instabilities was investigated. At high discharge currents (>30 A), a larger orifice reduced the magnitude of the IAT instabilities; however at low flow rates (<10 SCCM) the larger orifice was susceptible to more low frequency instabilities [27]. At smaller orifice diameters it is postulated that the electron streaming (or drift) velocity is higher, since the number densities were confirmed to be equal across all of the orifice diameters tested. Thus, a measurement of the electron drift velocity could support the measurement of IAT in the cathode plume.

Measurement of the EEDF downstream of the hollow cathode could determine the electron drift velocity. Measurements of the EEDF in the plume of a LaB₆ hollow cathode using a single Langmuir probe found that a shifted Maxwellian distribution fit their measured EEDF [28]. The cathode used was nominally a 0.25 inch LaB₆ cathode and the EEDF was measured for a single cathode geometry and operating point. The work of this thesis intends to extend these EEDF measurements to an equivalently sized cathode at various operating points and geometries.

Typically, hollow cathodes have only used noble gases as the working gas since that has been the standard propellant choice for electrostatic thrusters. It has been reported that LaB₆ cathodes have operated on all noble gases, reactive gases including oxygen and hydrogen, and vaporous propellants such as bismuth [29]. A cathode using a relatively new emitter material, C12A7 (or “electride”), has been reported to have operated on iodine propellant for approximately 20 hours [30]. This is the only known emitter to have operated on iodine other than the BaO cathode presented here.

2.3 Iodine as a Propellant for Electrostatic Thrusters

The most common propellants for electrostatic thrusters have been noble gases, specifically xenon, with some exceptions such as mercury and cesium, during their early development [4]. Other propellants have been investigated in the laboratory including krypton, argon and molecular gases (oxygen and nitrogen) [31, 32, 33]. Some condensable propellants have been tried including magnesium, zinc, bismuth and iodine [34, 35, 36]. Xenon is generally preferred to other propellant options since it is inert, not hazardous to handle, does not condense on surfaces (above cryogenic temperatures), easy to ionize (low ionization energy), has a fairly large mass and can be easily stored at high pressure [4]. Along storing xenon at high pressure requires a thick-walled tank, a high-pressure tank is the simplest in design and concept. Other propellant options considered may be preferable to xenon in one of these categories or another, but have other disadvantages, making xenon the practical choice for most applications. Mercury and cesium have a large atomic mass and low ionization potentials but are highly reactive and hazardous to handle. All other noble (krypton, argon) and inert gases (nitrogen) are less expensive (\$/kg) than xenon; however, they have a lower atomic (or molecular) mass, are harder to ionize than xenon and still require high pressure storage tanks. Condensable propellants, i.e. those that condense at “typical” laboratory or spacecraft feed system temperatures, have significant storage advantages, and in some cases, low ionization potentials and large (first) ionization cross sections. Some condensable propellants offer system-level benefits (high T/P or high I_{sp}) but can require significant heating (100’s of degrees Celsius) to generate adequate vapor pressure. Iodine has a unique property (in terms of propellant candidates); it will sublime at relatively low temperatures ($\sim 50^\circ\text{C}$). Iodine was first considered as a propellant in the early 2000’s and is a candidate to replace xenon as the propellant for deep space missions requiring high throughput [37, 38]. Table 2 lists the physical properties of several candidate propellants for electric thrusters.

Table 2: Physical properties of candidate propellants for electric thrusters [39].

Propellant	Atomic Mass (amu)	T _m (°C)	T _b (°C)	First Ionization Potential (eV)	Price (\$/kg)*
Xenon	131.3	-111.79 (tp)	-108.12	12.13	1,138
Krypton	83.8	-157.38 (tp)	-153.22	14.00	295
Cesium	132.9	28.5	671	3.89	40,000
Mercury	200.6	-38.837 (tp)	356.73	10.44	4
Magnesium	24.3	650	1090	7.65	3
Zinc	65.4	419.53	907	9.39	0.5
Bismuth	209.0	271.40	1564	7.29	6
Iodine (I ₂)	126.9	113.75	184.67	10.45 (9.35)	500
Nitrogen (N ₂)	28.0	-210.0 (tp)	-195.8	15.58	3
Oxygen (O ₂)	32.0	-218.8 (tp)	-183.0	12.07	3

*Typical commercial prices in 2017

Xenon and iodine have first-ionization energies, 12.13 eV and 10.45 eV (9.35 eV for I₂), respectively. Both have similar ionization cross sections; however, for electron impact energies below approximately 100 eV the atomic iodine cross section is approximately 50% larger than xenon. Iodine is typically diatomic but has a relatively low dissociation energy (1.57 eV at 298 K) and will almost entirely dissociate at high temperature (>1000 K) [40]. The molecular iodine cross section is twice as large as xenon for electron energies below ~100 eV and is larger than the xenon cross section for electron energies up to 500 eV. Figure 8 shows the ionization cross sections for iodine (I and I₂) and xenon for electron energies up to 500 eV. Iodine has shown similar performance characteristics to xenon in Hall thrusters [41]. Only small levels of I₂⁺ were detected in the HET beam and equivalent amounts of doubly (1.5%) and triply (0.3%) charged iodine and xenon [42].

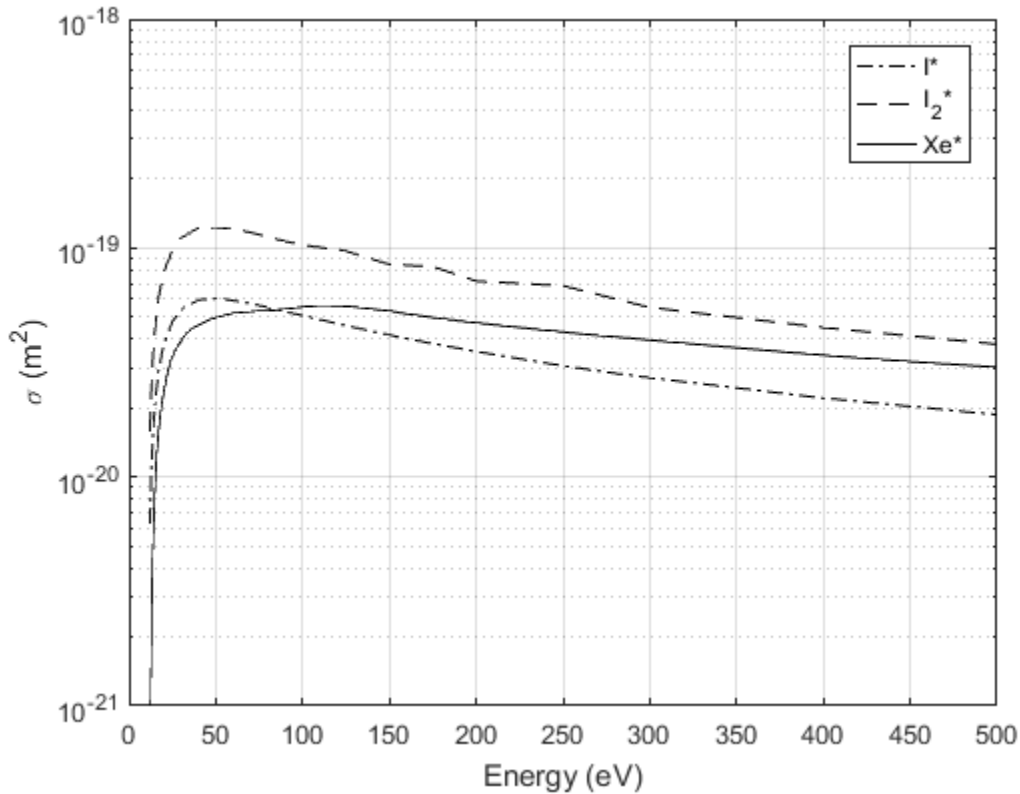


Figure 8: Ionization cross sections for iodine (I and I₂) [43] and xenon [44].

In general for typical EP-powered missions, assuming a fixed spacecraft dry mass, the mass (or change in mass) required for a particular Δv will not change with propellant (for a given I_{sp}), thus the required propellant mass will remain largely the same with xenon and iodine. Also, while the cost savings with iodine is significant for the fuel alone (approximately 50% reduction) the total cost of the propellant for a large mission is on the order of approximately 0.1% of the total mission cost [37]. For example, a typical GEO satellite carries approximately 100 kg of propellant, which would cost approximately \$100k-200k; however, the total spacecraft cost is approximately \$100M [37]. Therefore, while the cost of propellant is a consideration, it may not be a driving factor for a deep-space/Flagship mission. The real mission systems benefit comes from the elimination of the high-pressure (thick-walled) propellant tank required for xenon. Many factors determine the mass of the propellant tank but reasonable estimates for gaseous propellant tanks can be up to 35% of the total propellant mass [45]. Since iodine can be stored at low

pressure (10's of torr) and higher density, the propellant tank can be a much smaller in terms of volume and mass. Iodine also lends itself to conformal tanks, made of non-traditional and light materials such as thermoplastics—further reducing the mass contribution of the propellant tank. The reduction in tank mass lowers the spacecraft dry mass, which in turn allows for additional propellant for a given wet mass; this is quite desirable since it effectively increases mission life for equal cost on the launch pad.

Since iodine can be stored as a solid at ~3 times the density of xenon, the overall tank size can be significantly reduced and conformal tanks can be considered. This would benefit spacecraft of all sizes, but it would benefit small, volume-starved spacecraft in particular, specifically ESPA-class (180 kg) and smaller. (The EELV Secondary Payload Adapter (ESPA) is a payload adapter ring that accepts standardized spacecraft buses and was developed for missions that use Evolved Expendable Launch Vehicles (EELV) such as the Atlas V and Delta IV. These standardized spacecraft are often referred to as *ESPA-class*.) Small spacecraft often are secondary payloads and have fixed or prescribed platforms and buses. A smaller propellant tank would allow for the equivalent (or more) propellant to be stored compared to xenon, but allow more physical space for the payload, instrumentation, for the same spacecraft mass (i.e. launch cost). As mentioned above, iodine is also stored at low pressure, approximately 1000 times lower than xenon. This is a system-level benefit when spacecraft are being considered as secondary payloads as the main payload takes priority and a high-pressure vessel in the secondary payload would be considered a risk.

For high-power and high-throughput missions like the ones currently slated as future NASA Flagship missions (Asteroid Redirect Robotic Mission (ARRM) for example), ground-based full-system testing becomes problematic with xenon. Currently, under the NASA Space Technology Mission Directorate (STMD) Solar Electric Propulsion Technology Demonstration Mission (SEP TEM), a high power ion propulsion system is being co-developed by the NASA Glenn Research Center and the Jet Propulsion Laboratory for the ARRM concept vehicle. The ARRM primary propulsion system consists of four 12.5 kW Hall Effect Rocket with Magnetic Shielding (HERMeS) thrusters clustered together to form a 50 kW-

class electric propulsion system [46]. EP systems up to 100 kW and above have been proposed by NASA for manned missions to Mars and other deep space missions. Current test facilities do not have the pumping speed to maintain adequate background pressure (high 10^{-6} torr [47]) to test these high-power thruster systems, especially in cluster formation, at full scale, throughput and power. Iodine will readily condense on cold surfaces (< 25 C); therefore relevant background pressure can be maintained for high-throughput thrusters using cryogenic and liquid nitrogen (LN2) panels. Iodine will react and form oxides with common vacuum facility materials including aluminum, iron, copper and stainless steel, but these reactions can be mitigated by simple surface coatings such as plating and anodizing. It is important to prevent iodine from reacting with surfaces not only to preserve the vacuum facility but because the iodine compounds formed are more difficult to remove from the chamber post-test since the reaction changes the vapor pressure and the resulting compounds can no longer be simply pumped out. Iodine (and some compounds) are extremely hygroscopic and should be prevented from forming before the vacuum facility is returned to atmospheric pressure with air. Once these compounds have been formed, care must be taken to remove them from the vacuum facility as their presence (in large quantities) may affect pumping speed. Iodine can be potentially hazardous to humans if exposed to large quantities by inhalation or physical contact with the skin [48]. The issues associated with testing iodine from a facilities standpoint are quite manageable if the necessary precautions are taken. Steps to prevent iodine contamination of the vacuum facility will be required for ground-based testing for high-power/high-throughput future missions using iodine propellant.

Iodine has at least one major hurdle to overcome before it can be considered as a replacement for xenon for all missions—its effectiveness and compatibility has not been demonstrated when used as the working gas for plasma-discharge based electron sources, i.e. hollow cathodes. As described in Section 2.2, ion engines and HETs require an electron source, typically in the form of a hollow cathode, which usually operates on the same propellant as the thruster. For high-power/high-throughput missions a “bi-propellant” system may be considered where the cathode operates on xenon and thruster on iodine;

however, even for large systems this is not ideal and for small, volume-starved spacecraft it may nullify most or all of the benefits of using iodine propellant. Iodine propellant has been demonstrated with an electrified (C12A7) cathode for approximately 50 hours [49]. Electride is still in the development stage and far from a replacement for BaO or LaB₆ emitters in hollow cathodes as more testing is required (i.e. duration testing). Iodine is also known to react with typical cathode materials [50]. A flight demonstration of a HET and cathode operating on iodine on a 12U spacecraft was approved in 2015 by NASA's Space Technology Mission Directorate (STMD). This spacecraft, known as iSat and is being co-developed by NASA Glenn Research Center (GRC) [51], Marshall Space Flight Center (MSFC) [52] and Busek Co. Inc. and is scheduled for launch in 2018. Busek Co. Inc. demonstrated more than 100 cathode cycles and 50 hours of operation with a laboratory model BaO hollow cathode, yet the cathode remains a key area of risk for the iSat system [53]. Demonstrating operation with iodine in conjunction with a proven emitter material with flight heritage is critical to iodine being considered a replacement for xenon as an electrostatic thruster propellant.

2.4 Plasma Physics

To fully understand how electric thrusters operate and appreciate the plasma diagnostics used, it is imperative to understand basic plasma physics and charged particle behavior. Hollow cathodes, from insert to plume, involve behavior over a very broad range of plasma regimes. A plasma is defined as a "quasineutral gas of charged and neutral particles which exhibit a collective behavior" [54]. Collective behavior refers to the interaction of many particles, possibly over long length scales, which distinguish plasmas from neutral gases. Quasineutrality means that over a sufficiently long length scale the plasma behaves as if it is electrically neutral even if locally that is not the case.

2.4.1 Electrodynamics and Single Particle Motion

Although James Clerk Maxwell was not the only contributor, he was primarily responsible for determining the self-consistent set of equations that govern electromagnetic field behavior. A key

contribution from Maxwell was the addition of the displacement current ($\frac{\partial \mathbf{E}}{\partial t}$) term in *Ampère's Law*. This term reflected the fact, experimentally observed, that a changing electric field would induce a magnetic field, even without the presence of a flowing current. This addition had profound implications for the physics community and changed the trajectory of electromagnetic theory in nineteenth century. The following set of four differential equations is known as *Maxwell's Equations*.

$$\text{Gauss' Law} \quad \nabla \cdot \mathbf{E} = \frac{\rho}{\epsilon_0} \quad (2-4)$$

$$\text{Faraday's Law} \quad \nabla \times \mathbf{E} = -\frac{\partial \mathbf{B}}{\partial t} \quad (2-5)$$

$$\nabla \cdot \mathbf{B} = 0 \quad (2-6)$$

$$\text{Ampère's Law (for } \frac{\partial \mathbf{E}}{\partial t} = 0) \quad \nabla \times \mathbf{B} = \mu_0 \left(\mathbf{J} + \epsilon_0 \frac{\partial \mathbf{E}}{\partial t} \right) \quad (2-7)$$

Where \mathbf{E} is the electric field, \mathbf{B} is the magnetic field, ρ is the charge density, \mathbf{J} is the current density, ϵ_0 is the permittivity of free space and μ_0 is the permeability of free space. The complexity in plasmas lie in the interactions of the charged particles. Changing electric fields influence magnetic fields, which are then coupled to charged particle motion. The effect of electromagnetic fields on charged particles and the resulting plasma behavior largely depends on the mass and mobility of the particles (ion versus electron). Maxwell's equations, along with Newton's Laws, are used to fully describe the physics and governing equations of plasmas. Other tools, such as statistics and kinetic theory, are required to more fully describe a plasma's collective behavior.

For a particle of charge q , with mass m and velocity \mathbf{v} , the equation of motion in a uniform electromagnetic field is given by Equation 2-8. This equation is known as the *Lorentz Force Equation*.

$$\mathbf{F} = m \frac{d\mathbf{v}}{dt} = q(\mathbf{E} + \mathbf{v} \times \mathbf{B}) \quad (2-8)$$

For a charged particle interacting with a uniform magnetic field in the \hat{z} direction, in the absence of an electric field ($\mathbf{E} = 0$), the equation of motion can easily be simplified and broken up in terms of spatial coordinate. Taking the time-derivative and solving for each velocity component results in two (since $\frac{\partial v_z}{\partial t} = 0$) second order, coupled differential equations. These equations of motion take the form of a simple harmonic oscillator at the characteristic plasma frequency ω_c , known as the cyclotron frequency for electrons [55].

$$\omega_c = \frac{|q|B}{m} \quad (2-9)$$

Considering only the direction perpendicular to the applied magnetic field, the solution to equations of motion show that the particle will travel in a circular orbit around a *guiding center* with a period of ω_c [55]. Figure 9 shows the free body diagram and circular orbit in the x-y plane of a positively charged particle.

The radius of this circular orbit is known as the Larmor radius and depends on the particle mass, the magnitude of the magnetic field and the particle velocity perpendicular to the applied magnetic field. The Larmor radius can be defined several ways and all are presented below.

$$r_L = \frac{mv_{\perp}}{qB} = \frac{v_{\perp}}{\omega_c} = \frac{1}{B} \sqrt{\frac{2mv_{\perp}}{e}} \quad (2-10)$$

Considering the direction parallel to the applied magnetic field, the particle will travel parallel to the magnetic field at velocity v_{\parallel} . The velocity along \mathbf{B} is constant and equal to the particle's initial velocity (assumed collisionless) for a constant magnitude magnetic field. The resulting particle trajectory is given by the superposition of a uniform motion along the applied B-field and a circular motion perpendicular to the applied B-field [55]. This is the characteristic helical trajectory of a charged particle along a magnetic field line and is shown in Figure 9. The angle between the applied magnetic field and the direction of the motion of the particle is known as the *pitch angle* and is given by the following equation [55].

$$\alpha = \sin^{-1}\left(\frac{v_{\perp}}{v}\right) = \tan^{-1}\left(\frac{v_{\perp}}{v_{\parallel}}\right) \quad (2-11)$$

Where v is the total speed of the charged particle.

As determined by Maxwell, a changing electric field, caused in this case by a charged particle in motion, will induce a magnetic field. Due to the direction of gyration, this induced magnetic field will always oppose the direction of the applied magnetic field. Thus, the motion of charged particles tend reduce the applied magnetic field [54].

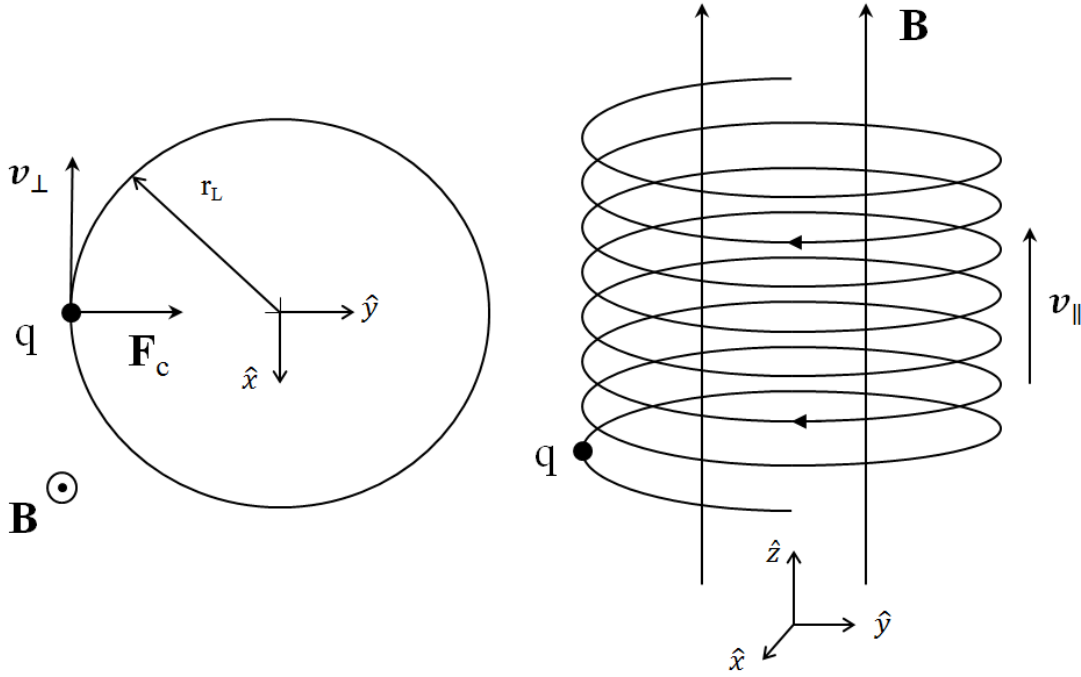


Figure 9: Charged particle trajectory in the presence of a uniform magnetic field top view (left) and side view (right) (adapted from [4] and [55]).

If a finite electric field is imposed perpendicular to the applied magnetic field the equation of motion can be solved in a similar fashion as the previous case without an electric field. The result is a drift of the guiding center in the direction perpendicular to both \mathbf{E} and \mathbf{B} . The guiding center drifts at a particular velocity and is known as the *drift velocity* which is described by the following equation [54].

$$\mathbf{v} = \frac{\mathbf{E} \times \mathbf{B}}{B^2} \equiv \mathbf{v}_E \quad (2-12)$$

The result of the drift velocity is an elongation and flattening of the helical trajectory the charge particle follows. Although oppose in sign, both ions and electrons will drift in the same direction as \mathbf{v}_E is independent of m , q and v_\perp [54]. In a collisionless plasma this drift velocity will not result in a current since the ions and electrons move together; however, in a collisional plasma, ions move slower than electrons due to their lower mobility. The resulting difference in collision frequency causes ions and electrons to drift at different velocities and gives rise to an electric current, dominated by electrons. This induced current is known as the *Hall current*.

2.4.2 Sheaths

Although plasmas are electrically neutral on the whole, when a boundary such as a wall or probe is in contact with a plasma it will adjust to the perturbation and the local neutrality will be disturbed. Since electrons have a much smaller mass and (usually) higher temperature, and hence a higher collision frequency, than ions they have a much higher mobility. Therefore, electron flux to the boundary will be much higher than ions.

For an electrically isolated, conducting object, immersed in an plasma a sheath will develop around it. Initially, it will collect electrons leaving a positive space charge behind, which will tend to slow electron transport to the object. Initially, the current density of electrons and ions will be dictated by their random flux [9].

$$J_e = -e\Gamma_e = -\frac{1}{4}en_e\bar{v}_e = -en_e\sqrt{\frac{k_bT_e}{2\pi m}} \quad (2-13)$$

$$J_i = e\Gamma_i = \frac{1}{4}en_i\bar{v}_i = en_i\sqrt{\frac{k_bT_i}{2\pi M}} \quad (2-14)$$

where \bar{v} is the average particle velocity, n is the density, k_b is Boltzmann's constant, T is the particle temperature, m is the electron mass and M is the ion mass. These current densities would suggest that the number densities are equal, resulting in a much higher flux of electrons than ions since, in general, $\sqrt{T_e/m}$ greatly exceeds $\sqrt{T_i/M}$ [55]. The rapid accumulation of electrons will create a negative charge, thereby attracting ions and repelling electrons, reducing the electron flux. This oscillation of electron and ion flux will quickly reach steady-state, where the object's potential is sufficiently negative to equilibrate the flux of electrons with ions. This potential is known as the *floating potential* and is typically lower than the plasma potential due to the difference in temperature and mobility between ions and electrons.

Due to the electron's higher mobility, the flux of negative charge to the boundary is larger than positive charge. This creates a region of negative space charge near the boundary, which inhibits the flow of electrons to the wall. This self-consistent current balance, with the associated potential and density gradients, is known as the plasma *sheath* [4]. A sheath represents a non-quasineutral region through which the potential transitions from the value in the plasma to that of the surface. Sheaths can be positive or negative depending on the plasma conditions and the bias on the surface. The thickness is defined as the distance from the wall (or boundary) to the potential at the unperturbed plasma. For the case of a floating or grounded wall, this thickness is dictated by the potential at the sheath edge (sheath potential, $e\phi$) and the electron temperature of the unperturbed plasma, $k_b T_e$. Poisson's equation can be solved to determine the radial potential distribution in a plasma. (Poisson's equation is the form of Gauss's law when the magnetic field is static (or nonexistent), in which case the electric field can be described by the gradient of a scalar potential, $\mathbf{E} = -\nabla\phi$.)

$$\nabla^2\phi = -\frac{\rho}{\epsilon_0} = -\frac{e}{\epsilon_0}(Zn_i - n_e) \quad (2-15)$$

One can classify sheath solutions into three main classes, depending on the magnitude of the electron temperature relative to the potential drop in the sheath. For the first case, the potential drop through the

sheath will be much less than the electron temperature in the bulk plasma ($e\phi \ll k_b T_e$). For a fixed ion density, electrons follow the Boltzmann relationship

$$n_e(x) = n_0 \exp\left(\frac{e\phi(x)}{k_b T_e}\right) \quad (2-16)$$

and the above equation can be linearized and solved for the potential as a function of radial distance [4].

$$\phi = \frac{e}{4\pi\epsilon_0 r} \exp\left(-r / \sqrt{\frac{\epsilon_0 k_b T_e}{n_0 e^2}}\right) \quad (2-17)$$

This equation shows the potential falls off exponentially with increasing distance from the boundary. The denominator of the exponential term is defined as the characteristic length over which potential changes are small compared to the bulk and is known as the *Debye length*.

$$\lambda_D = \sqrt{\frac{\epsilon_0 k_b T_e}{n_0 e^2}} \quad (2-18)$$

For the second case, where the sheath potential drop is of the same order as the bulk electron temperature ($e\phi \approx k_b T_e$) the transition from the bulk plasma to the sheath is gradual and the concept of the *presheath* is necessary. It is assumed that ions enter the sheath with zero temperature so the ion velocity is v_0 derived using an arbitrary potential, ϕ_0 . The arbitrary potential ϕ_0 represents the potential difference between the bulk plasma and the sheath edge and is known as the *pre-sheath potential drop*.

$$\frac{1}{2} M v_0^2 = e\phi_0 \quad (2-19)$$

Once past the sheath edge, ions will gain additional energy as they fall towards the boundary. Considering a 1-D case, the ion velocity through the sheath can be defined using conservation of energy and substituting the ion velocity as the sheath edge.

$$v = \sqrt{\frac{2e}{M} [\phi_0 - \phi(x)]^{1/2}} \quad (2-20)$$

Using $v_0 = \sqrt{2e\phi_0/M}$, Equation (2-20) can be rewritten as

$$\frac{v_0}{v} = \sqrt{\frac{\phi_0}{\phi_0 - \phi}} \quad (2-21)$$

which represents the ion acceleration towards the boundary. Since the ion flux through the sheath must be conserved ($n_i v = n_0 v_0$), the ion density anywhere in the sheath can be described by

$$n_i = n_0 \sqrt{\frac{\phi_0}{\phi_0 - \phi}} \quad (2-22)$$

The electron density through the sheath can be determined using the Boltzmann relation, which describes the density of charged particles in equilibrium under the influence of an electrostatic field [55].

$$n_e = n_0 \exp\left(-\frac{e\phi}{k_b T_e}\right) \quad (2-23)$$

Using equations (2-22) and (2-23) in Poisson's equation, one can show that in order to maintain a monotonically decreasing potential as ions move towards the wall and to prevent ions from being reflected away from the wall, the following inequality must be true.

$$\phi_0 > \frac{k_b T_e}{2e} \quad (2-24)$$

This inequality is known as the Bohm sheath criterion and shows that an ion must fall through a potential drop of at least $T_e/2$ before it will enter the sheath, which defines the pre-sheath. This can be rewritten using $v_0 = \sqrt{2e\phi_0/M}$, which is known as the *Bohm speed*.

$$v_0 \geq \sqrt{\frac{k_b T_e}{M}} \quad (2-25)$$

This represents the minimum velocity an ion must have to enter the sheath in order to maintain the original sheath criterion of a monotonically decreasing potential towards the boundary. Due to the ion acceleration towards the wall, the plasma density in pre-sheath must decrease. Using the Boltzmann distribution and the Bohm sheath criterion the current density of ions entering the sheath can be determined.

$$J_i = 0.6n_0 e v_i \approx \frac{1}{2} n e \sqrt{\frac{k_b T_e}{M}} \quad (2-26)$$

Where n is the plasma density at the beginning of the pre-sheath. Multiplying the current density by the ion collection area at the sheath boundary the Bohm current can be defined.

$$I_i = \frac{1}{2} n e \sqrt{\frac{k_b T_e}{M}} A \quad (2-27)$$

The third case corresponds to the sheath solution where the potential drop across the sheath is much larger than the electron temperature ($e\phi \gg k_b T_e$) and is called the Child-Langmuir sheath solution. For this case the potential drop is so large that only a negligible quantity of electrons have sufficient energy to overcome the potential barrier and reach the surface. As a result, the electron density in the sheath can be neglected. Using Equation (2-20) to determine the ion velocity through the sheath, the ion current density can be obtained.

$$J_i = n_i e \sqrt{\frac{2e}{M} [\phi_0 - \phi]^{1/2}} \quad (2-28)$$

Solving Poisson's equation in one dimension using the above equation for ion current density and neglecting the electron density yields the following relationship known as the Child-Langmuir law. This

relationship reflects the space-charge limited current that can be extracted through a high-voltage sheath. It plays an essential role in ion thruster performance, specifically, establishing limits on current extraction and hence thrust density.

$$J_i = \frac{4\epsilon_0}{9} \left(\frac{2e}{M} \right)^{1/2} \frac{V^{3/2}}{d^2} \quad (2-29)$$

Where d is the sheath thickness and V is the potential difference across the sheath. The overall potential drop is much larger than the pre-sheath potential drop, ϕ_0 mentioned in the previous sheath solution. (The pre-sheath potential drop is neglected in some derivations of the Child-Langmuir sheath solution [56].)

Other sheaths, where one of the boundaries is not a wall or physical surface, exist in plasmas. A situation may exist where large gradients in potential exist between two regions in a plasma—a common occurrence in electric thruster and cathode plasmas [4]. As with other physical boundary conditions, a self-consistent charge distribution is established with an associated potential and density gradients. These are known as double sheaths or *double layers*. Across the double layer electrons and ions still travel in opposite directions as in previous sheath cases but the potential on either side is not zero. This potential difference accelerates both ions and electrons across the double layer. The conservation of energy for the electrons can be solved for their velocity.

$$v_e = \sqrt{\frac{2e\phi}{m}} \quad (2-30)$$

The conservation of energy for the ions gives the same ion velocity as derived for previous sheath conditions (Equation (2-20)). Summing the charge densities and applying a one-dimensional Poisson's equation it can be shown [4] that the electron current density across the double layer is proportional to the ion current density by the square root of the mass ratio and a constant κ .

$$J_e = \kappa \sqrt{\frac{M}{m}} J_i \quad (2-31)$$

This relationship is known as the Langmuir condition and describes the space-charge-limited flow of electrons and ions across a double layer. The constant, κ , arises from double layers where initial velocities at the sheath edges are non-zero and varies from 0.8 to 0.2 for T_e/T_i ranging from 2 to 20 [4]. The double layer can also form if the electron drift speed exceeds the electron thermal speed. The ratio of the electron drift velocity and thermal velocity is known as the electron *Mach number*.

2.4.3 Plasma Characteristics

The Knudsen number is a non-dimensional number used to describe fluid regimes and is applicable to plasmas. The Knudsen number is the ratio of the mean free path of particles in the system and a characteristic length scale. According to Knudsen number, three broad flow regimes exist for fluids; continuum flow ($\text{Kn} < 0.01$), transitional flows ($0.01 < \text{Kn} < 1$), free molecular flow ($\text{Kn} > 1$) [57]. For invasive plasma diagnostics, such as Langmuir probes, the characteristic length is the probe diameter.

Knowledge of the mean free path is not only important in determining the Knudsen number and invasiveness of interrogation methods, but also for calculating other parameters such as collision frequency. Particles in plasmas interact entirely through collisional processes. Collisions involve all species (ions, electrons, neutrals) in the plasma and surroundings, and determine many properties of the plasma including diffusion, resistivity and mobility. For a collision between two particles, the center of the incoming particle must enter the *cross section*, which is an imaginary circle of area σ whose center is coincident with the center of the target particle. If the two colliding particles are neutrals the cross section is simply the sum of the two radii, $\pi(r_1 + r_2)$. The mean free path for collisions involving neutrals is given by

$$\lambda = \frac{1}{n_n \sigma} \quad (2-32)$$

where n_n is the neutral density and σ is the cross sectional area of the neutrals. This also represents the mean distance a charged particle, such as an ion or electron, will travel in a slow/stationary population of neutrals.

The cross section can be much larger than the geometric area of the colliding particles when they carry charge due to coulomb forces and Debye shielding. The probability of these collisions in a plasma can be expressed in terms of an *effective cross section*. It is difficult to capture this complexity and typically empirically derived cross sections are necessary to calculate plasma parameters involving cross sections. Bittencourt provides an analytical solution to the momentum transfer cross section for electron-ion collisions [55].

$$\sigma_m = 2\pi b_0^2 \ln \left(1 + \frac{\lambda_D^2}{b_0^2} \right) \quad (2-33)$$

Where b_0 is the *impact parameter* and is defined as

$$b_0 = \frac{e^2}{12\pi\epsilon_0 k_b T} \quad (2-34)$$

2.4.4 Distribution Functions

Due to the large number of particles in plasmas a statistical approach is necessary to describe macroscopic quantities. Particle collisions lead to distributions of particle velocities. Probability distributions provide a basis for statistical description of kinetic behaviors. For any classical system in equilibrium, regardless of the interaction between particles, a Gaussian distribution derived by Maxwell and Ludwig Boltzmann known as the *Maxwell velocity distribution* (or *Maxwellian*) describes the distribution of particles [58]. In terms of velocity, the Maxwellian distribution is

$$f(v) = \left(\frac{m}{2\pi k_b T}\right)^{3/2} \exp\left[-\frac{m}{2k_b T}(v_x^2 + v_y^2 + v_z^2)\right] \quad (2-35)$$

where m is the particle mass, k_b is Boltzmann's constant, T is the temperature, and v_x , v_y and v_z are the three velocity components [59].

The Maxwellian velocity distribution may also be written in terms of the particle's speed by converting to spherical coordinates and integrating over a differential "volume" element, or solid angle $d\Omega = \sin(\phi)d\phi d\theta$. The Maxwellian speed distribution is then given by the following expression where C is the particle's speed [59].

$$f(C) = 4\pi \left(\frac{m}{2\pi k_b T}\right)^{3/2} C^2 \exp\left(-\frac{mC^2}{2k_b T}\right) \quad (2-36)$$

Certain statistical quantities can be determined for the particle's speed including the average speed \bar{C} , the root-mean-square speed $(\overline{C^2})^{1/2}$ and the most probable speed C_{mp} . These quantities are expressed in the following relations:

$$\bar{C} = \frac{2}{\sqrt{\pi}} \left(\frac{2k_b T}{m}\right)^{1/2} \cong 1.13 C_{mp} \quad (2-37)$$

$$C_{mp} = \left(\frac{2k_b T}{m}\right)^{1/2} \quad (2-38)$$

$$(\overline{C^2})^{1/2} = \left(\frac{3k_b T}{m}\right)^{1/2} \cong 1.22 C_{mp} \quad (2-39)$$

The Maxwellian speed distribution can also be rewritten in terms of kinetic energy, ε —a form that is particularly useful in plasma physics as particles and systems are often referred to by their energy and temperature. By making the substitution $\varepsilon = \frac{1}{2}mC^2$ and $f(\varepsilon) = f(C) \frac{dC}{d\varepsilon}$, where $\frac{dC}{d\varepsilon} = \left(\frac{1}{2m\varepsilon}\right)^{1/2}$ into the speed distribution, one can obtain the Maxwellian energy distribution.

$$f(\varepsilon) = \frac{2}{(k_b T)^{3/2}} \sqrt{\frac{\varepsilon}{\pi}} \exp\left(-\frac{\varepsilon}{k_b T}\right) \quad (2-40)$$

Where ε is the particle's kinetic energy and T is the temperature. The width of the distribution is dictated by the temperature (shown by the root-mean-square, Equation (2-39)), where larger temperatures reflect a wider range of probable particle energies. The average, root-mean-square and most probable energy can be calculated from the energy distribution or by substituting the kinetic energy into the above relations corresponding to speed.

Since the velocity distribution is a product of three, independent factors, the probability of the velocity of a particle in a particular direction is independent of the velocity in any other direction. For collective velocity in the z-direction the velocity component becomes $v_z = v_z + v_d$, where v_d represents the *drift velocity*. Substituting v_z into Equation (2-35), converting to spherical coordinates and integrating over all angles gives the following speed distribution.

$$f(C) = \frac{2}{v_d} \left(\frac{m}{2\pi k_b T} \right)^{1/2} \exp \left[-\frac{mv_d^2}{2k_b T} \right] C \exp \left(-\frac{mC^2}{2k_b T} \right) \sinh \left(\frac{mCv_d}{k_b T} \right) \quad (2-41)$$

This speed distribution can also be rewritten in terms of the kinetic energy, $\varepsilon = \frac{1}{2}mC^2$ and the drift velocity written in terms of energy, $\varepsilon_d = \frac{1}{2}mv_d^2$. The Maxwellian energy distribution resulting from a drift velocity in one direction is expressed as follows [60]:

$$f(\varepsilon) = \left(\frac{1}{\pi k_b T \varepsilon_d} \right)^{1/2} \exp \left[-\frac{\varepsilon + \varepsilon_d}{k_b T} \right] \sinh \left(2 \frac{\sqrt{\varepsilon \varepsilon_d}}{k_b T} \right) \quad (2-42)$$

Where T still represents the temperature, or width of the distribution.

In systems composed of two or more species, such as plasma with neutrals, ions and electrons, distribution functions can be used to describe the distribution of individual species in the system. In plasmas, since electrons have high mobility they are easily influenced by electric and magnetic fields; thus, dictate much of the plasma processes—making the electron energy distribution function important to characterizing a particular discharge. Elementary processes can be described by six main parameters:

cross section, probability, mean free path, interaction/collision frequency, reaction rate and reaction rate coefficient.

In the event that a relatively slow neutral is incident on a population of fast moving electrons the mean free path is defined as

$$\lambda = \frac{v_n}{n_e \langle \sigma v_e \rangle} \quad (2-43)$$

where v_n is the neutral particle velocity and the term in brackets is the reaction rate coefficient [59]. This represents the mean distance an incident neutral particle will travel in a population of electrons before ionization occurs [4]. The reaction rate coefficient describes the cross section averaged over all relevant collision cross sections and electron velocities.

$$k_{A+B} = \int \sigma(v) v f(v) dv = \langle \sigma v \rangle \quad (2-44)$$

Where ν is the collision frequency. The *collision frequency* of any (charged or neutral) two particles A and B can be defined by the ratio of their velocity relative to the mean free path.

$$\nu_A = n_B \sigma v \quad (2-45)$$

The mean time between collisions can then be calculated from the mean free path divided by the particle velocity, or the inverse of the collision frequency.

$$\tau = \frac{1}{\nu_A} \quad (2-46)$$

To account for the distribution of particles the collision frequency relation should be integrated (averaged) and multiplied by the velocity distribution function

$$\nu_A = n_B \int \sigma(v) v f(v) dv = n_B \langle \sigma v \rangle \quad (2-47)$$

The reaction rate represents the number of collisions per unit volume, per unit time, in a plasma and is specific to each reaction.

$$w_{A+B} = v_A n_A = \langle \sigma v \rangle n_A n_B \quad (2-48)$$

For example, the production rate of ions is expressed by:

$$\frac{dn_i}{dt} = n_a n_e \langle \sigma_i v_e \rangle \quad (2-49)$$

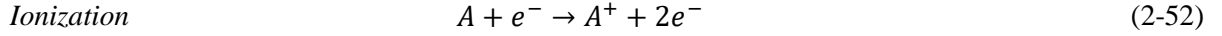
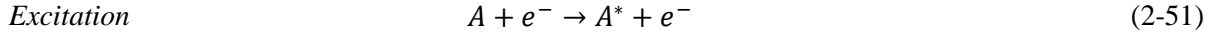
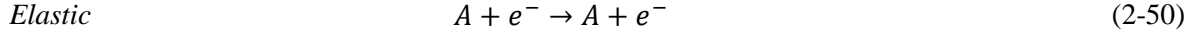
where σ_i is the ionization cross section for the atom or molecule and v_e is the electron velocity. Again, the bracketed term is the reaction rate coefficient, which is the ionization cross section, averaged over the electron energy distribution function. Assuming a quasi-neutral plasma, if the cross sections are known for all the reactions in a given plasma all the reaction rates can be calculated simply with the knowledge of the plasma density and electron velocity distribution function. Thus, cross sections and EEDF's are powerful tools used to characterize a plasma and determine the importance of specific reactions.

2.4.5 Collision Processes

As mentioned in the previous section, due to the electron's high mobility, they drive many plasma characteristics including the distribution function, making knowledge of collisional processes involving electrons important to understanding plasmas. In general, collisional processes in plasmas can be subdivided into two categories—elastic and inelastic. In elastic collisions the internal energy of the colliding particles does not change and total kinetic energy is conserved. These collisions basically lead to scattering of particles and a redistribution of kinetic energy in the system. Inelastic collisions include excitation and ionization, where for electron-atom or electron-molecule collisions, the internal energy of the target particle changes. If an electron collides with an excited atom or molecule, the internal energy of the target particle may be transferred to the electron increasing its kinetic energy—these collisions are termed *superelastic*.

In monatomic gases such as xenon collisional processes involving electrons are limited to elastic, excitation and ionization. The products include neutrals, excited atoms, ions and electrons. These collisional processes are listed in Table 3.

Table 3: Collisional processes involving electrons in monatomic plasmas



For elastic collisions the state of the target particle does not change and coulomb forces do not play a role; however, energy is exchanged. For collisions resulting in excitation, outer valence electrons are promoted to excited orbitals and remain there until the atom relaxes. Obviously, the excitation energy required to promote the electron is quantized; therefore, these collisions have discrete energy magnitudes. The finite value of the energy transfer is dictated by the size and shell configuration of the target atom. If an incident electron has high enough energy to remove a bound valence electron, ionization of the target atom will occur. The threshold energy to remove a bound electron from a given atom or molecule is known as the *ionization potential*. For all of these processes an electron simply loses energy, but is not lost entirely from the plasma. Inelastic collisions can play a major role in the free electron energy distribution in a plasma since excitation and ionization often require significant fractions of the incident electron's energy; therefore, these processes shift the mean energy of the free electron population to lower values [3]. If the incident electron has exceedingly high energy more than one bound valence electron can be removed during a single collision—resulting in a multiply charged ion. All of these processes have associated cross sections which can be used, in conjunction with the electron density and energy distribution function (reaction rate coefficient) to determine the rate of each process. Table 4 shows the reaction rates for excitation and ionization processes in a typical, quasi-neutral xenon plasma, assuming a Maxwellian electron energy distribution with a temperature a 5 eV.

Table 4: Reaction rates for a typical xenon plasma.

n_e (m ⁻³)	T_e (eV)	$\langle\sigma^*v\rangle$ (m ³ /sec) [†]	$\langle\sigma_i v\rangle$ (m ³ /sec) [†]	$\frac{dn^*}{dt}$ (m ⁻³ sec ⁻¹)	$\frac{dn_i}{dt}$ (m ⁻³ sec ⁻¹)
10 ¹⁶	5	1.30·10 ⁻¹⁴	7.61·10 ⁻¹⁵	1.30·10 ⁻¹⁸	7.61·10 ⁻¹⁷

[†] Reaction rate coefficients from Goebel [4] Appendix E.

When plasmas with molecular gases are considered, the number of processes involving electrons grows considerably. Only processes involving electron impacts with mononuclear, diatomic molecules are considered here since iodine is both mononuclear and diatomic, and the complexity of the collisional processes increase considerably when non-mononuclear and polyatomic molecules are considered. Special consideration will be given to iodine-specific processes and cross sections. Common collisional processes involving electrons in plasmas consisting of diatomic molecules are listed in Table 5.

Table 5: Collisional processes involving electrons in diatomic plasmas

<i>Elastic</i>	$AB + e^- \rightarrow AB + e^-$	(2-53)
<i>Rotational Transition</i>	$AB(J) + e^- \rightarrow AB(J') + e^-$	(2-54)
<i>Vibrational Transition</i>	$AB(v) + e^- \rightarrow AB(v') + e^-$	(2-55)
<i>Electronic Excitation</i>	$AB + e^- \rightarrow AB^* + e^-$	(2-56)
<i>Ionization</i>	$AB + e^- \rightarrow AB^{+(*)} + 2e^-$	(2-57)
<i>Dissociation</i>	$AB + e^- \rightarrow A^{(*)} + B + e^-$	(2-58)
<i>Dissociative ionization</i>	$AB + e^- \rightarrow A^{+(*)} + B + 2e^-$	(2-59)
<i>Electron capture</i>	$AB + e^- \rightarrow AB^-$	(2-60)
<i>Dissociative electron attachment</i>	$AB + e^- \rightarrow (AB)^* \rightarrow A^- + B$	(2-61)
<i>Ion pair formation</i>	$AB + e^- \rightarrow A^- + B^+ + e^-$	(2-62)
<i>Dissociative recombination</i>	$AB^+ + e^- \rightarrow (AB)^* \rightarrow A + B^*$	(2-63)

For molecular plasmas the two general types of collisions, elastic and inelastic, still apply. In molecular plasmas there are three types of elastic collisions; elastic, rotational and vibrational. In all three elastic collisions the molecule remains in the ground state after the collision. For rotational and vibrational elastic collisions energy is exchanged and held internally in the molecule. Rotational collisions are fairly low-energy, on the order of a few meV or less, and therefore, are not a significant source of electron

energy loss from the system [61]. Vibrational excitation, even in the ground state, is the highest energy electron-molecule elastic collision and can be a source of electron energy loss from the system.

Molecular electronic excitation and ionization, in principle, happens in a similar manner to excitation and ionization in atoms. The incident electron must have sufficient energy to promote a bound electron to a higher orbital energy (excitation) or remove a bound electron (ionization). In either collision, the molecule is often left in some state of vibrational excitation, with typical periods of 10^{-14} - 10^{-13} seconds [62]. The oscillation time is much longer than the electron-molecule interaction time, which is on the order of 10^{-16} - 10^{-15} seconds [62]. This means that any electronic process (excitation or ionization) happens much faster than the response time of the nuclei; therefore, the nuclei can be considered stationary during electron-molecule collisions. This is known as the *Frank-Condon Principle*. Figure 10 shows two potential energy curves (before and after a collision) with the vibrational states of each electronic state indicated by ν'' for the ground state and ν' for the excited state. For each state the harmonic-oscillator probability density is plotted. Electronic transitions are indicated by vertical lines as dictated by the Frank-Condon Principle.

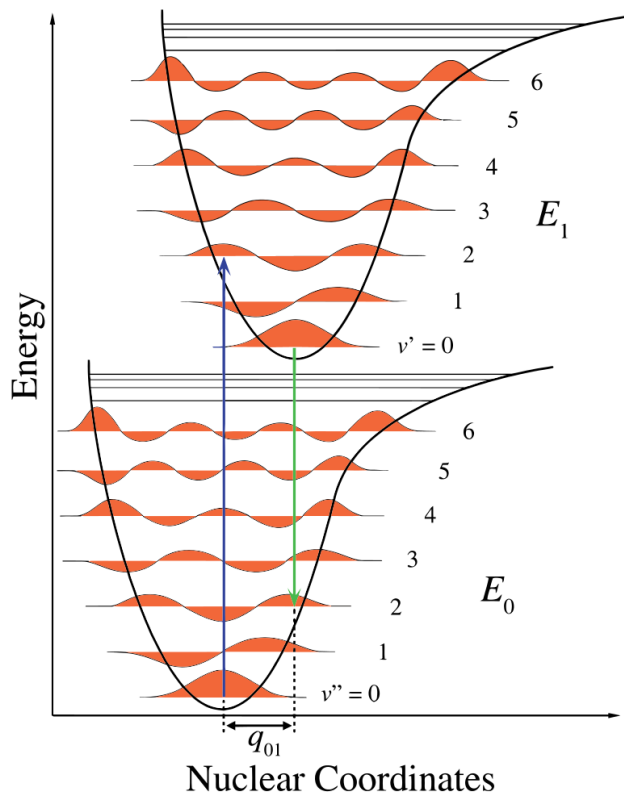


Figure 10: Two electronic potential energy curves showing the vibrational states associated with each electronic state [63].

For non-dissociative excitation (2-56) or ionization (2-57) to occur the electron energy cannot greatly exceed the threshold energy for excitation or ionization since excess energy can be stored in vibrational modes of the excited or ionized molecule. Otherwise, when the electron energy greatly exceeds the threshold energy for either process, the excess energy cannot be stored internally and the molecule dissociates leading to processes (2-58) and (2-59).

Unique to molecular plasmas, electron loss mechanisms exist via electron capture (2-60) and dissociative electron attachment (2-61) processes. For molecules with positive electron affinities, low energy electrons can be captured by the molecule and a negative molecule formed. Dissociative electron attachment is a two-step process where the products have positive electron affinities. First an excited molecule is formed, which is unstable and then dissociates into a neutral and negative ion. The process is described by the potential energy diagram below in Figure 11. First the molecule transitions from the

ground state (AB) to excited state (AB^*) following a vertical transition as dictated by the Frank-Condon principle. Once the excited state is reached, it is possible for the electron to detach from the molecule, but once it reaches the intersection point (R_x) the AB potential energy exceeds that of AB^* and it dissociates into a neutral and negative ion.

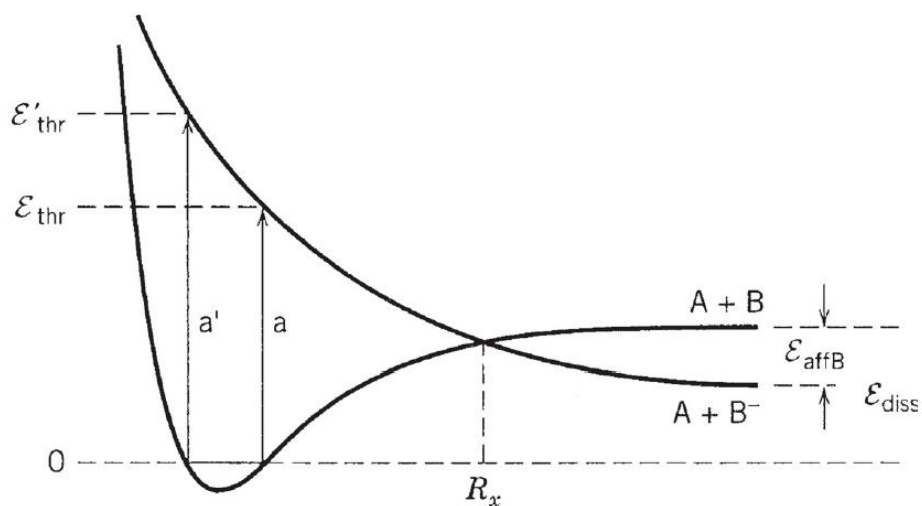


Figure 11: Potential energy diagram for dissociative electron attachment for products with low electron affinity [56].

Where ϵ_{affB} is the electron affinity of the resulting atom and ϵ_{diss} is the dissociation energy (measured from 0 to the upper dashed line at AB).

Depending on the electron affinity and dissociation energy the likelihood of electron attachment can increase. If the electron energy exceeds the dissociation energy, electron attachment becomes much more likely. The potential energy diagram for this process is shown in Figure 12, where the dashed line represents a potential energy of zero.

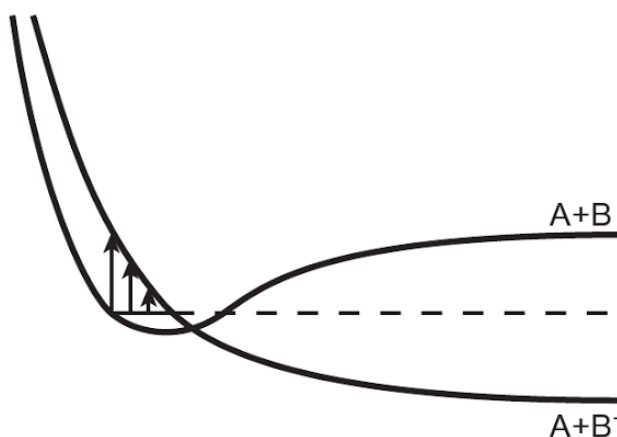


Figure 12: Potential energy diagram for dissociative electron attachment for products with high electron affinity [62]. Copyright Alexander Fridman 2008.

In this case, the intersection point (where the two solid lines intersect) of AB and AB⁻ is actually inside the so-called geometric size of the dissociating molecule. Thus, the likelihood of the excited state detaching an electron is extremely low, leading to an increase in the probability of dissociation and electron attachment [62].

For some molecular gases, such as iodine (halogen), where the electron affinity (2.5 eV) [64] exceeds the dissociation energy (1.5 eV) [40] very low-energy electrons can provide dissociation. Like any electron-ion collision, dissociative attachment has an associated cross section. The dissociative attachment cross section for several molecules is shown below in Figure 13. This clearly shows the dissociative attachment cross section is quite high for iodine and favors much lower electron energy compared to other molecules.

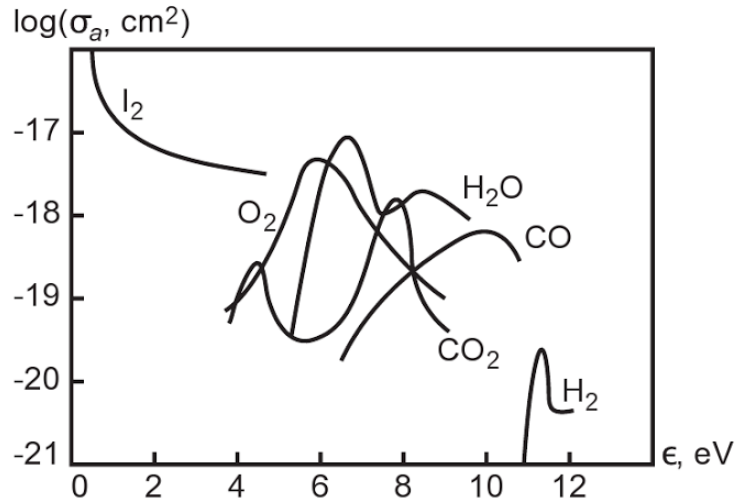


Figure 13: Dissociative electron attachment cross sections for several molecules as a function of energy [62]. Copyright Alexander Fridman 2008.

Dissociative attachment can be enhanced by a process known as *resonant capture* if the molecule has a negative ion state very close to the ground state, resulting in negative ions with a long lifetime [62]. In this process dissociation occurs directly from electron impact rather than dissociation by establishing an excited molecule which subsequently breaks apart due to internal energy. Negative ions are formed by exploiting the resonant capture process capture electrons at low energy after an inelastic collision with a molecule [65]. This process results in a complete loss of the incident electron from the system and results in a negative ion and neutral atom.

Negative ions may also be formed in conjunction with positive ions—this process is known as *ion pair formation*, or *polar dissociation*. The incident electron must have sufficient energy to dissociate the target molecule and ionize the resulting atom; therefore, these are relatively high energy collisions (at least above the resulting atom's ionization potential). This process is enhanced by the same resonant capture process described above, which enhances dissociative attachment by direct dissociation and electron capture [62].

Another possible electron loss mechanism in molecular plasma includes dissociative electron-ion recombination. A process by which an electron combines with a molecular ion to form an excited molecule, then dissociates into any combination of neutrals and excited atoms [62].

2.4.6 Iodine Literature Review

Based on the atomic and molecular processes explained in the previous section, what follows is a summary of relevant, iodine-specific cross sections for processes in an iodine plasma. Since iodine is the focus of this work and one of the first molecular propellants to be considered for electric propulsion, cross sections and other data for common processes found in electrostatic thruster discharges is not well established [66].

Since iodine will dissociate at elevated temperatures (Moutinho suggests that a large percentage of iodine vapor will be dissociated at temperatures above 1000 K [64]), electron collisions with atomic iodine must also be considered in an iodine discharge. Figure 14 plots the single and double ionization cross section for atomic iodine by electron impact. Uncertainties in the measurements are $\pm 12\%$ for some of the data points shown [43]. The solid and dashed lines are from Ali [43]. The open squares are from Hayes and experimental single ionization cross section

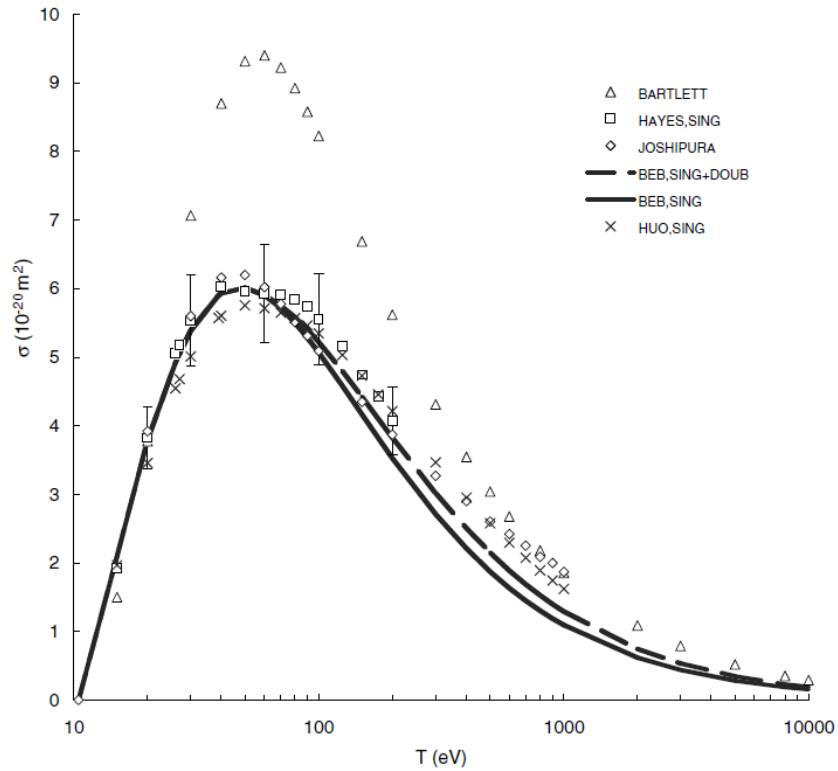


Figure 14: Ionization cross sections of atomic iodine [43]. (Solid curve: single ionization; dashed curve: single and double ionization; open squares: experimental single ionization cross section by Hayes et al [67]; open diamonds: model potential cross section by Joshipura and Limbachiya [68]; open triangles: orthogonalized plane-wave Born cross sections by Bartlett and Stelbovics [69]; crosses: single ionization by Huo [70].)

Figure 15 plots the ionization cross sections for single, doubly and triply charged ions from electron impact with atomic iodine. The total ionization cross section is the sum of the three ionization cross sections. The doubly and triply charge ionization cross sections have been scaled to present them all on the same plot (hence the multiplier listed in the figure).

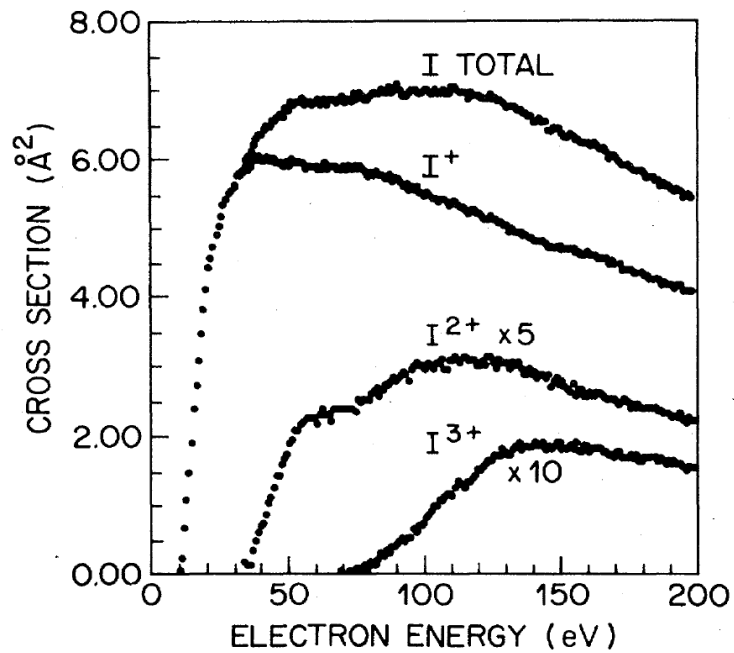


Figure 15: Cross sections for single, double and triple ionization of I, and the total ionization cross section from 0 to 200 eV [67].

Figure 16 shows the ionization cross section for electron impact of molecule iodine resulting in a molecular ion ($e^- + I_2 \rightarrow I_2^+$). The cross sections are shown for electron energies from the ionization potential (9.31 eV) to ~5000 eV.

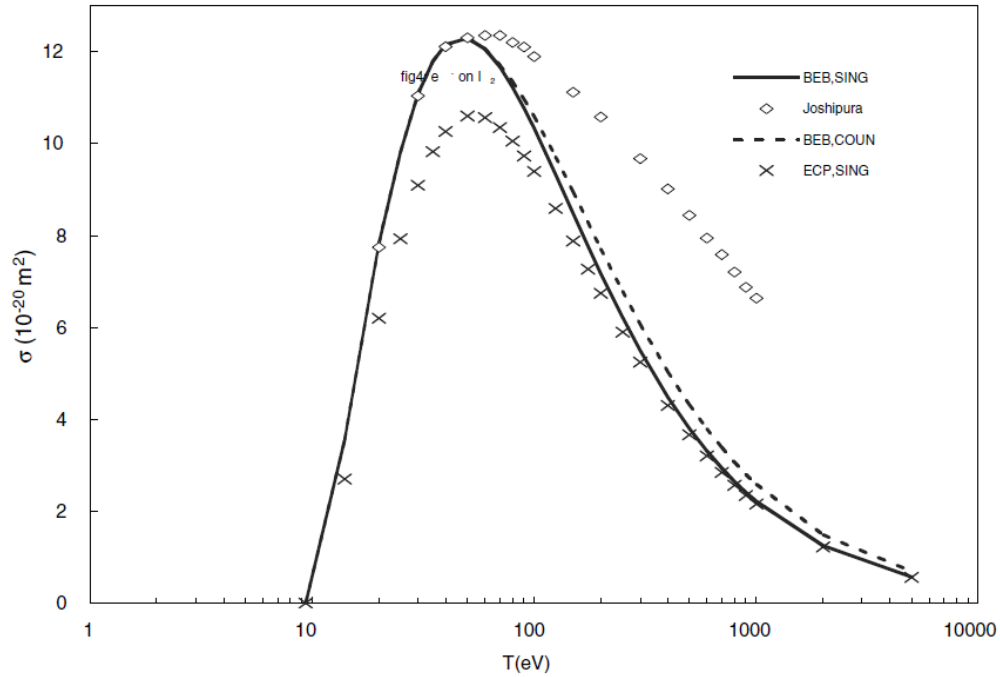


Figure 16: Ionization cross section of I_2 [43]. (Solid curve: present work for single ionization; dashed curve: present work for single and double counting ionization; crosses: ECP(d) single ionization; open diamonds: model potential cross section by Joshipura and Limbachiya [68].)

Figure 17 plots the cross sections for two excited molecular states and molecular ionization. The two excited states, identified by their respective transitions, are $B^3\Pi_{0+u}$ which relaxes to the ground state $X^1\Sigma_g^+$ and $E^3\Pi_{0+g}$ which relaxes to the B state. Also identified by its transition is the molecular ion $A^2\Pi_{3/2u}$ which relaxes to the ground state. These cross sections are plotted from their respective threshold energy to 100 eV.

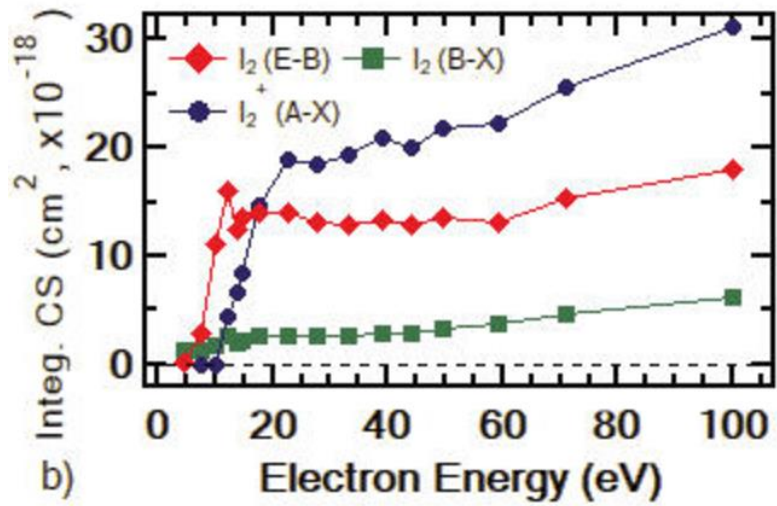


Figure 17: Electronic excitation and ionization cross sections for molecular iodine (e^-+I_2) [66].

Figure 18 plots the dissociative attachment cross section electron impact with molecular iodine from several experiments. Buchdahl [71] used a total ionization tube method and Healy measured the attachment of a swarm of electrons directed through a gas by an applied electric field [72].

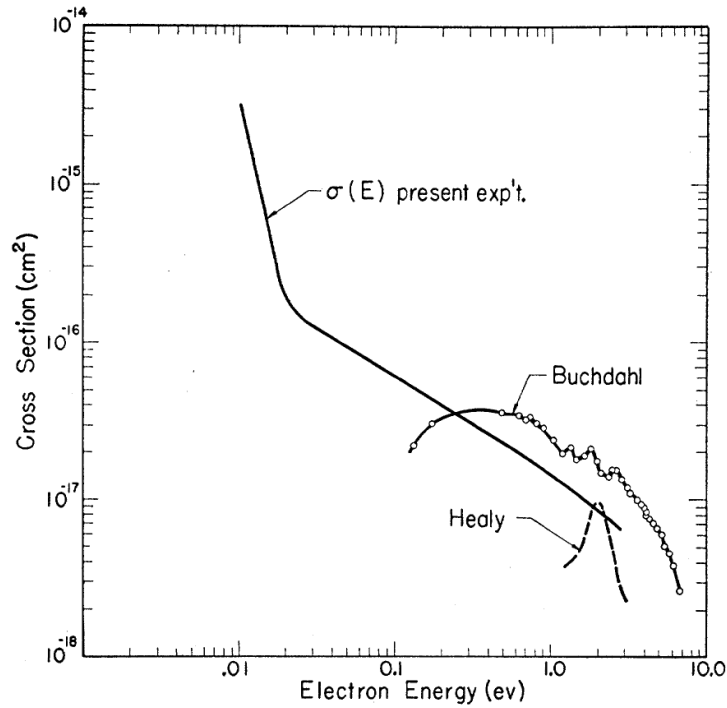


Figure 18: Dissociative electron attachment cross section for iodine [73] (Buchdahl [71] and Healy [72]).

Figure 19 shows a typical I⁻ capture peak, plotted against a measured SF₆⁻ capture peak for comparison and experimental validation. The resonant capture process is plotted from the onset energy (0.03±0.03 eV) to the upper energy limit (1.08±0.04 eV) [74]. The energy corresponding to the maximum capture cross section is 0.34±0.07 eV [74]. This measurement is important for any process resulting a negative iodine ion.

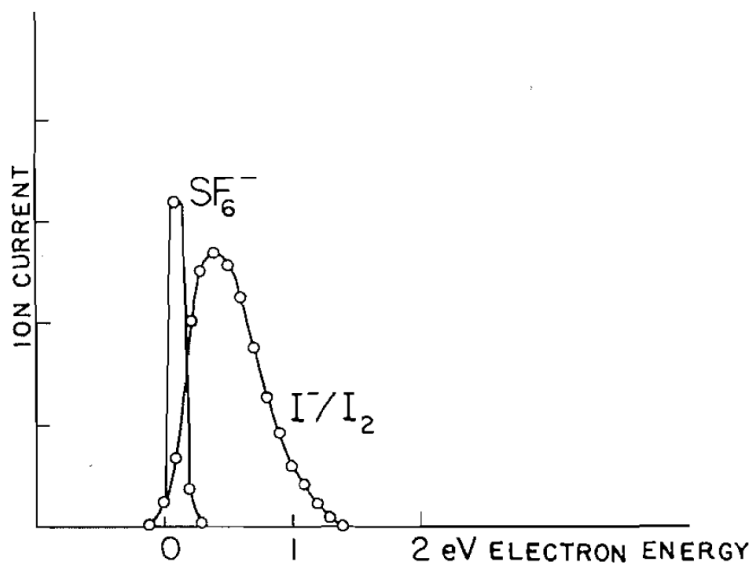


Figure 19: Resonant capture peak for the formation of I^- from iodine by electron impact (SF_6^- for comparison) [74].

Figure 20 shows the potential energy curves for electron attachment leading to negative ion formation.

Highlighted with the inset is the vertical energy band over which the resonant capture peak is measured.

The resonant capture process is described in detail by Frost and McDowell [65].

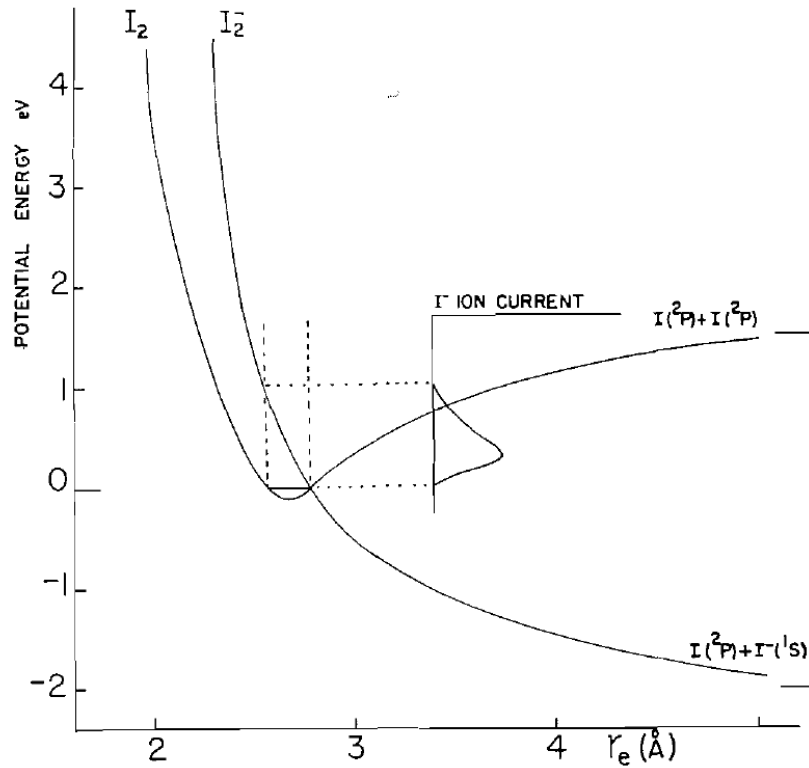


Figure 20: Potential energy diagram to illustrate the formation of I^- from iodine by resonant capture [74].

Figure 21 shows the cross sections for the production of atomic halides from several halogen molecules. A unique feature in the iodine cross section is the rapid rise of negative ion current beginning at 9 eV. It is postulated that the cause of this enhancement in the production of negative ions is caused by ion-pair formation [75]. This may have implications for the production of negative ions in the plume of a hollow cathode since this phenomenon spans the electron energy range on interest in hollow cathode discharges.

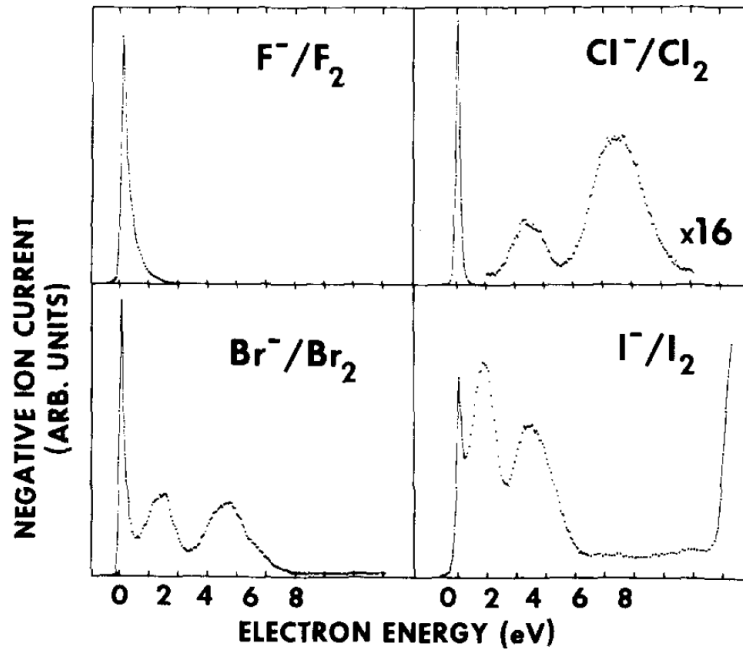


Figure 21: Cross section for production of atomic halide ions from halogen molecules [75].

In more complex plasmas, such as ones including iodine molecules, many reaction products exist for collisions involving electrons including vibrational excitation, electron attachment and dissociation. Knowledge of cross sections for specific reactions such as electron attachment, which is responsible for the formation of negative ions, is critical to understanding the dominant processes in the plasma. In typical plasma thrusters, negative ion formation is undesirable as electric fields are tailored to accelerate positive ions and accelerating negative ions into surfaces will increase degradation rates due to sputtering. In ion thrusters, negative ions effectively reduce the Bohm speed of ions entering the accelerating grids and reduce the beam yield [76]. Typically, electron attachment is most likely at low electron energies (<10 eV), which is exactly the electron energies typically found in electrostatic thrusters and hollow cathodes. Formation of negative ions will consume electrons, which would typically inhibit ionization; therefore, electron attachment is considered an efficiency loss at best and at worst it will quench the plasma and extinguish the discharge [77].

Chapter 3 Experimental Methods

Electrostatic probe plasma diagnostics cover a wide range of invasive tools most often used to measure current-voltage characteristics when inserted in a plasma under study. This data can be used to either directly infer a plasma property (e.g. floating potential) or to provide data that can be used to calculate plasma properties (density, temperature, energy distribution) through the use of appropriate theories and methods. Whenever a probe is inserted into a plasma it is imperative to understand the extent to which this will disturb the local plasma and to properly account for this perturbation in subsequent analysis. It is also important to consider the plasma that is being interrogated and understand how the characteristics of the plasma can affect the probe measurements. This chapter describes the experimental methods employed to characterize the hollow cathode plume and interpretation of the measurements.

3.1 Emissive Probes

Emissive probes have long been used to determine plasma parameters due to their simplicity and ease of interpretation and implementation. Electron-emitting probes can be electrically floating or biased with respect to some reference potential, typically ground potential. Several methods can be used to determine the plasma potential and other plasma parameters depending on the type of probe used and post-processing of the information obtained from the probe. Floating emissive probes provide a direct, time-resolved measurement of the plasma potential using a very simple measurement circuit and require little post-processing. This section describes the floating point technique and associated theory for an emissive probe in the strongly emitting regime, what plasma parameters can be obtained from this technique and uncertainty analysis.

3.1.1 Theory of Operation—Floating Point Technique

Emissive probes provide a direct measurement of the floating potential using a thermionically emitting filament immersed in the plasma. The concept of an electron-emitting probe first proposed by Langmuir [78], and Kemp and Sellen [79] were one of the first to implement such a technique. In this technique, an

electrically isolated, emitting wire is used to provide a direct measurement the floating potential, which for a strongly emitting probe is approximately equal to the plasma potential. The floating point technique is the most widely used emissive probe method due to the ease of implementation and broad range of applicability in a variety of plasma conditions [80]. Typically, a loop of tungsten wire is heated to emission temperatures by passing a current through it. For the floating point method, the entire measurement circuit is isolated from facility ground and floats very close to the plasma potential.

To understand the measurement technique it is illustrative to begin with a planar geometry. For a non-emitting planar surface, both ions and electrons are collected, and a sheath will develop as described in Section 2.4.2 to ensure that the electron and ion current fluxes are balanced. For an emitting surface, the inclusion of an additional flux term is necessitated by the emitted electrons. As the temperature of the surface is increased, the flux of emitted electrons increases. This additional flux will change the floating potential of the surface and hence the sheath structure. The potential difference between the floating potential and plasma potential is given by

$$\Delta V = -\left(\frac{T_e}{e}\right) \ln\left(\frac{1 - \Gamma}{\sqrt{2\pi m_e/m_i}}\right) \quad (3-1)$$

where Γ is the ratio of emitted and collected electron flux [80]. As the emission current is increased, the floating potential reaches a value close to the plasma potential. This critical, emitted flux is given by

$$\Gamma = 1 - 8.3 \sqrt{\frac{m_e}{m_i}} \quad (3-2)$$

This critical flux reduces the difference between the floating potential and plasma potential to a value on the order of the electron temperature ($\Delta V \approx -T_e$). More rigorous analysis, which includes the sheath [81] and pre-sheath [82] at critical emission shows the difference between the floating potential and plasma potential is given by

$$\Delta V \approx -1.8T_e \quad (3-3)$$

A corresponding rigorous solution has not been established for the case of the cylindrical geometry, but the phenomenon is the same—as the electron emission increases the floating potential rises and reaches a value near the plasma potential. For the cylindrical geometry the sheath conditions have been considered in the saturation condition [83]. If the probe floating potential is lower than the local plasma potential, the probe surface will repel the emitted electrons and appear as ion current to the probe. When the potential of the probe is positive, relative to the local plasma potential, emitted electrons will be collected by the probe, leaving the collected electron current unaffected. The electron emission cannot be increased arbitrarily due to space-charge limitation around the probe. In this case a double sheath will form around the probe and the slow-moving electrons emitted by the probe will be returned to the surface. The sheath potential structure in the saturation regime is shown in Figure 22. The floating emissive probe with cylindrical geometry still provides a direct measurement of the plasma potential within approximately $1T_e$ [84].

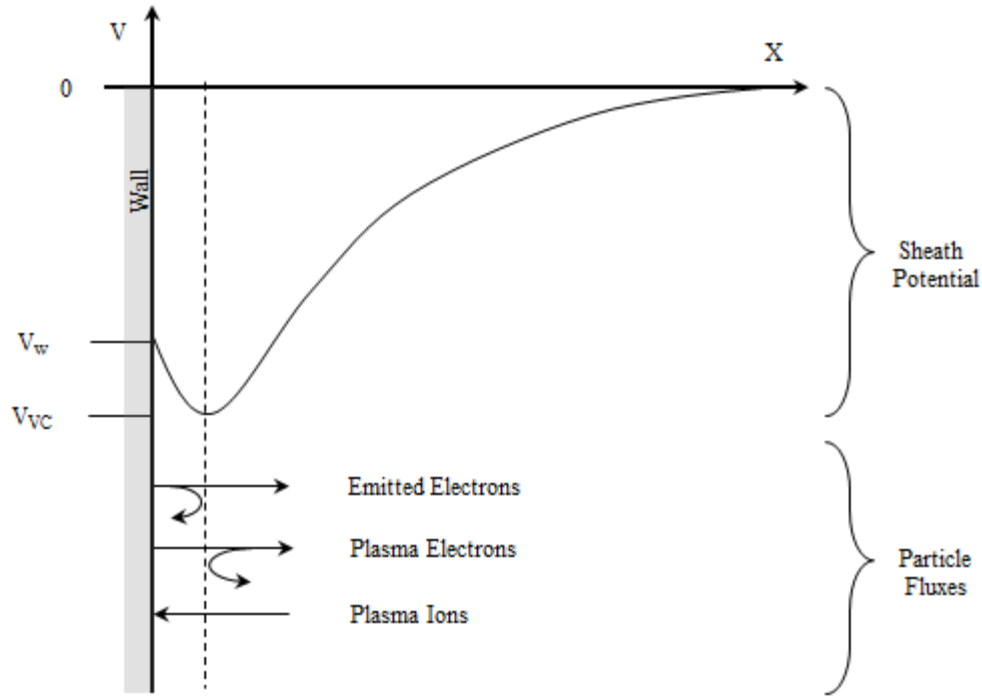


Figure 22: A schematic diagram of the sheath potential (V) and particle fluxes near an emitting surface [85].

The floating point method is capable of following fast temporal fluctuations in plasma potential in the low RF regime. The main limitation of the frequency response of the probe is its own stray capacitance generated by the fluctuating plasma potential in the vicinity of probe surface [79]. It is possible to overcome significant errors due to stray capacitance by using high impedance between the probe tip and measurement circuitry. When the probe emission is sufficient such that the floating potential is on the order of the electron temperature as described above, temporal measurements of the plasma potential can be performed. This is a distinct advantage of using an emissive probe and the floating point method.

3.1.2 Uncertainty Analysis

As described in the previous section, it is common to estimate the plasma potential by the measured floating potential, which for a probe in the limit of strong emission, will lie within approximately $1T_e$ of the actual plasma potential [84]. A more conservative range for this value, reported in the literature, is

that the difference between the floating potential and plasma potential for a probe in the strongly emitting regime lies between $1.5-2T_e$ [86]. If an emissive probe is in the regime where the floating potential is (from the associated theory just presented) within $1.5T_e$ of the plasma potential, then the uncertainty on the electron temperature must be known to determine the uncertainty of the plasma potential measurement. An uncertainty on the electron temperature measurement can be estimated using the floating potentials from both hot and cold probes to calculate the electron temperature. Following the uncertainty analysis for the calculation of the electron temperature using cold and hot emissive probes by Sheehan et al. [86], the maximum uncertainty in the “real” electron temperature, calculated from an experimentally measured electron temperature for a planar probe model is $\pm 17\%$.

$$\Delta T_e = \pm 0.17 T_e^{exp} \quad (3-4)$$

Here, T_e is the “real” electron temperature and T_e^{exp} is the experimentally measured electron temperature. Therefore, for a plasma with an experimentally measured electron temperature of 10 eV, the uncertainty in the electron temperature is ± 1.7 eV.

The ultimate uncertainty in the electron temperature depends on the particular method and probe used to calculate the electron temperature. For this work, the electron temperature was calculated by several methods including the Slope Method and EEDF from a Langmuir probe, for which the uncertainty analysis is not as straightforward and described in the following section (Section 3.2.5). It would be inappropriate to use a specific electron temperature, measured using the Langmuir probe, to calculate the plasma potential from the floating potential measurements, since the floating potential measurements cover a broad range of cathode operating conditions and the electron temperatures calculated using the Langmuir probe were for a few, discrete operating conditions. However, it is reasonable to assume a range of electron temperature based on those measurements for the purpose of estimating a total uncertainty on the plasma potential measurements. Based on the EEDF results it is reasonable to assume an electron temperature up to 2 eV with an uncertainty of 20% (± 0.4 eV) in the plasma surrounding the emissive probe for all the test conditions.

To estimate the uncertainty in the measured value of the floating potential the emissive probe measurement circuit was calibrated using a linear least squares regression fit to measured values using a known input voltage. An uncertainty of 0.05 V (ΔV_{sig}) is assumed for the measured values input into the regression analysis, which is a conservative uncertainty for calibrated FLUKE voltmeters. This procedure for the linear regression analysis follows the work by Bevington and Robinson [87], but can be found in most data analysis textbooks. The linear function for the regression analysis is

$$y(x) = mx + b \quad (3-5)$$

Where x and y are the measured data, m is slope, b is the intercept and σ_m and σ_b are the uncertainties in their respective coefficients. The results of the linear regression are listed in Table 6.

Table 6: Emissive probe measurement circuit uncertainty values based on linear regression analysis

ΔV_{sig}	m	σ_m	b	σ_b
0.05	11.061	0.026	1.423	0.044

The equation to recover the floating potential measurement from signal measured by the emissive probe circuit is then

$$V_f = mV_{sig} + b \quad (3-6)$$

The total uncertainty in the floating potential measurement is then dependent on the value of the signal produced by the measurement circuit and determined using the following equation.

$$\delta V_f^2 = \delta V_{sig}^2 m^2 + \delta b^2 (1)^2 + \delta m^2 (V_{sig})^2 \quad (3-7)$$

Thus, the plasma potential estimate from the floating potential measurement and electron temperature is

$$\phi_p = V_f + 2T_e \quad (3-8)$$

And the uncertainty in the plasma potential estimate using Equation (3-8) is

$$\delta \phi_p^2 = \delta V_f^2 + 4\delta T_e^2 \quad (3-9)$$

Assuming a floating potential measurement of 100 V, using Equation (3-7) the total uncertainty in the measurement of the floating potential is $\delta V_f = \pm 0.27 V$. If one assumes a reasonable range of electron temperatures of 1 eV to 2 eV based on the electron temperatures measured by the Langmuir probe, this would dominant the uncertainty in the plasma potential. With the uncertainty in both the floating potential and electron temperature known (assuming $\delta T_e = \pm 1 eV$ based on Langmuir probe measurements), the plasma potential is $\delta \phi_p = \pm 2 V$. Based on this uncertainty analysis, and given the measured plasma conditions, it is reasonable and conservative to assign an uncertainty of $\pm 10\%$ since the emissive probe circuit can only measure potentials up to 100 volts. This is comparable to the low end of the range (12-20%) reported by Sheehan et al [80].

To calculate the RMS of the floating potential, which is reported in some of the results, built in MATLAB function “rms” was used. Where the RMS of a set of data where the mean has been subtracted off is defined as

$$x_{RMS} = \sqrt{\frac{1}{N} \sum_{n=1}^N x^2} \quad (3-10)$$

For a signal where $y = x^2$, following simple error propagation using rules for series and power, the uncertainty in the RMS calculation is

$$\delta x_{RMS}^2 = \delta \bar{y}^2 \left(\frac{1}{2\sqrt{\bar{y}}} \right)^2 \quad (3-11)$$

Where

$$\delta \bar{y}^2 = \left(\frac{1}{\sum 2\delta x * x} \right)^2 \quad (3-12)$$

And x is the floating potential measurement and δx uncertainty in the measurement of the floating potential. This analysis results in an uncertainty in the RMS calculation on the order of 10^{-5} , which shows that the uncertainty in the RMS calculation is negligible for all measurements.

3.2 Langmuir Probes

Given its wide range of applicability the electrostatic Langmuir probe has long been the most widely used diagnostic tool for measuring local many plasma properties. Irving Langmuir first developed the Langmuir probe during his work with plasmas during the first quarter of the twentieth century. Several types of Langmuir probes exist and are often identified by the number of electrodes: single, double, triple and even quadruple. Each type has advantages and disadvantages and can be used to measure different sets of plasma properties. Each requires unique experimental methods and considerations to ensure accurate results. In this work, a single cylindrical Langmuir probe was used to determine several plasma parameters as well as the electron energy distribution function.

3.2.1 Theory of Operation

The Langmuir probe is probably the simplest of all probes to build and conceptualize; however, its physical simplicity is accompanied by the complexity involved in interpretation of the current-voltage signal, commonly referred to as the “I-V curve,” characteristic or trace. The Langmuir probe consists of a small wire and probe holder that is inserted into the plasma. The probe wire or “tip” is then biased with a voltage source and current is collected. This current is measured as a function of the applied probe voltage. An ideal I-V curve is shown in Figure 23 below.

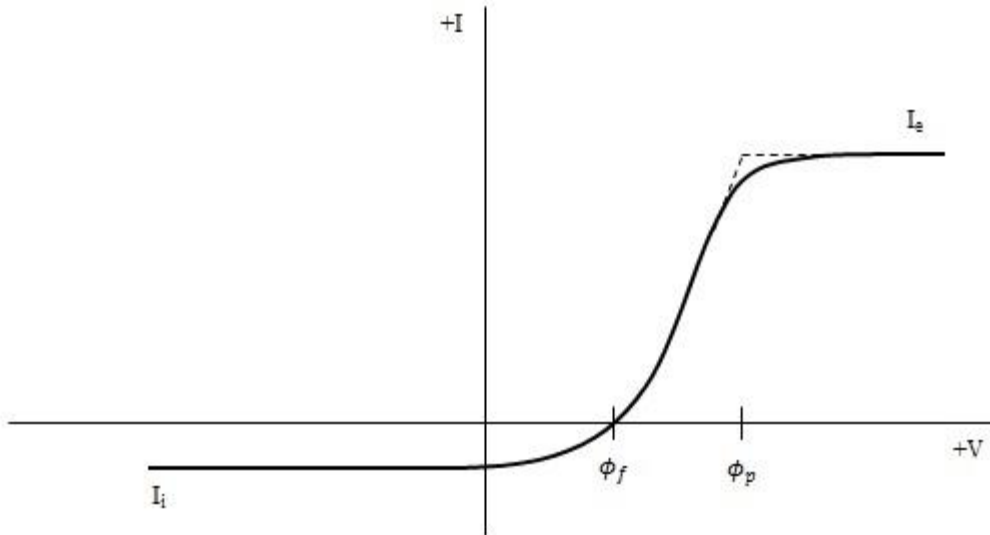


Figure 23: Ideal single Langmuir probe trace.

By convention electron current is plotted as positive. Moving from low to high values along the axis representing probe bias; when the probe has a large negative bias, even the most energetic electrons are repelled and mostly ions are collected, this region is known as the *ion saturation* region, I_i . As the probe bias moves more positive ions are still collected but more energetic electrons now arrive at the probe. When both ion and electron flux to the probe are equal, the probe is at the floating potential, ϕ_f . Moving still more positive, into what is known as the transition region, less energetic electrons are able to reach the probe until the probe reaches the plasma potential, ϕ_p . For probe biases at or above the plasma potential the probe theoretically collects all incident thermal electrons. This region is known as the *electron saturation*, I_e region as the collected ion current is negligible. Above the plasma potential, the electron current continues to increase due an expanding sheath surrounding the probe. The plasma potential is an extremely important parameter as it is the reference for all electron energy measurements. In this general description of the Langmuir probe characteristic, the plasma potential is assumed to be a steady value.

The single Langmuir probe can provide a measurement of the plasma number density, floating potential and plasma potential. Under certain conditions, the electron temperature can be calculated directly from

the probe trace as well. The probe trace can be used to calculate the EEDF, even for plasmas where electron energy distribution deviates from a Maxwellian distribution.

The plasma potential can be obtained from the Langmuir probe trace by identifying the “knee” of the I-V curve. The knee is determined by the inflection point between the transition and electron saturation regions. The ideal probe trace shown in Figure 23 indicates a rather sharp inflection point and the plasma potential can easily be identified. Figure 24 shows how the probe tip geometry can affect the sharpness of the knee and hence the ease with which the plasma potential can be identified [88].

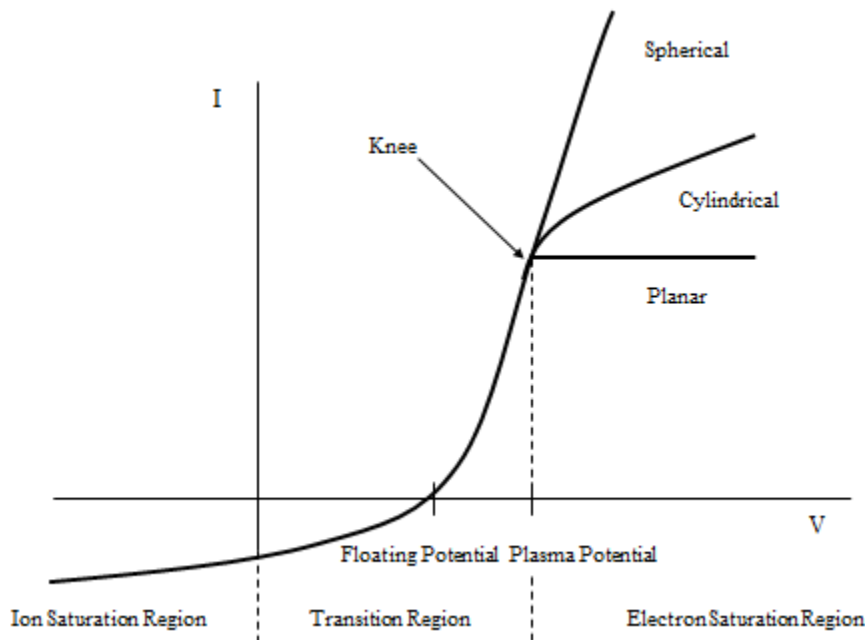


Figure 24: Comparison of single Langmuir probe traces with various geometries (adapted from [88]).

For the idealized case of a perfectly planar, one-dimensional probe geometry, the knee will be sharp and well-defined. The knee for spherical and cylindrical probes is much more difficult to distinguish due to an increasing effective collection area as the probe bias increases. When the knee is not so clearly defined the maximum of the first derivative of probe current with respect to probe voltage can be used to determine the plasma potential. Also, the zero crossing of the second derivative of the probe current with

respect to voltage will yield the plasma potential. Other plasma conditions can affect the probe trace including a strong magnetic field and RF potentials [9].

3.2.2 Plasma Density

To obtain the plasma density in a quasi-neutral plasma, either the ion or electron density can be obtained from the Langmuir probe trace. Two commonly employed theories to interpret probe data and calculate plasma density are Orbit Motion Limited (OML) theory [89] and Thin Sheath theory [90]. Each use saturation conditions of the Langmuir probe trace.

Thin Sheath Theory

Among the probe theories to determine plasma densities, thin-sheath theory is the simplest and first developed by Langmuir [90]. For thin-sheath theory to be applicable the thickness of the plasma sheath surrounding the probe is negligible. When a probe is inserted into a plasma a sheath will develop around it, resulting in a gradient in the plasma potential that can extend for up to several Debye lengths. Chen suggests that the probe size (r_p) should be much larger than the Debye length and recommends that the ratio of probe radius to Debye length (r_p/λ_D) be 10 or larger for thin-sheath theory to be applicable [83]. Other assumptions for thin-sheath theory include: a Maxwellian distribution of electrons, quasi-neutrality in the vicinity of the probe, the probe is not emitting electrons, the probe size is much smaller than the mean free path of ions and electrons, (i.e. the plasma is collisionless), the ion temperature is much less than the electron temperature, and a negligible ion and electron drift velocity [90]. These criteria are listed in Table 7.

Using the Boltzmann relation and conservation of energy to determine the ion density and velocity, respectively, the flux to the probe can be described by the following relation:

$$\Gamma_i(x) = n_i(x)v_i(x) = n_0 \exp\left[\frac{e\phi(x_s)}{k_b T_e}\right] \left[\frac{-2e\phi(x_s)}{M_i}\right]^{1/2} \quad (3-13)$$

To determine the electron flux to the probe, the random flux is used and electron thermal speed is substituted for the electron velocity as determined from the Maxwellian velocity distribution. The electron flux to the probe is written as:

$$\Gamma_e(x) = \frac{1}{4} n_e v_e = \frac{1}{4} n_0 \exp \left[\frac{e\phi(x_p)}{k_b T_e} \right] \left[\frac{8k_b T_e}{\pi m} \right]^{1/2} \quad (3-14)$$

Combining the electron and ion flux, and multiplying by the areas of the probe A_p and sheath A_s yields an expression for the total collected current by the probe.

$$I = e \left\{ -\frac{1}{4} A_p n_0 \exp \left[\frac{e\phi(x_p)}{k_b T_e} \right] \left[\frac{8k_b T_e}{\pi m} \right]^{1/2} + A_s n_0 \exp \left[\frac{e\phi(x_s)}{k_b T_e} \right] \left[\frac{-2e\phi(x_s)}{M_i} \right]^{1/2} \right\} \quad (3-15)$$

In this equation $\phi(x_p)$ is the potential at the probe and $\phi(x_s)$ is the potential at the sheath edge. The potential at the sheath edge can be obtained by solving Poisson's equation inside the sheath. Substituting the potential at the sheath edge and assuming that the probe area is similar to the sheath area ($A_p \approx A_s$) the following relation is obtained for the total current collected by the probe.

$$I = -eA_p n_0 \left\{ \frac{1}{4} \exp \left[\frac{e\phi(x_p)}{k_b T_e} \right] \left[\frac{8k_b T_e}{\pi m} \right]^{1/2} - n_0 \exp \left(-\frac{1}{2} \right) \left[\frac{k_b T_e}{M_i} \right]^{1/2} \right\} \quad (3-16)$$

From this expression, electron and ion saturation currents can be identified.

$$I_{se} = -\frac{1}{4} eA_p n_0 v_e \quad (3-17)$$

$$I_{si} = eA_p n_0 v_i \exp \left(-\frac{1}{2} \right) = 0.61 eA_p n_0 v_i \quad (3-18)$$

Then,

$$I = I_{se} \exp \left[\frac{e\phi(x_p)}{k_b T_e} \right] + I_{si} \quad (3-19)$$

From these equations for probe current several plasma parameters can be determined including electron temperature, plasma density and floating potential. Subtracting off the ion current and solving for slope

of Equation (3-16) in the exponential region will yield the electron temperature. Using the calculated electron temperature in Equation (3-18) will provide the plasma density. To determine the floating potential, (3-16) can be set equal to zero and solved for $\phi(x_p)$.

Orbit Motion Limited (OML) Theory

Orbit Motion Limited theory was first developed by Langmuir and Mott-Smith [91], and improved on by several others including Allen [89]. OML theory accounts for a finite ion temperature in the bulk plasma and hence a non-zero velocity at the sheath edge. The criteria for OML are listed in Table 7. OML theory accounts for these effects by introducing the concept of an absorption radius surrounding the probe as shown in Figure 25. The absorption radius, or impact parameter, h represents the maximum approach distance a charged particle can have when passing an attracting probe (probe potential is the opposite sign of the passing charged particle) and still make it to the probe surface. The impact parameter is considered the effective probe radius. Figure 25 shows the impact parameter and charged particle trajectory in the vicinity of a cylindrical probe.

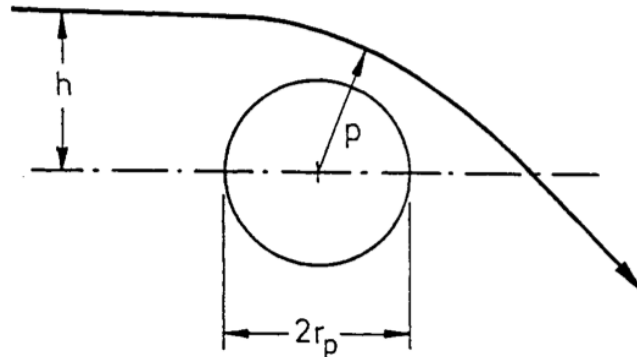


Figure 25: Charged particle trajectory in the vicinity of the collecting probe for OML theory [89].

A full derivation of OML theory can be found in Allen [89], beginning from conservation of energy and angular momentum, and assuming a Maxwellian distribution of charged particles in the bulk. Similar to thin-sheath theory, OML assumes similar conditions on the plasma including: the thickness of the plasma sheath surrounding the probe is large compared to the probe ($(r_p/\lambda_D) \lesssim 3$) [92], and a collisionless and

quasineutral plasma [83]. The result is a relationship between the plasma density and the ion or electron current collected by the probe.

$$I_i = 2\pi n_0 r_p l e \left(\frac{k_b T_i}{2\pi M_i} \right)^{1/2} \frac{2}{\sqrt{\pi}} \left(1 - \frac{e\phi_p}{k_b T_i} \right)^{1/2} \quad (3-20)$$

$$I_e = 2\pi n_0 r_p l e \left(\frac{k_b T_e}{2\pi m} \right)^{1/2} \frac{2}{\sqrt{\pi}} \left(1 + \frac{e\phi_p}{k_b T_e} \right)^{1/2} \quad (3-21)$$

Equation (3-20) shows that a plot of I^2 versus ϕ_p should be a straight line. In the ion saturation region of the probe current, the slope of a linear curve fit of I^2 versus ϕ_p can be used to determine the ion density and, for a quasi-neutral plasma, the plasma density.

Table 7: Summary of ion collection theory criteria

Method	$\frac{r_p}{\lambda_D}$	$\frac{\lambda_{ei}}{d_p}$	$\frac{\lambda_{en}}{d_p}$	Electron Population
Thin Sheath	> 10	$\gg 1$	$\gg 1$	Maxwellian EEDF
OML	$\lesssim 3$	$\gg 1$	$\gg 1$	Maxwellian EEDF

For some plasmas, the orientation of the probe relative to the plasma can affect the current collected by the probe. In general, probe alignment must be considered with a plasma where there is significant drift velocity of the ions $U_\infty/U_{Bohm} > 1$, or the plasma is flowing. These plasmas are often found in electric propulsion thrusters, but not in hollow cathode plumes where there is no extraction or acceleration mechanism for the bulk ions. Alignment of the probe parallel to this velocity largely mitigates most flowing plasma effects [92].

3.2.3 Druyvesteyn Method

As discussed in 2.4.4 the EEDF can be used to calculate numerous plasma properties and is critical in characterizing collisional processes in any particular plasma. In real plasmas, the EEDF can often deviate far from a Maxwellian distribution, making knowledge of the actual EEDF important to accurately characterize them. Druyvesteyn developed a method of determining the EEDF for a given plasma using

the second derivative of the collected Langmuir probe IV curve, known as the *Druyvesteyn method* [93]. Druyvesteyn has historically been credited with being the first to discover the relationship between the distribution function and second derivative of the probe current; however, Mott-Smith and Langmuir were actually the first to demonstrate this relationship [91].

The Druyvesteyn method has been derived in several texts including Chabert and Braithwaite [9], and Lieberman and Lichtenberg [56]. In summary, electrons must have sufficient energy to reach the probe, which is proportional to the applied probe voltage and dictates the collected current. The total collected probe current can be written in the following form [56]:

$$I_e = eA_p \int_0^{2\pi} d\phi \int_{v_{min}}^{\infty} v^3 f(v) dv \int_0^{\theta_{max}} \cos \theta \sin \theta d\theta \quad (3-22)$$

where $v_{min} = \left(\frac{2eV}{m}\right)^{1/2}$, $\theta_{max} = \cos^{-1}\left(\frac{v_{min}}{v}\right)$, ϕ is the azimuthal angle and A_p is the exposed probe surface area. Here, v_{min} represents the minimum velocity required for an electron to reach the probe surface. By integrating over all angles, the following expression is obtained for the collected probe current [56].

$$I_e = 2\pi A_p \int_{v_{min}}^{\infty} \left(1 - \frac{v_{min}^2}{v^2}\right) v^3 f(v) dv \quad (3-23)$$

Again, as in the derivation of the EEDF from the velocity distribution in Section 2.4.4, an expression for the distribution function in terms of energy rather than velocity is desired. Using a simple substitution for the particle's energy, expressed in electron volts, the collected probe current becomes [56]

$$I_e = \frac{2\pi e^3}{m^2} A_p \int_V^{\infty} \varepsilon \left[\left(1 - \frac{V}{\varepsilon}\right) f(v(V)) \right] d\varepsilon \quad (3-24)$$

Where V is the probe bias voltage with respect to the local plasma space potential, ϕ_s ($V = \phi_s - \phi_p$). This expression can then be differentiated twice with respect to the probe voltage to obtain the following relationship.

$$\frac{d^2 I_e}{dV^2} = \frac{2\pi e^3}{m^2} A_p f(v(V)) \quad (3-25)$$

This expression can then be written as a function of the particle's energy. First, the number of particles in a unit volume of energy space can be equated to the number of particles in a unit volume of velocity space using the appropriate density function $F(\varepsilon)$. This equality can be used to express this density function as [56]

$$F(\varepsilon) = 4\pi v^2 f(v) \frac{dv}{d\varepsilon} \quad (3-26)$$

Substituting the derivative of the kinetic energy, $\frac{dv}{d\varepsilon} = \left(\frac{1}{2m\varepsilon}\right)^{1/2}$ in this expression results in the following expression for the particle probability (or density) distribution function in energy space.

$$F(\varepsilon) = 4\pi \frac{2\varepsilon}{m} \left(\frac{1}{2m\varepsilon}\right)^{1/2} f(v) \quad (3-27)$$

Solving Equation (3-24) for the velocity distribution, $f(v)$, and substituting into the above expression along with $\varepsilon = eV$, yields the following relationship.

$$F(\varepsilon) = \frac{4}{e^2 A_p} \left(\frac{mV}{2e}\right)^{1/2} \frac{d^2 I_e}{dV^2} \quad (3-28)$$

This is known as the *Druyvesteyn Formula* and it relates the second derivative of the probe current (differentiated with respect to the probe bias voltage) to the EEDF. Calculating the EEDF also requires knowledge of the plasma potential, which must be subtracted from the applied probe bias. The plasma potential can be determine using the zero crossing of the second derivative of the probe current with respect to the probe bias [83]. From the EEDF several plasma parameters can be calculated including electron number density, electron temperature and reaction rates for known collisional processes.

The number is calculated by

$$n_e = \int_0^{\infty} F(\varepsilon) d\varepsilon \quad (3-29)$$

and the electron temperature can be determined by averaging over the EEDF [56].

$$T_e = \frac{2}{3} \frac{1}{n_e} \int_0^{\infty} \varepsilon F(\varepsilon) d\varepsilon \quad (3-30)$$

where $\varepsilon = V - \phi_s$.

3.2.4 Second Harmonic Method

From the previous section (3.2.3), it is clear that an accurate determination of the second derivative of the Langmuir probe trace is critical for an accurate calculation of the EEDF. The Langmuir probe trace can be numerically differentiate; however, this process is considerably amplifies any noise present on the probe traces. Filtering and smoothing techniques often cannot mitigate this noise without distorting the underlying probe trace to the point where the calculated EEDF is inaccurate or wrong. A widely used method to determine the second derivative of a Langmuir probe trace uses a small amplitude (relative to the expected electron temperature), high frequency (1-100kHz) signal superimposed over the probe bias [94, 95, 96, 97, 98]. This signal is commonly referred to as the “ac signal” and that terminology has been adopted for this work. With the ac signal superimposed over the probe signal, the probe current then becomes $I = I(V + A \sin \omega t)$. It can be shown, using a Taylor series expansion, that the second derivative of the probe current is proportional to the amplitude of the second harmonic term in the expansion (last bracketed term in Equation (3-31)) [97].

$$I(V) = I(V) + \frac{A^2}{4} \frac{d^2 I(V)}{dV^2} + \frac{A^2}{64} \frac{d^2 I(V)}{dV^2} + \dots$$

$$\begin{aligned}
& + \left[A \frac{dI(V)}{dV} + \frac{A^3}{8} \frac{d^3I(V)}{dV^3} + \dots \right] \sin(\omega t) + \dots \\
& - \left[\frac{A^2}{4} \frac{d^2I(V)}{dV^2} + \frac{A^4}{48} \frac{d^4I(V)}{dV^4} + \dots \right] \cos(2\omega t) + \dots \\
& + \textit{higher order terms}
\end{aligned} \tag{3-31}$$

In this equation, A is the amplitude of the ac signal and ω is the frequency. A is chosen such that the contribution from the second term in cosine coefficient negligible and is small relative to the expected electron temperature, but not so small that the signal-to-noise ratio is below experimental uncertainty in the measurement. The frequency of the ac signal must also be much higher than the frequency of the dc probe sweep to obtain reasonable resolution for the second derivative, but should be kept lower than one tenth of the plasma frequency to prevent distortion in the EEDF [94]. The ac frequency must also be kept sufficiently low to prevent the RC time constant of the measurement circuit to affect the signal by suppressing the ac signal. A lock-in amplifier is commonly used to measure the amplitude of the signal corresponding to the second derivative of current with respect to voltage. A full derivation of this method can be found in Swift [99].

The plasma EEDF, $F(\varepsilon)$, can be represented by the product of the electron density and normalized distribution function, $f(\varepsilon)$. The normalized distribution function takes the following form when the Druyvesteyn method is applied and a simplification of the electron energy distribution function adopted from Heidenreich [97].

$$f(\varepsilon) \propto \sqrt{\varepsilon} \frac{d^2I}{dV^2} \tag{3-32}$$

where $\varepsilon = \phi_p - V$

The signal corresponding to the second derivative of the Langmuir probe trace produced by the lock-in amplifier cannot be used to directly calculate the normalized distribution function since the signal itself must be normalized. The following normalization constant was used to calculate the normalized EEDF.

$$H = \int_0^{\infty} \sqrt{\varepsilon} A(\varepsilon) d\varepsilon \quad (3-33)$$

The lock-in output was used to generate a function proportional to the EEDF, which was normalized using the normalization constant.

$$f(\varepsilon) = \frac{\sqrt{\varepsilon} A(\varepsilon)}{H} \quad (3-34)$$

Equation (3-34) is used to normalize EEDF as calculated using the second derivative of the probe current generated by the lock-in amplifier.

3.2.5 Uncertainty Analysis

All of the methods, analytical and theoretical, used to determine plasma parameters from the Langmuir probe I-V curve have uncertainties associated with them. Due to a multitude of factors from phenomenon in the physical plasma to measurement techniques and circuitry these uncertainties are often large, functions of other parameters, and difficult to quantify. A concerted effort has been made by the electric propulsion community to standardize the methods of performing correct and accurate Langmuir probe measurements within typical plasmas produced by electric propulsion devices, namely thrusters and cathodes [92]. Several studies investigated the accuracy of measurements made by Langmuir probe compared to other validated measurement techniques such as microwave cavity and interferometry, hairpin resonant probes, radar scattering, spectroscopic and others.

These studies have shown agreement within 3-30% for n_e [100, 101, 102, 103], 10-50% for n_i [104, 105, 100], 2-11% for T_e [106, 107, 108] and 12-20% for ϕ_p [80]. Many of the Langmuir probe analysis techniques have the some or all of the same general requirements including cold ions (for thin sheath

theory), a Maxwellian distribution of electrons, collisionless, nonmagnetized, quasineutral, isotropic and homogeneous. Some or all of these conditions are often not met in plasmas found in EP devices (i.e. hollow cathode plumes). For the hollow cathode in this study, in the near-plume region it is reasonable to assume cold ions since there is no beam extraction, and a collisionless, quasineutral, nonmagnetized and homogeneous plasma.

It will be shown that the distribution of electrons follows a drifting Maxwellian, which violates one of the main underlying conditions for almost all of the probe techniques (see Section 3.2.2) used to determine the plasma density, plasma potential and electron temperature (in some cases). Although the Druyvesteyn method assumes an isotropic plasma (mainly with consideration towards ions), the anisotropic effect on the collected electron current, and subsequently on the EEDF, is mitigated when the cylindrical Langmuir probe is aligned parallel to the drifting electrons [92].

For EEDF's calculated using numerical differentiation the error can be large since the measurement noise is amplified considerably with each differentiation. In many cases, several (10 or more) I-V curves are averaged together to mitigate the measurement error for differentiation; however, for this work, even averaging up to 100 I-V curves together did not reduce the error enough to obtain reliable EEDFs via numerical differentiation and a moving average was required between each differentiation to reduce the noise. As a result of the averaging and moving average between differentiations, the resulting EEDFs were typically "flattened" and tended toward a more Maxwellian-looking distribution. This may have appeared correct, but it was actually the distorted result of excessive smooth techniques. The second harmonic method avoids the errors associated with numerical differentiation of the probe I-V curve, but has its own associated error. Typically, the error in the measured electron temperature from the second harmonic method is attributed to the magnitude of the applied ac signal [99].

A linear regression analysis was performed for the Langmuir probe measurement circuit in the same manner as the emissive probe circuit, Equation (3-5). Table 8 shows the total uncertainty in both the

voltage and current measurements. Where ΔV_{sig} is the measurement uncertainty from a calibrated FLUKE voltmeter, and m is the slope, σ_m is the uncertainty in the slope, b is the y-intercept and σ_b is the uncertainty in the y-intercept for the linear regression, and σ_{tot} is the total measurement uncertainty.

Table 8: Voltage and current measurement uncertainty from linear least squares regression analysis

	Voltage	Current
ΔV_{sig}	0.05	0.05
m	11.1224	23.8926
σ_m	$4.139 \cdot 10^{-4}$	0.0045
b	-0.0875	-0.1441
σ_b	0.0013	0.0013
σ_{tot}	0.06	0.13

For this experiment, each probe sweep (individual I-V curve) has an associated second derivative as determined by the signal from the lock-in amplifier. The continuous signal from the lock-in amplifier was parsed into individual “sweeps” according to the applied probe voltage, resulting in a second derivative for each sweep of the probe voltage. Approximately 100 of these second derivative “sweeps” were averaged together to generate a single, representative second derivative, which was subsequently integrated to calculate the EEDF. This reduced the measurement noise considerably. The standard error as a function of probe bias voltage was calculated for the second derivative measurement. Standard error is given by the following equation

$$\sigma_{\bar{x}} = \frac{\sigma(V_p)}{\sqrt{n}} \quad (3-35)$$

where $\sigma(V_p)$ is the standard deviation in the second derivative as a function of probe voltage and n is the number of samples (or probe sweeps, approximately 100). It is important to report the standard error as a function probe voltage as the uncertainty in the measurement depends largely on the probe voltage, and

subsequently, the electron energy. Figure 26 shows the standard error bars (vertical) over the representative second derivative (averaged, in red).

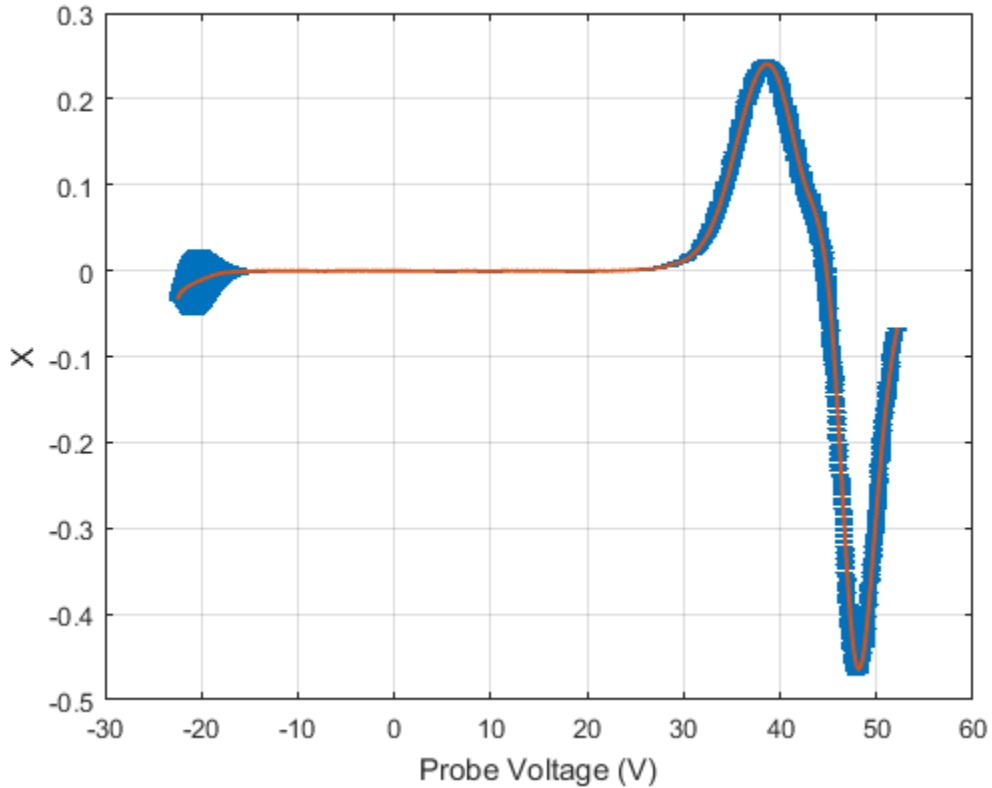


Figure 26: Second derivative of the probe current with respect to voltage, averaged (red) and with error bars

The uncertainty in the second derivative will also influence the calculation of the plasma potential, as the plasma potential is calculated using the zero-crossing of the second derivative. To determine the uncertainty in the plasma potential calculation, the extremes of the uncertainty in the second derivative were used to calculate a minimum and maximum plasma potential. For the case outlined in this section the uncertainty in the plasma potential is ± 0.204 V.

As described in the previous section (Sections 3.2.3 and 3.2.4), the second derivative is then used to calculate the EEDF. The uncertainty in the second derivative and plasma potential will then propagate through this calculation, which requires a definite integral. To conservatively estimate the uncertainty

through the definite integral required to calculate the EEDF, a minimum-maximum approach was implemented. This approach used the minimum and maximum uncertainties in the second derivative and plasma potential (constant) to calculate a “min” and “max” EEDF. The difference between the minimum and maximum distributions, as a function of energy, then yielded the uncertainty in the calculated EEDF as a function of energy. Figure 27 shows the measured distribution function (Experimental) with error bars (every 100 points for clarity) for both the probability and energy.

Also, as described in the previous section, the distribution function can be used to calculate a number of parameters including mean electron energy. As will be shown in the results section, the measured distributions follow a shifted Maxwellian which require an electron temperature and drift energy. The minimum and maximum distributions resulted in the following uncertainties for these key parameters, which include mean electron energy (± 0.02 eV, or $\pm 0.3\%$), electron temperature (± 0.01 eV, or $\pm 1.4\%$) and electron drift energy (± 0.05 eV, or $\pm 0.7\%$).

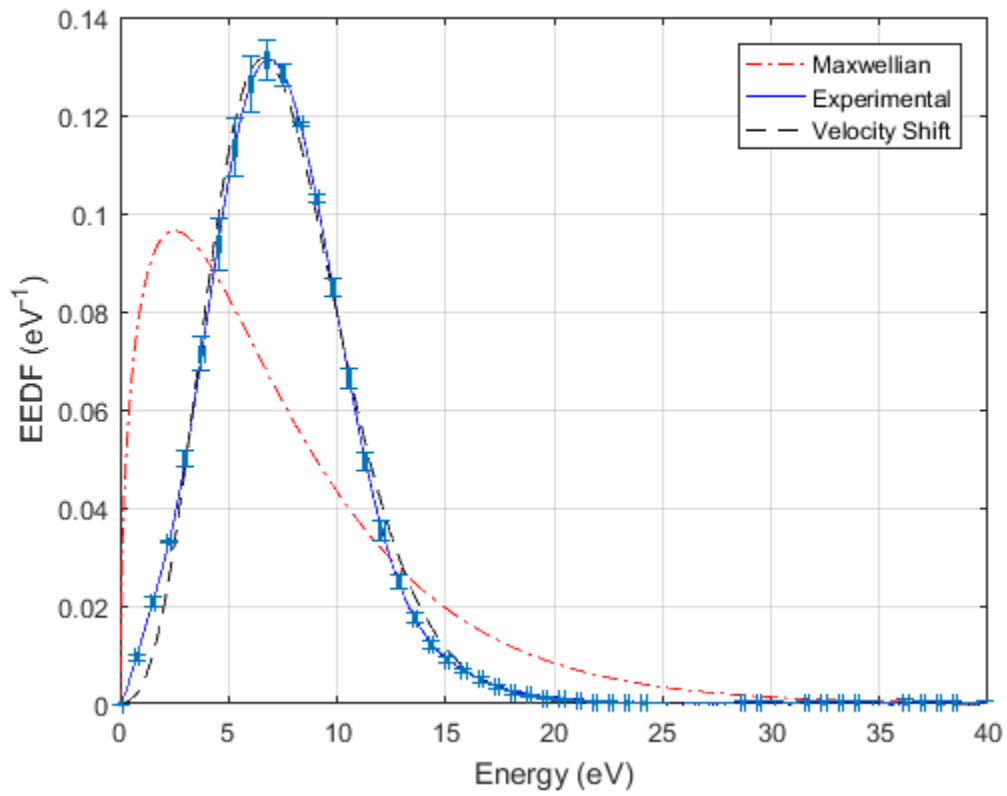


Figure 27: Resulting EEDF with error bars on the experimentally measured distribution (error bars every 100 points for clarity)

Chapter 4 Experimental Instrumentation and Apparatus

This section describes the experimental apparatus and diagnostic tools used to interrogate the cathode plume. Emissive and Langmuir probe construction is detailed, and associated circuitry presented. The three cathodes and their corresponding experimental setup are also described.

4.1 Emissive Probe

The emissive probe used to directly measure the plasma potential consisted of a hairpin loop of tungsten wire and probe holder to electrically isolate and protect the electrical leads. Figure 28 shows a cross section schematic of an emissive probe. A short length of tungsten wire bridges two electrical leads, which are isolated from one another and the surroundings by double-bore alumina tubing with an outer diameter of 0.094" and inner diameter of 0.025" for each of the two bore holes. The bore holes are sufficiently small such that the tungsten wire is forced into physical contact with the electrical leads. The ends of the bore holes (base of the hairpin loop) were sealed with high temperature ceramic paste (Zirconia Ultra Hi-Temp Ceramic Adhesive, MTI Corporation) to prevent unwanted movement of the tungsten wire.

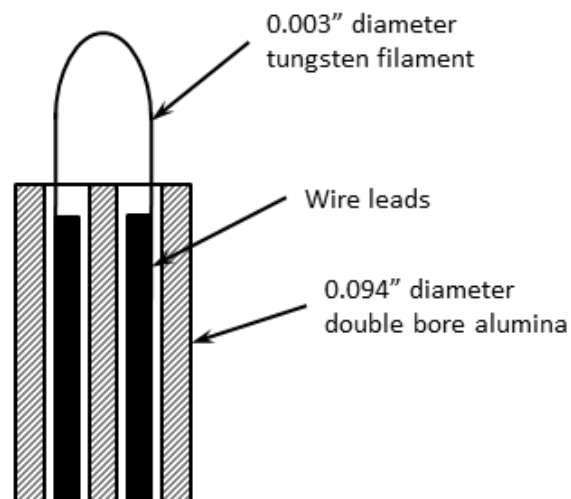


Figure 28: Emissive probe schematic

Standard stranded wire was used for the electrical leads. The thermal insulating jacket was stripped back to expose a length of conductor almost as long as the alumina tubing. The stranded wire was inserted into the alumina tubing up to the insulation to prevent shorting. The unstripped sections of wire were fed through 0.25" stainless steel tubing to a custom electrical box. The alumina was sealed and supported at the base by a Swagelok™ fitting and Teflon™ ferrule to securely hold the alumina tubing in place without the risk of fracture.

The lead wires transitioned to shielded BNC cable at the electrical box at the rear of the emissive probe and connected the filament to the power supply and diagnostic circuitry outside the vacuum tank. The setup is shown in Figure 29.

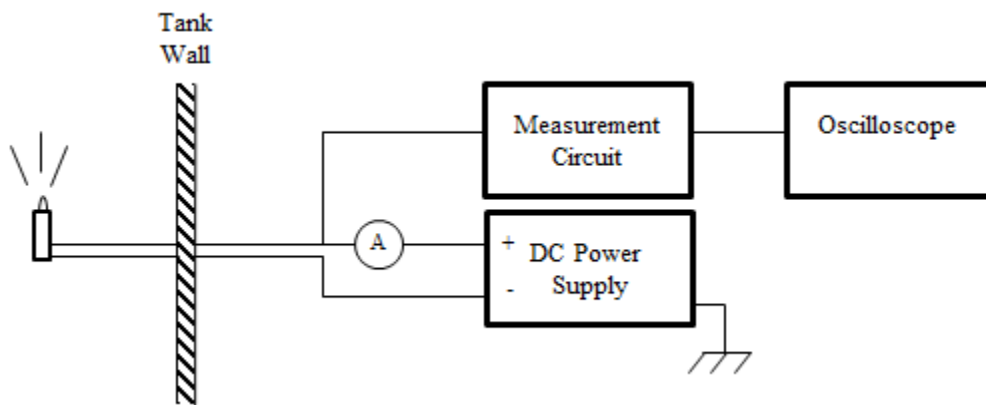


Figure 29: Emissive probe setup

The DC power supply sourced the current necessary to heat the emissive probe to emission temperatures. The current to the filament was monitored by an ammeter in series with the filament and power supply. The emissive probe floating voltage was measured using a custom, high impedance circuit. The output of the measurement circuit was fed to an oscilloscope, where the emissive probe voltage could be monitored in real time. Emissive probe voltages were recorded from the oscilloscope using LabVIEW and computer through a General Purpose Interface Bus (GPIB).

The emissive probe measurement circuit was based on a previous design and circuit by Goebel [109] and consists of an IRF540 MOSFET (metal-oxide semiconductor field effect transistor) in a source-follower configuration. The gate of the MOSFET is forward biased with 1.5V by an AA battery, allowing measurements close to 0 V. The source of the MOSFET is connected to a 10:1 voltage divider to reduce the measured voltage. To avoid improper loading of the MOSFET and maintain a low impedance to the DAQ, a unity gain buffer is implemented between the voltage divider and DAQ. In the event of a short, the measurement circuit is protected on either end by 1 kΩ resistors. The emissive probe measurement circuit schematic is shown in Figure 30.

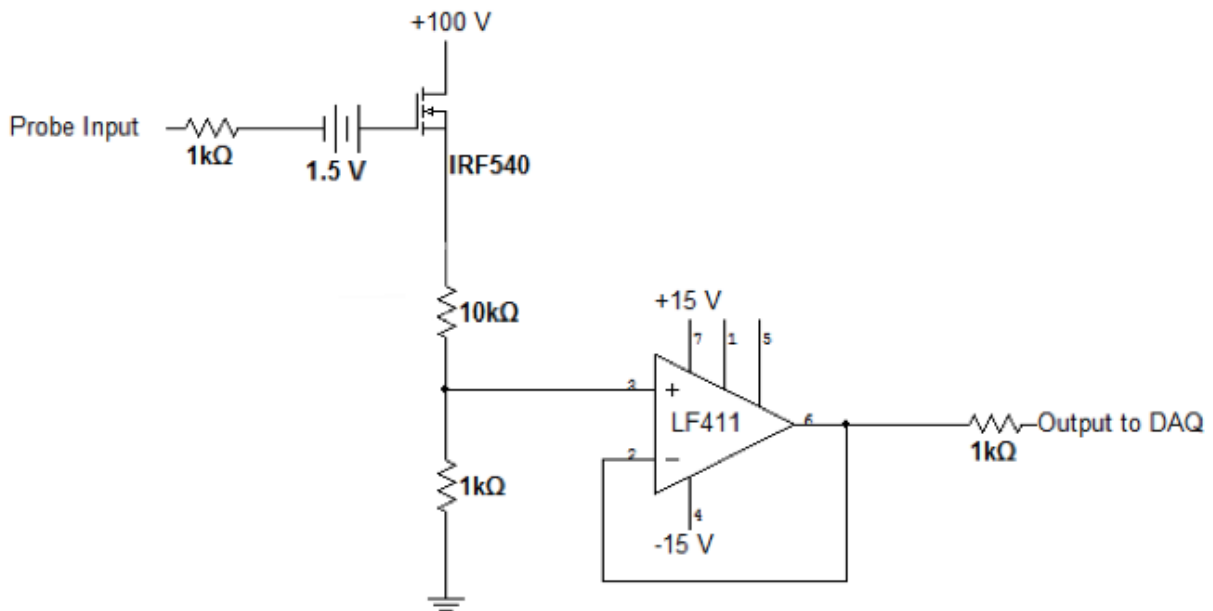


Figure 30: Emissive probe measurement circuit schematic [110]

The emissive probe was located approximately 7 mm downstream of the keeper exit plane, along the center axis of the cathode. The top of the emissive probe loop was 1-2 mm below the cathode centerline, to allow the moving Langmuir probe to traverse the near-plume region without damaging the emissive probe.

4.2 Langmuir Probe

This section describes the physical construction of the single Langmuir probe (SLP) and associated circuitry. The SLP used for this experiment consisted of a 0.076 mm x 2 mm (0.003 in x 0.079 in) high purity tungsten wire (probe tip), supported and insulated by 0.70 mm OD x 0.50 mm ID x 7.0 mm L (0.028 in OD x 0.020 in ID x 0.276 in L) borosilicate tube (probe holder). The borosilicate tube was supported and insulated by a 6.35 mm OD x 4.78 mm ID (0.25 in OD x 0.188 in ID) alumina tube (approximately 300 mm in length) fixed at one end in a Swagelok™ tee. The end of the borosilicate tube was sealed with 904 Zirconia paste. The interface between the borosilicate tube and the alumina was also sealed with 904 Zirconia paste to hold the borosilicate tube in place and prevent plasma penetration. To securely seat the alumina tubing in the reducing union without the risk of fracture, Teflon ferrules were used in place of stainless steel (this method also does not require any modifications to the Swagelok union). A scale drawing of the SLP assembly is shown in Figure 31.

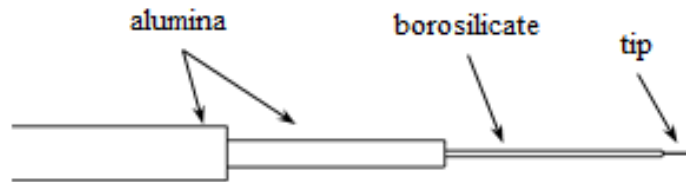


Figure 31: SLP tip schematic

As discussed in Section 2.4.2 any object immersed in a plasma will perturb the local plasma in some way and develop a sheath, and a Langmuir probe is no exception. Standard Langmuir probe theories, as discussed in Section 3.2 account for the presence a sheath around the probe; however, a general assumption in these theories is that the probe does not “sufficiently disturb” the bulk plasma. To ensure the probe does not perturb the bulk, the probe tip and probe holder must be sufficiently small. A simple guide for probe tip and holder sizing was determined by Godyak and is defined by the following inequality [111]:

$$a \ln \left[\frac{\pi l}{4a} \right], b, \lambda_D \ll \lambda_e \quad (4-1)$$

Where a is the probe tip radius, l is the probe tip length, b is the probe holder radius (borosilicate tube), λ_D is the electron Debye radius and λ_e is the electron mean free path. Satisfying this criterion will ensure the plasma is not sufficiently disturbed by the probe and the sheath is collisionless.

The probe position relative to the cathode was controlled by two, stacked PI miCos VT-80 linear translation stages, providing two-axis control in the horizontal plane (300 mm range in x-direction and 200 mm range in y-direction). Each translation stage was powered by a “2phase-042” stepper motor with an SMC Pullox motor-control module, and equipped with full-step encoders and integrated limit switches. The stepper motors offered a maximum translation speed of 13mm/sec and a knowledge resolution of 5 microns. Communication with the motor occurs through two RS 232 DB-9 cables providing independent power and data, with a PI miCos supplied LabVIEW virtual instrument (VI) as the control interface. The VI allowed independent control of each stage, with the capability of specifying absolute or relative probe displacement. The translation stages were mounted one on top of the other, as shown in Figure 32. A custom aluminum fixture, which allowed fine vertical and pitching adjustments, supported the probe on the upper translation stage. The positioning system was mounted on to an adjustable scissor lift for precise vertical adjustments, which was securely fastened to the vacuum chamber wall and allowed up to two inches of vertical adjustment. Prior to each test, the acceptable probe translation area was mapped to ensure unobstructed probe translations. The positioning system and probe assembly is shown in Figure 32 below. For scale, the aluminum mounting plate is 18 inches by 15.5 inches.

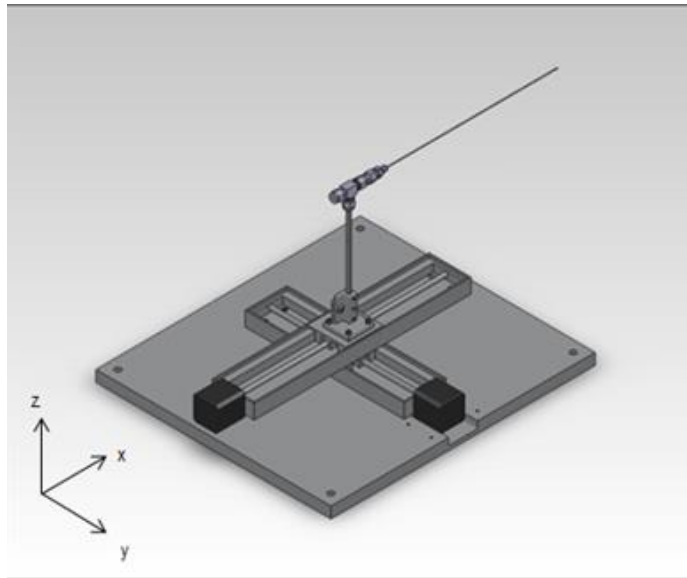


Figure 32: Single Langmuir probe and stage linear translation stages

To connect the SLP to the measurement and data acquisition equipment, 20 AWG magnet wire (with enamel insulation removed at each end) was inserted into the alumina tubing, through to the Swagelok tee and soldered to the tungsten wire. The other end of the magnet wire (outside of the reducing union) was soldered to a BNC connector and connected to a shielded coaxial cable, which was connected to the instrumentation outside of the vacuum chamber via a BNC feedthrough. The transition from magnet wire to BNC connector was housed in a custom grounded electrical shield, which connected to the Swagelok tee and accepted a threaded BNC connector at the other end. A schematic of the Langmuir probe setup is shown in Figure 33.

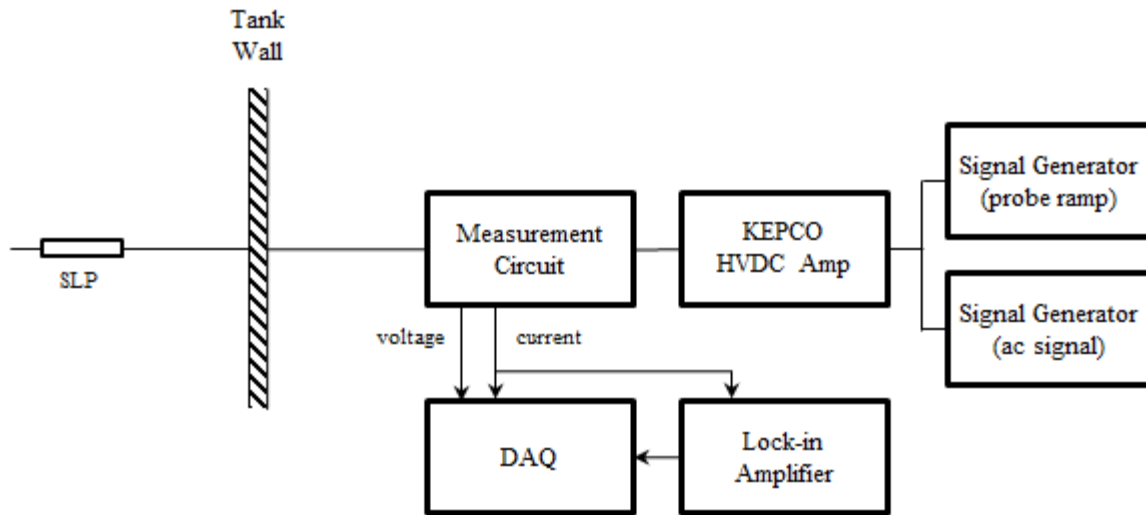


Figure 33: Langmuir probe setup

Measurement of the probe bias voltage and collected current was obtained using a measurement circuit based on a design used for hollow cathode plume studies at the Jet Propulsion Laboratory [109]. A schematic of the SLP circuit is shown in Figure 34 below. The circuit measures the probe voltage (V_{out}) and voltage proportional to the probe current (I_{out}) using a shunt resistor. The primary modification to the circuit for this work was the addition of a low pass filter on the probe current signal. The custom low pass filter is a 4-pole Butterworth filter based on a Sallen-Key topology with a 3 kHz cutoff frequency.

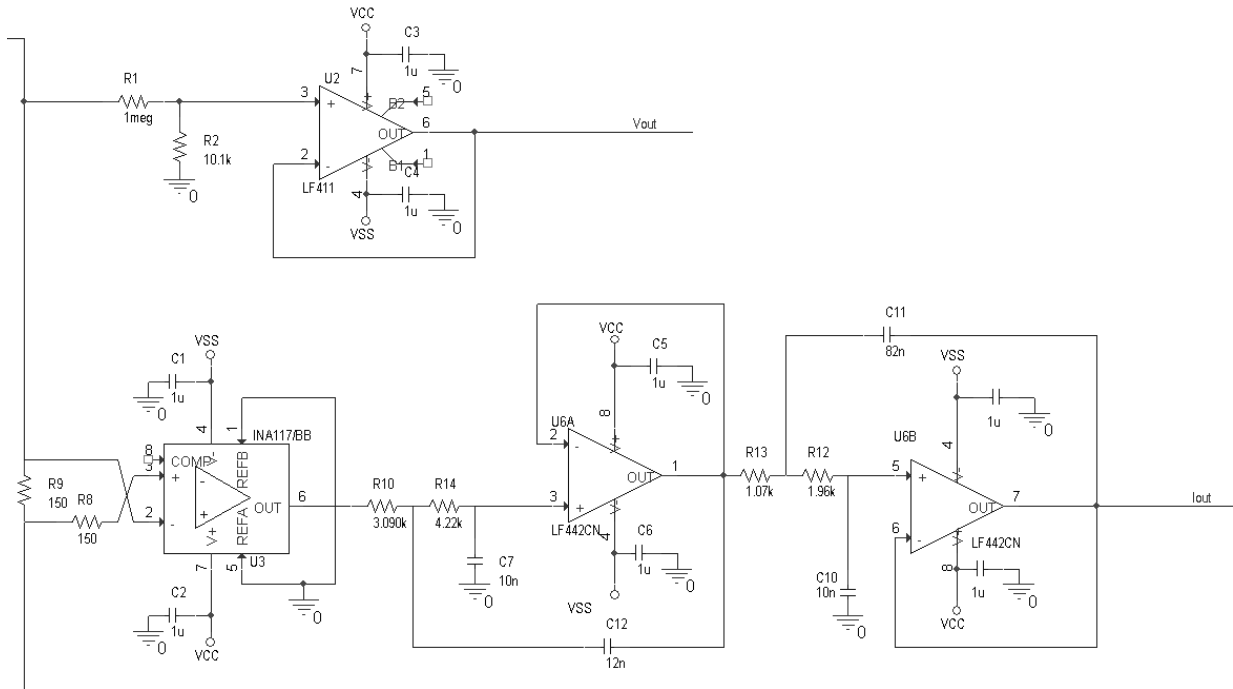


Figure 34: Langmuir probe measurement circuit schematic.

The measurement circuit allowed probe voltage and current to be measured and collected by the DAQ and LabVIEW. For each set of tests performed, the signal from the measurement circuit was calibrated using a constant DC voltage applied to a known resistance simulating the plasma load. The result of each calibration test was a curve of actual current and voltage versus a corresponding sense voltage produced by the measurement circuit. These calibration curves were then used to generate the correct voltage and current measurements displayed in LabVIEW in real-time during testing and used in post-processing.

The probe bias waveform was provided by an Agilent 33229A waveform generator and amplified by a KEPCO BOP-100M high voltage bipolar power amplifier, then sent to the probe tip through the custom measurement circuit. The gain of the bipolar amplifier is fixed at 10:1, thus adjusting the probe bias waveform amplitude at the signal generator changed the magnitude of the probe sweep. For this test series, a ramp (saw tooth) waveform at 10Hz was used. The sweep frequency (10 Hz) was chosen to ensure that it was below any time constant effects of the measurement circuit, but above any transient time constant of the plasma. A second signal (± 1 V, 1 kHz sine wave) was superimposed over the probe

bias waveform using a Beckman FG2A signal generator. This signal was superimposed using a simple summing circuit (based on the INA105 difference amplifier) before the bipolar amplifier.

The amplitude (corresponding to the last bracketed term in Equation (3-31)) of the second harmonic term is extracted from the probe current signal using a Stanford Research Systems SR810 DSP lock-in amplifier. The experimental data were collected for analysis using a LabVIEW virtual instrument (VI) and National Instruments USB-6341 X-Series DAQ capable of collecting 500 kS/sec (aggregate). A detailed user's guide for the collection of I-V curve second derivative data from the lock-in amplifier is provided in Appendix B.

A MATLAB code was used to import and parse the data to obtain corresponding voltage, current and second derivative data for each probe sweep. For the tests reported here, the probe was stationary during each sweep so the data was manually paired with the corresponding probe location.

4.3 Hexaboride Cathode Experimental Setup

The hexaboride cathodes were tested in the T1 test facility at Busek Co. Inc. The T1 test facility is a stainless steel cylindrical tank with a 6-ft diameter. High vacuum pumping is provided by a 16" diffusion pump and single stage cryopump, which is shrouded by liquid nitrogen (LN2) panels. The T1 facility is has a base pressure in the low 10^{-6} torr range and a pumping speed of approximately 80,000 l/s on xenon. The facility is more than capable of maintaining a space environment for hollow cathode testing.

The hexaboride cathode used in this experiment was designed and built by Busek Co. Inc. (Natick, MA). The cathode thermionic emitters and cathode orifices could be changed by disassembling the cathode tube and heater assembly. The cathode tube was made entirely of graphite to eliminate boron diffusion from the hexaboride emitters to hot refractory metals (traditional cathode tube materials). A custom graphite-PBN heater brought the hexaboride emitters to emission temperatures. The downstream end of the keeper was made from graphite because of its low thermal conductivity, low sputter yield and low reactivity. The upstream end was made of 316 stainless steel. The cathode discharged to a cylindrical stainless steel

anode, located approximately 50 mm downstream of the keeper exit plane. The cylindrical anode provides an axisymmetric potential and allows the Langmuir probe access to the cathode centerline. The hexaboride cathode setup is shown in Figure 36 and properties listed in Table 9.

Table 9: Cathode properties and range of operating conditions

Propellant	Flowrate (SCCM)	Discharge Current (A)	Emitter Material
xenon	1-8	1-5	LaB ₆ and CeB ₆

Although hexaborides are much less susceptible to poisoning and contamination than traditional BaO thermionic emitters, the cathode was conditioned after each exposure to air. The cathode conditioning procedure consisted of incrementally increasing cathode heater power, holding each power level for approximately one hour, until the cathode reached emission temperatures. The conditioning procedure drives water and other contaminants from the emitter surface before ignition. The conditioning procedure was used after each exposure to atmosphere to prevent contamination, which would result in an increase in the emitter work function and possibly changes in the cathode performance from test to test. Once the cathode reached emission temperatures through the conditioning procedure, the keeper electrode was energized and internal discharge initiated. Once a stable plasma was established, the cathode heater was turned off and anode energized. The anode power supply was set to current-limited mode at the desired discharge current.

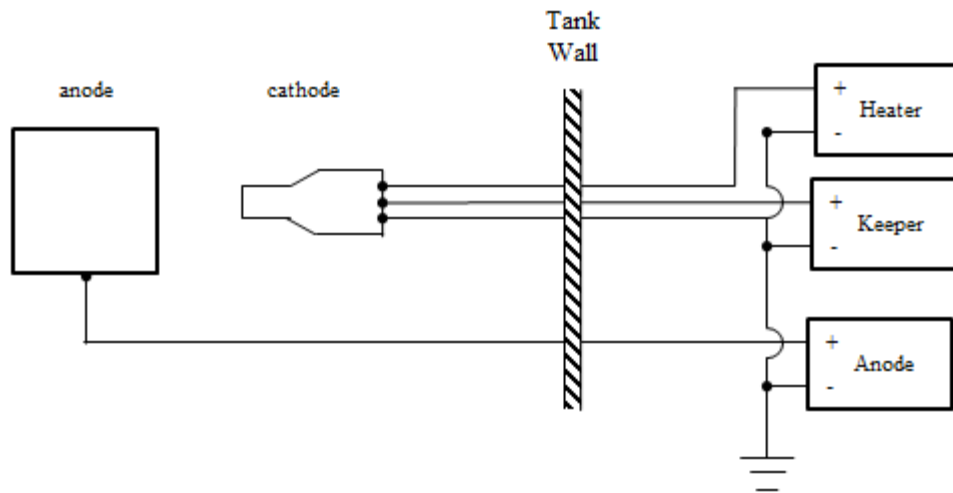


Figure 35: Hexaboride cathode electrical diagram

High purity, propulsion grade xenon (99.999+%) xenon was supplied to the cathode using a 0-20 SCCM MKS mass flow controller (accuracy = $\pm 1.0\%$ of F.S.). Propellant lines consisted of stainless steel tubing and fittings. The entire propellant feed system was thoroughly leak-checked using helium to prevent oxygen contamination of the propellant.

The emissive probe position was fixed on the cathode centerline, approximately 7 mm downstream of the keeper exit plane. To prevent the moving Langmuir probe from impacting the emissive probe, the emissive probe was positioned slightly below the cathode centerline in the vertical direction. This allowed the Langmuir probe to pass over the emissive probe when not in use and to access points closer the keeper exit plane along the cathode centerline.

The Langmuir probe was mounted on two stacked linear translation stages which allowed movement in the horizontal plane in the cathode plume. Prior to closing the vacuum facility the Langmuir probe travel range was mapped to avoid the anode, confirm the emissive probe position would not interfere with SLP motion and align the probe tip with the cathode centerline and cathode exit plane.

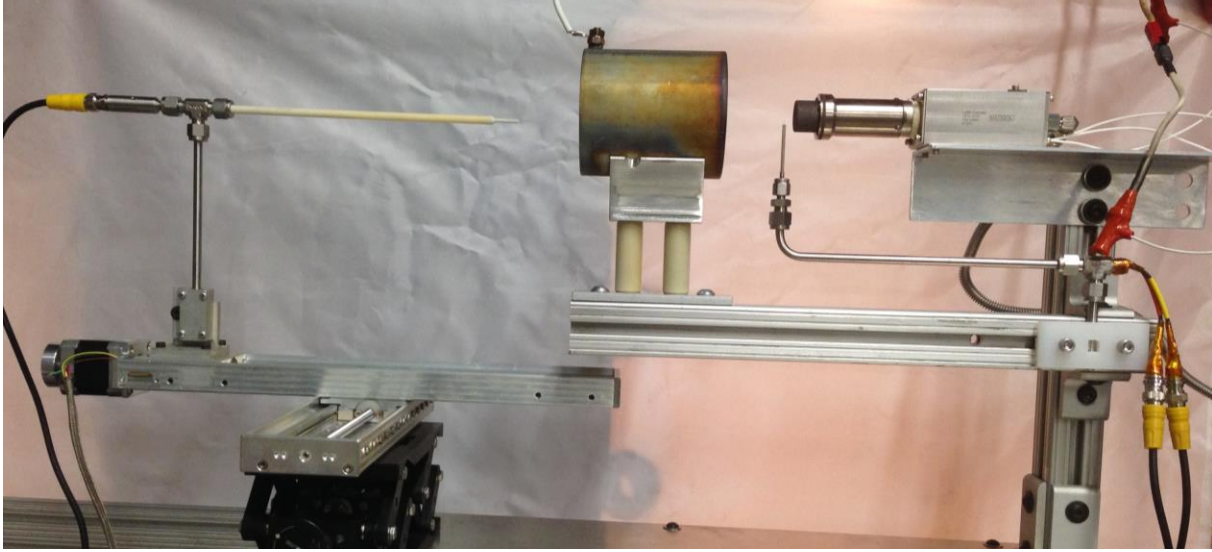


Figure 36: Hexaboride cathode setup showing SLP, translation stages, anode, emissive probe and cathode

4.4 BaO Cathode Experimental Setups

Two BaO hollow cathodes were tested with iodine and xenon propellants; one at WPI and the other at Busek Co. Inc. The testing conducted at WPI consisted exclusively of testing BaO emitter compatibility with iodine propellant. The testing at Busek Co. Inc. also testing the ability of a BaO cathode to operate on iodine propellant but the facility was also equipped with diagnostic tools. This section described both BaO cathodes used for iodine compatibility and performance testing.

4.4.1 BaO Cathode – Configuration 1

BaO cathode compatibility tests with iodine were conducted in Worcester Polytechnic Institute's (WPI) Fluid and Plasma Dynamics Laboratory. The vacuum chamber used in this study consisted of an 18" by 36" stainless steel bell jar shown in Figure 37. The chamber has base pressure of approximately 10^{-6} Torr, achieved by a 6" Clark diffusion pump backed by a Welch rotary mechanical pump. The chamber pressure is measured by a Varian XGS-600 Gauge Controller using a Type 0531 Vacuum Gauge and MBA-200 Bayard-Alpert Ion Gauge.



Figure 37: Vacuum facility used for BaO cathode tests with iodine propellant.

Cathode

The cathode used in this experiment was custom designed and built by Busek, Co., Inc. Some deviations from a typical cathode design were necessitated by the need to easily remove and replace the low work function insert. A conventional BaO:CaO:Al₂O₃ cathode insert was procured by Busek from Heat Wave Labs Inc. (Watsonville, CA) and sectioned into smaller segments, or samples, for use in this study under a variety of operating conditions. The cathode is shown installed in the bell jar in Figure 38. For testing, a planar anode was installed below (downstream of) the keeper orifice.

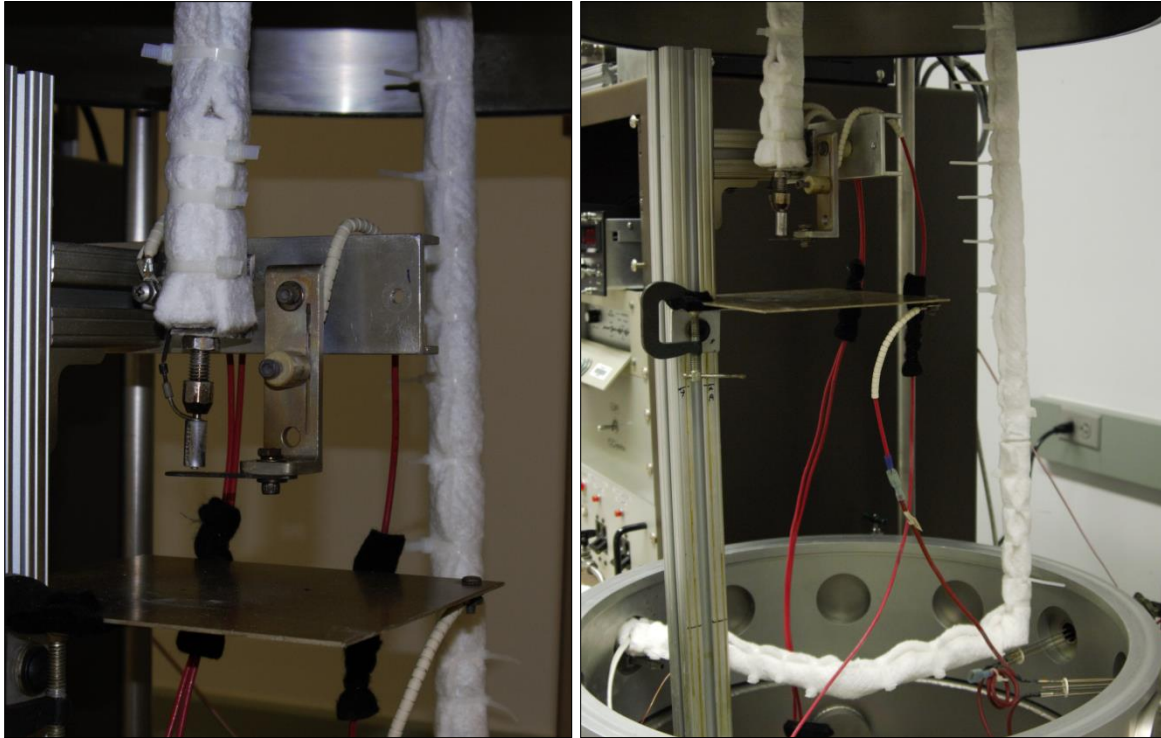


Figure 38: Laboratory cathode and rectangular anode (left) used in iodine cathode tests and feed lines to cathode inside vacuum chamber comprising temperature controlled zone 3 (right).

The cathode/anode system was powered by three DC power supplies, which provided power to the keeper electrode, heater coil, and anode, as shown in Figure 35. All power supplies shared a common neutral, or cathode common, which was tied to facility ground. For this experiment, the resistive heater coil was powered by a TDK-Lambda 36V/25A power supply and the keeper electrode by a Sorenson XFR 600-2 power supply. The anode was of rectangular geometry and biased to approximately +40 V by a Sorenson DCR 150 power supply. The power supplies were manually controlled and operating conditions were manually recorded.

Propellant Feed System

Xenon was supplied through a custom manifold, regulated by a manually operated Swagelok SS-4VCR4 needle valve, and monitored by a 20 SCCM MKS 179A mass flow meter (MFM) and MKS 246 power supply/readout. The MFM was calibrated with xenon using a bubble volumeter. Xenon flow rate was monitored by a data acquisition system using LabView.

Iodine (I_2) vapor was sublimed from high purity crystals (Alfa Aesar, 99.9985% purity, resublimed crystals) in a thermally controlled reservoir (pot) located outside of the vacuum chamber as shown in Figure 39. The iodine delivery system is shown schematically in Figure 40. To prevent condensation of iodine within the feed lines, the lines were divided into two temperature-controlled zones (the pot comprising an additional zone) as shown in Figure 40. The stainless steel lines were wrapped in Omega FGS051-020-LSE heater tape and all heated lines were wrapped in thermal insulation (over the heater tape). The pot heat was provided by an Omega CIR-1023/120V heater cartridge (also wrapped in thermal insulation). The feed line temperatures (zones 2 and 3) were controlled using Omega CN424 controllers to a set point above the pot temperature with thermocouples placed at what likely would be cold spots along the lines. The feed line pressure, P_L , was measured by an Omega PX-409 pressure transducer (0-5 psia range, with temperature compensation to 85°C) and used to correlate mass flow rate with supply pressure. (During testing, the pressure transducer was permanently damaged; therefore, the pressure transducer was omitted from Figure 39.)

To initiate iodine flow, the iodine reservoir was heated to the desired temperature, T_{pot} , by the zone 1 temperature control circuit. The pot temperature is selected based on the vapor pressure curve for pure iodine and a flow calibration measurement. The iodine feed line, from the reservoir to the cathode, was heated by zone 2 and 3 temperature control circuits to $T_{pot} + \Delta T$ where ΔT is typically a minimum of 10°C, in order to prevent the iodine from depositing downstream of the pot. The mass flow rate was calculated by weighing the reservoir before and after each test, then dividing the difference by the test duration.

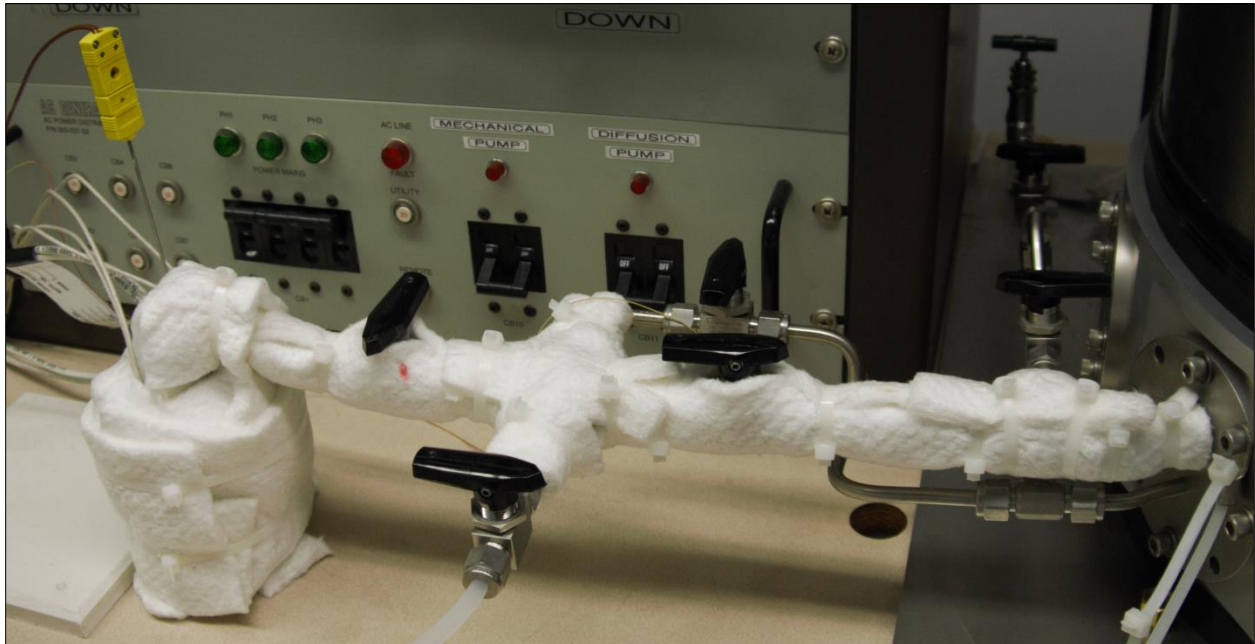


Figure 39: Portion of iodine delivery system located outside vacuum chamber. Iodine reservoir (pot) and stainless (wrapped in thermal insulation) lines comprise temperature control zones 1 and 2, respectively.

In order to correlate iodine mass flow rate with line pressure and pot temperature, a calibration test was performed. For these calibration measurements, the cathode was replaced with a Swagelok plug in which a through hole (0.020 in) was machined to create an orifice of the same diameter as the cathode orifice. The plug was used to provide an approximation of the hydraulic resistance provided by the cathode without contaminating or poisoning it before attempting to operate it with iodine for the first time.

For the Calibration Test, the (filled) pot was weighed and integrated into the iodine feed system. The iodine reservoir was heated to 55°C (T_{pot}) and maintained within $\pm 0.5^\circ\text{C}$ for the duration of the test. The lines downstream of the reservoir to the cathode were heated to 120°C ($T_{\text{pot}} + \Delta T$) and also maintained to within $\pm 0.5^\circ\text{C}$ for the duration of the test. During the test, temperature and pressure data were recorded every few minutes. After heating the pot for approximately 45 minutes, the pot was isolated (valve V1), allowed to cool, removed and weighed. From the calibration, the flow rate was found to be approximately 0.9 ± 0.01 mg/s at a temperature of 55° C and line pressure of 0.05 – 0.06 psia. The target

flow rate for this cathode was 0.05 to 0.1 mg/s, so for Calibration 2, the pot temperature (zone 1) was reduced to 30°C while keeping the temperature of zones 2 and 3 the same.

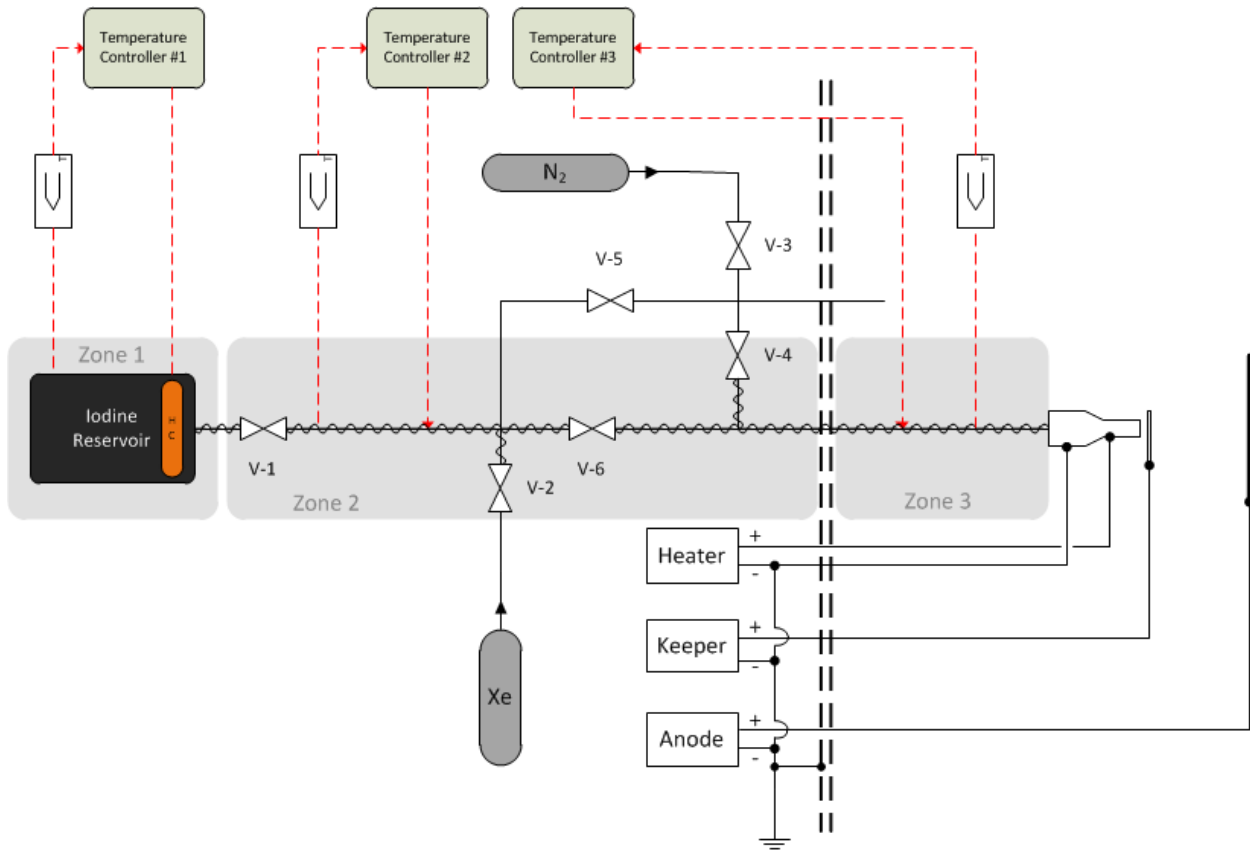


Figure 40: Schematic showing iodine, xenon and nitrogen (purge) supplies, and electrical connections used in testing.

4.4.2 BaO Cathode – Configuration 2

Testing of the second BaO cathode on iodine and xenon was conducted in the T1 vacuum facility at Busek Co. Inc. as described in Section 4.3.

The hollow cathode used in this experiment was a laboratory hollow cathode developed by Busek Co. Inc. and similar in design to the BaO hollow cathode used in the initial iodine compatibility testing described in Section 4.4.1. Figure 41 shows the laboratory cathode with annotations.

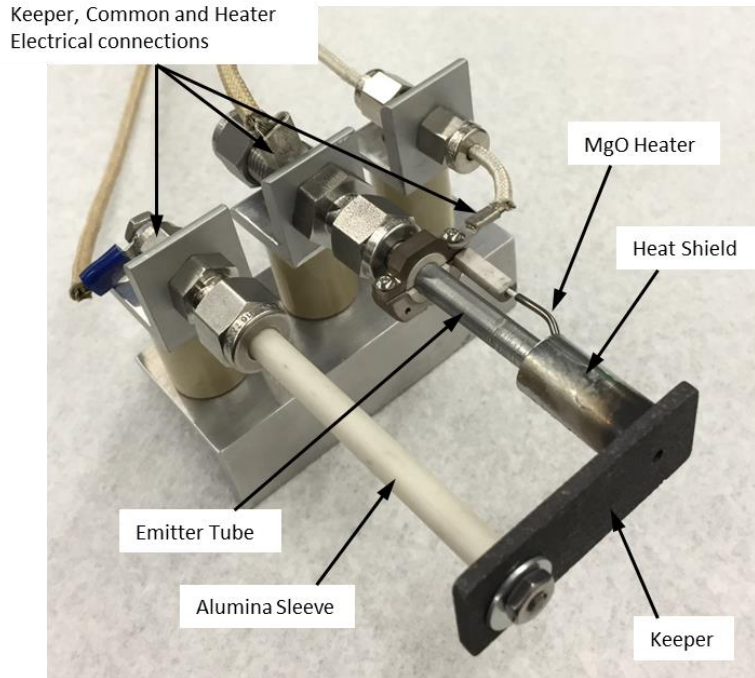


Figure 41: Laboratory BaO hollow cathode used for xenon and iodine comparison testing

Xenon and iodine propellants were independently supplied to the cathode and required entire separate feed systems. The xenon propellant was supplied to the cathode using an MKS mass flow controller as described in Section 4.3. The iodine feed system used a simplified version of the iodine feed system as described in the previous section. The entire iodine feed system was inside the vacuum tank to eliminate the possibility of oxygen leaking into the feed system. A schematic of the feed system is shown in Figure 42.

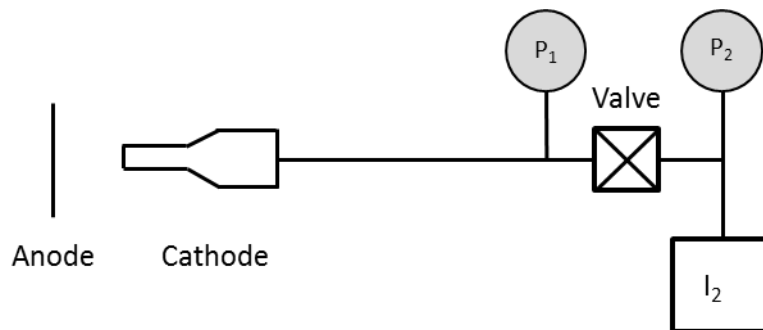


Figure 42: Schematic of the iodine feed system and cathode.

The iodine was supplied to the cathode via heater reservoir. The cathode could be isolated from the iodine reservoir via solenoid valve located just downstream of the iodine reservoir. Pressure sensors on either side of the solenoid valve measure the feedline and reservoir pressures. The feed lines and reservoir were heated by two separate heater circuits which allowed for the feed line temperature to exceed the reservoir temperature to prevent iodine condensation. The reservoir temperature was adjusted and pressure monitored to crudely control the iodine flow rate. The iodine feed system and BaO cathode is shown below in Figure 43. The cathode electric connections are identical to the connections described in the previous two sections.

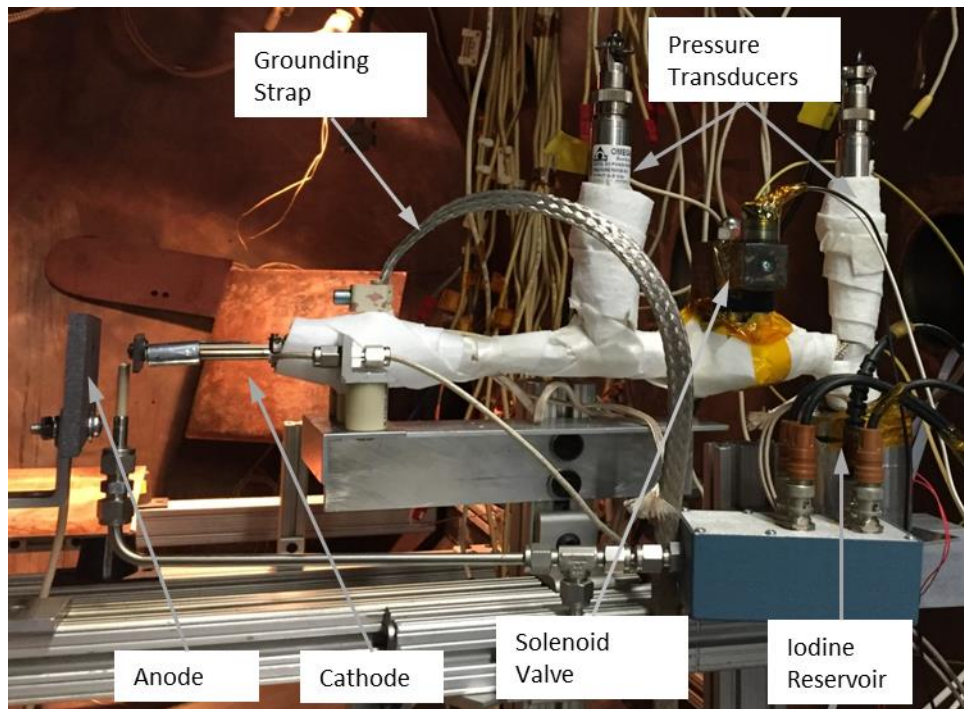


Figure 43: BaO hollow cathode with iodine feed system.

Chapter 5 Results

This chapter presents results for three separate cathode studies, one with hexaboride and two with BaO emitters. For the hexaboride emitters, Study 1, electrostatic probe measurements are presented to determine operating conditions (current and flow rate) that lead to spot and plume mode operation and to characterize the electron population in the near-plume region during spot mode operation. For the first BaO cathode, Study 2, cathode operation was characterized using both xenon and iodine propellants while also investigating the material interaction between the BaO insert and iodine. For the second BaO cathode, Study 3, cathode operation as well as the near-keeper plume plasma was investigated using both xenon and iodine propellants. Table 10 summarizes the cathode used, emitter type and discharge power for each study and will be referenced throughout Chapter 5. Specific tests will be referenced using the following convention; Study:Case:Trial. For example, “Test 2:2:1” corresponds to Study 2, Case 2 and Trial 1.

Table 10: Summary table for all cathode testing.

Study	Case	Trial	Emitter	Insert #	Orifice Diameter	Nominal Diameter	Propellant	Keeper Current	Anode Current
1	1	1	LaB ₆	N/A	0.020	0.250	Xenon	1.0	2.0
		1			0.020				
	2	2	CeB ₆		0.035				
		3			0.040				
2	1	1	BaO	1	0.020	0.125	Xe & I ₂	0.25	3.1
		2		Xe					
		3		Xe & I ₂					
		4		Xe & I ₂					
3	1	1	BaO	N/A	0.040	0.250	Xenon	0.25	3.1
							2		

5.1 Hexaboride Cathode Study

The hexaboride cathode study determined the nominal cathode operating conditions with xenon by identifying the transition from spot mode (favorable operating condition) to plume mode operation. A transition to plume mode is typically identified by a relative increase in plasma potential fluctuations as

flow rate is reduced for a given current, or as current is increased for a given flow rate. This study focused on changes in flow rate at a fixed discharge current (anode current) of 2 A (keeper current 1 A). The cathode flow rate was decreased from 8 SCCM to 1 SCCM. Operation near or below 1 SCCM typically resulted in “runaway” anode voltage. During normal operation, the anode power supply is in current control mode; therefore, in order to maintain a particular current setting the voltage must adjust to allow the power supply to source the desired current. When the cathode is operating in plume mode it is difficult for the cathode to source the desired current. As a result, the anode power supply will increase the potential of the anode in an attempt to maintain the current set point. The voltage is considered in a “runaway” condition when the anode power supply voltage continues to climb until the voltage limit is reached.

5.1.1 LaB₆ Emitter

As described in Section 2.2, LaB₆ and CeB₆ are very similar emitter materials, with CeB₆ having a slight theoretical advantage over LaB₆; however, LaB₆ has been used extensively in Russian hollow cathodes [112] and is being used with increasing frequency in laboratory cathodes supporting development of future, high-power EP missions [113]. The approximate operating conditions, for the cathode used in this study (described in Section 4.3), over the range of flow rates are listed in Table 11. In this Study, both the keeper and anode currents are maintained by their respective power supplies in current control mode, such that the voltage is automatically adjusted by the power supply.

Table 11: Range of LaB₆ cathode operating conditions

Q (SCCM)	V_K (V)	I_K (A)	V_A (V)	I_A (A)
1-8	13-15	1.0	30-90	2.0

Figure 44 shows the anode voltage required to maintain 2 A of current to the anode over the range of flow rates with both the keeper on (1 A) and off. As discussed in Section 4.3, the uncertainty in flow rate is +/- 0.2 SCCM while the uncertainty in the measured voltage is +/- 50 mV (this is the same for all xenon flow

rates and keeper and anode potentials reported). In either case, the anode voltage continues to rise as the cathode flow rate is reduced. For low flow rates (< 3 SCCM) the anode voltage is slightly higher with the keeper turned off. This suggests that at lower flow rates it may be more difficult (requiring higher potential) to couple to the cathode. Often the keeper is turned off during thruster operation to conserve power, but keeping it on may lead to a more stable plasma and better cathode-thruster coupling.

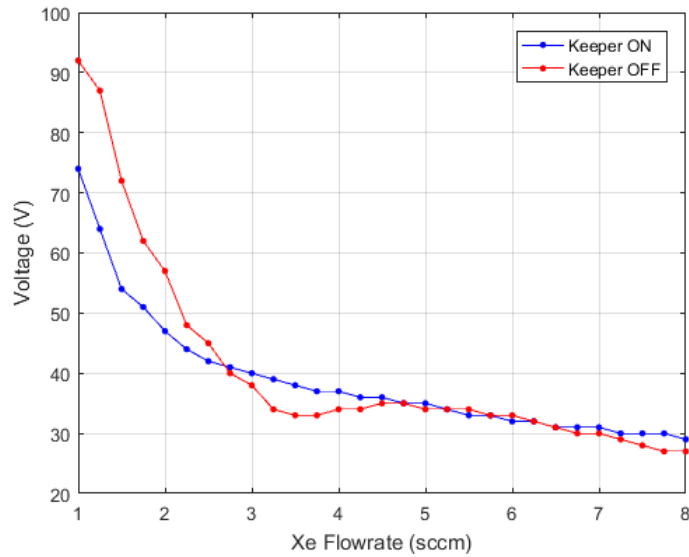


Figure 44: Anode voltage for the LaB₆ cathode

Plume mode vs. Spot mode

As discussed in Section 2.2, operation in plume mode is believed to be linked to the production of high energy ions which can lead to increased sputtering, resulting in higher-than-expected keeper and orifice erosion rates. The plasma potential will have some level of oscillatory behavior, even for a relatively steady discharge plasma, but the magnitude of fluctuations can change based on the plasma properties and discharge conditions. Operation in plume mode is characterized by high-frequency, large (relative to the mean) amplitude oscillations of the plasma potential. The peak plasma potential could vary significantly, and may not accurately represent the most probable or average amplitude of plasma potential oscillation; therefore, for consistency, the root mean square (RMS) of the plasma potential signal was used to

quantify the magnitude of the fluctuations in the plasma potential. The plasma potential as a function of time, as measured by a floating emissive probe for Test 1:1:1, is shown in Figure 45, for a flow rate that was determined to be within the regime of spot mode operation (6 SCCM). The spot mode operating range corresponds to the flow rate range corresponding to the minimum normalized RMS potential. For this configuration, the mean plasma potential, over 4 msec, was 36.9 V and the RMS was 0.96 V. The corresponding power spectral density estimate (in decibels referenced to 1 V²) in Figure 46 shows few frequencies of interest except for a slight peak at approximately 120 kHz, which is likely a result of normal plasma discharge oscillations [19]. Although the peak at 120 kHz shows a strong frequency signature, the magnitude of the peak is small and will likely not lead to the production of ions with energies significantly above the plasma potential. Throughout the entire results section (Chapter 5), the uncertainty in the reported plasma potential is $\pm 10\%$ unless otherwise specified.

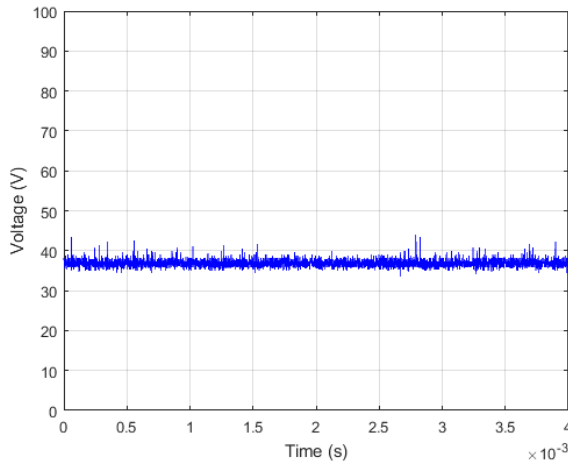


Figure 45: Plasma potential vs time (6 SCCM).
 $\phi_{mean} = 36.9 \text{ V}$, $\phi_{rms} = 0.96 \text{ V}$

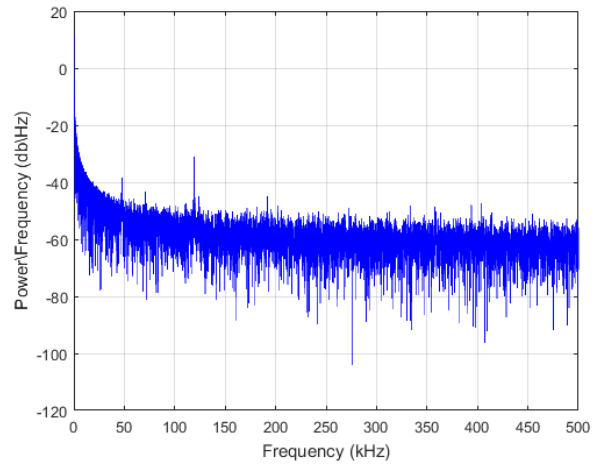


Figure 46: Power Spectral Density Estimate for plasma potential (6 SCCM)

For the same discharge power, the plasma potential time history changes considerably when the cathode flow rate is reduced to 1 SCCM corresponding to Test 1:1:1. For this case, Figure 47 shows the plasma potential, and Figure 48 shows the PSD estimate. The mean plasma potential for this case was 46.2 V and RMS 8.4 V, which are considerably higher than the corresponding values for the 6 SCCM case. The

frequency spectrum shows a peak around 50 kHz, which was not present in the 6 SCCM case. The plasma potential oscillations in Figure 47 are indicative of ionization instabilities.

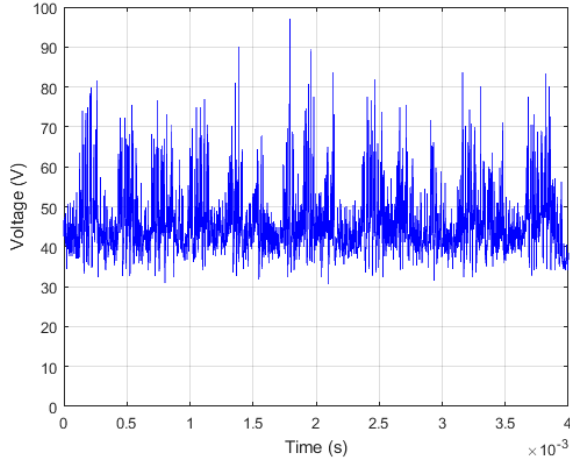


Figure 47: Plasma potential vs time (1 SCCM).
 $\phi_{mean} = 46.2 \text{ V}$, $\phi_{rms} = 8.4 \text{ V}$

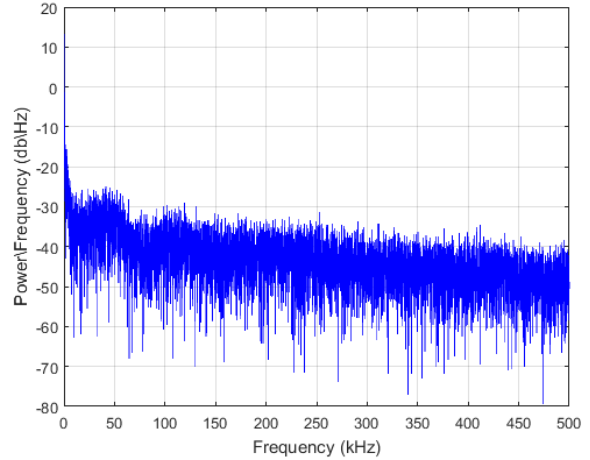


Figure 48: Power Spectral Density Estimate for plasma potential (1 SCCM)

As the cathode flow rate is increased, at fixed discharge current, the plasma potential time history evolves and the peak in the frequency spectrum becomes more pronounced. For a cathode flow rate of 2 SCCM, at the nominal discharge power, the plasma potential time history is shown in Figure 49 and PSD in Figure 50. The mean plasma potential for this case was 43.2 V and RMS 6.3 V; both are slightly lower than the corresponding values at the 1 SCCM flow rate. The frequency of interest in the PSD is approximately 30 kHz for this case.

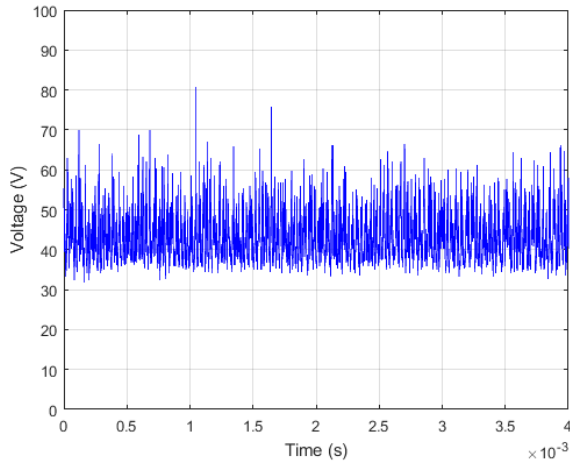


Figure 49: Plasma potential vs time (2 SCCM).
 $\phi_{mean} = 43.2 V, \phi_{rms} = 6.3 V$

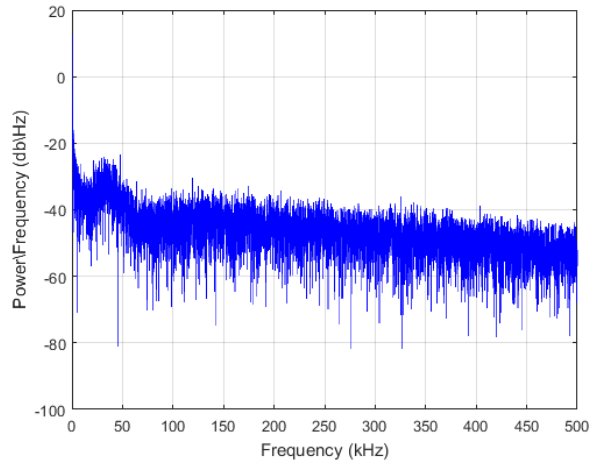


Figure 50: Power Spectral Density Estimate for plasma potential (2 SCCM)

Increasing the flow rate further, to 3 SCCM shows the trend continuing, where the mean and RMS plasma potential decrease, the peak in the frequency spectrum becomes sharper still. Figure 51 shows the plasma potential time history and Figure 52 shows the PSD estimate for a 3 SCCM cathode flow rate. The mean plasma potential was 40.2 V and RMS 5.26 V. The frequency of interest in the PSD is still ~30 kHz.

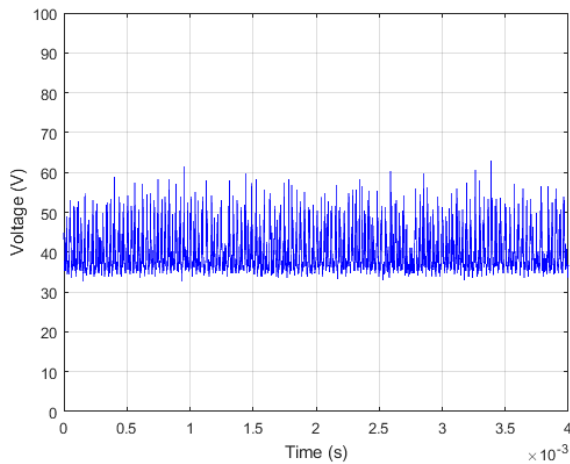


Figure 51: Plasma potential vs time (3 SCCM).
 $\phi_{mean} = 40.2 V, \phi_{rms} = 5.26 V$

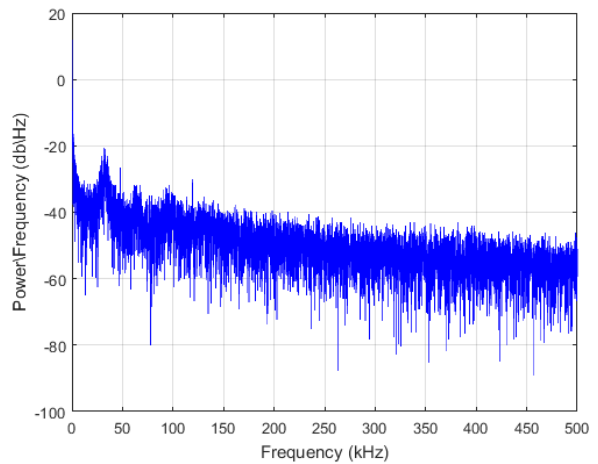


Figure 52: Power Spectral Density Estimate for plasma potential (3 SCCM)

Once the flow rate has increased to 4 SCCM, the 30 kHz peak becomes blunter and begins to widen. By 4.5 SCCM the peak is no longer visible.

To fully characterize the cathode transition from spot mode to plume mode operation, the plasma potential was measured at 0.25-SCCM increments over the range of flow rates at the nominal discharge power. Figure 53 shows the RMS of the plasma potential (uncertainty is negligible, see Section 3.1.2) as measured by an emissive probe in the near keeper region (8 ± 0.5 mm from keeper exit) for two operating conditions (keeper on and off) over a range of flow rates. For the keeper-on condition, the RMS value is slightly higher at low flow rates and lower at higher flow rates compared to the keeper-off condition. For the keeper-off condition, the RMS value does not fall as sharply compared to the keeper-on condition, as flow rate is increased; however, there is a sharp dip around 2.75 SCCM, which cannot be easily explained. One possibility for this dip is that the cathode plume is much more unstable in the keeper-off condition and the cathode is switching between spot and plume mode operation in the transition flow rate regime.

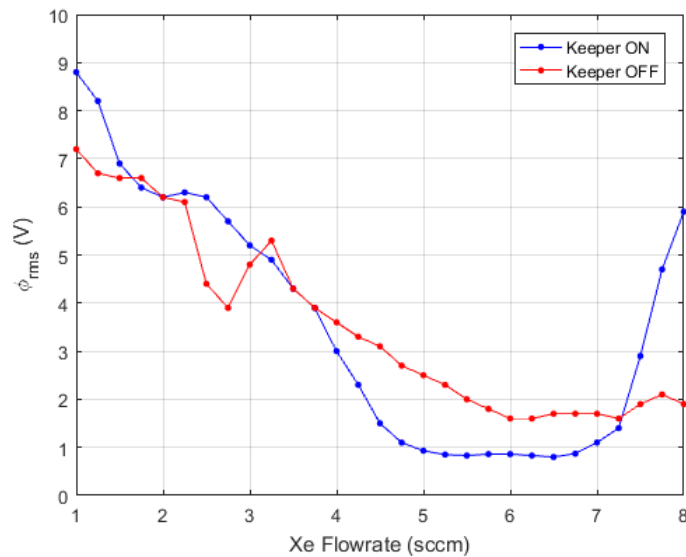


Figure 53: Plasma potential RMS for the LaB₆ cathode

Figure 54 shows the normalized RMS potential in the near keeper region of the discharge as a function of xenon flow rate at the nominal operating power. The normalized RMS potential is defined here as:

$$\frac{\phi_{rms}}{\phi_m} \equiv \frac{RMS\ plasma\ potential}{mean\ plasma\ potential} \quad (5-1)$$

Figure 54 shows the plasma potential level as a function of flow rate for the LaB₆ insert and 0.020” diameter orifice (Test 1:1:1) operating on xenon. Figure 54 reveals spot mode operation lies roughly between 5 and 7 SCCM. The normalized RMS potential level decreases monotonically beginning at approximately 2.5 SCCM until spot mode operation begins at approximately 5 SCCM and terminates at approximately 7 SCCM. This is much higher than the desired 2 SCCM nominal operating point based on 10% of the nominal thruster flow rate.

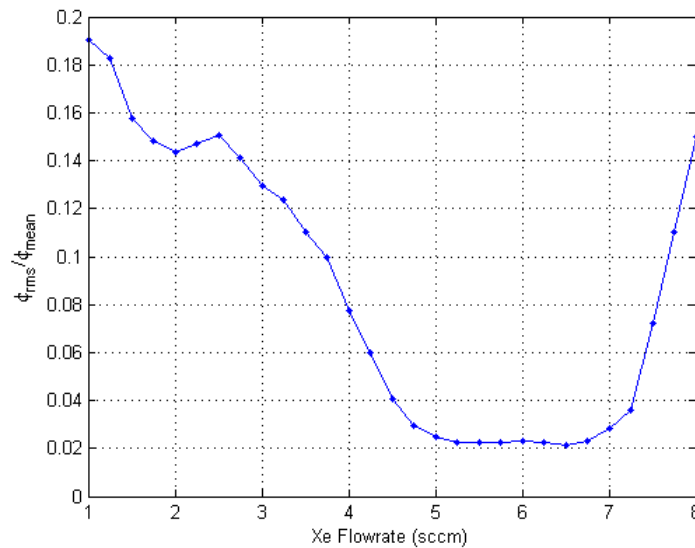


Figure 54: Relative plasma potential fluctuations in the near keeper region of a LaB₆ hollow cathode operating on xenon

Langmuir Probe/EEDF

A single, cylindrical Langmuir probe (Section 4.2) was used to measure the electron energy distribution function (EEDF) just downstream (5 mm) of the keeper exit while operating in spot mode (between 5 and 7 SCCM). Measurement of the EEDF while the cathode is operating outside spot mode leads to significant fluctuations in the plasma potential and results in calculation of an incorrect, lower electron temperature [114]. The Druyvesteyn method was used to calculate the EEDF as described in Section

3.2.3. This method requires the second derivative of the probe current, which is extracted from the probe trace using a lock-in amplifier to measure the second harmonic of a small sinusoidal signal superimposed over the probe voltage as described in Section 3.2.4.

Figure 55 shows a typical Langmuir probe trace, or I-V curve, corresponding to Test 1:1:1. The blue curve is the result of averaging approximately 100 probe voltage sweeps, with each sweep containing approximately 10,000 points. The numerical second derivative was calculated using the I-V curve for the purpose of comparing to the second harmonic method. Numerical differentiation is an inherently noise-amplifying process; therefore, as much signal noise as possible must be extracted from the trace before numerical differentiation can be performed [94]. To this end, using MATLAB's signal processing toolbox, a 9-pole low-pass Butterworth filter was implemented using a cutoff frequency of 800 Hz. This removed any oscillations from the superimposed voltage (1 kHz) over the main probe voltage sweep without distorting the underlying curve. After the noise is reduced using the low-pass filter, the trace is further smoothed using the built-in MATLAB function `smooth`, which uses a moving box-car (400 points) average to "smooth" the trace. The number of points used in any given box of the moving average is two orders of magnitude lower than the total number of points in the trace; as a result, it does not distort the underlying shape of the curve. In Figure 55, the red curve is the result of a numerical filtering and smoothing, which is used for subsequent numerical analysis for comparison with the derivative determined with the harmonic method.

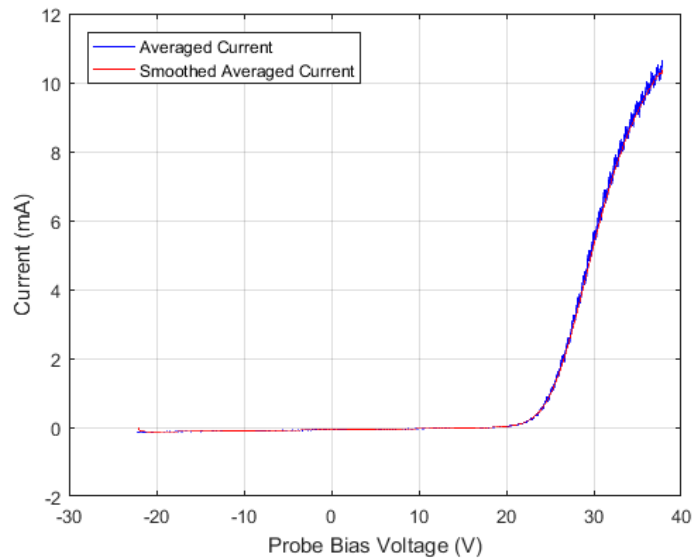


Figure 55: Typical Langmuir probe trace (blue) and trace with smooth function applied (red)

The filtered and smoothed probe trace is then numerically differentiated using the built-in MATLAB function `diff`, which uses a forward finite difference scheme to calculate the slope of two adjacent points. Taking the numerical derivative amplifies any remaining noise not removed through filtering and smoothing. Before the numerical derivative can be taken again to obtain the second derivative, another moving box-car average (400 points) is used to smooth the first derivative. Figure 56 shows the second derivative of the I-V curve determined using numerical differentiation and the second harmonic method. For the numerical second derivative (red curve), the large spikes on either end are from slight kinks in the IV curve caused by the smoothing operations, which are in turn amplified by the numerical differentiation procedure. For the second derivative determined by the harmonic method (blue curve), the large spike near -20 V is the result of the second derivative trying to follow the vertical jump of the underlying ramp signal.

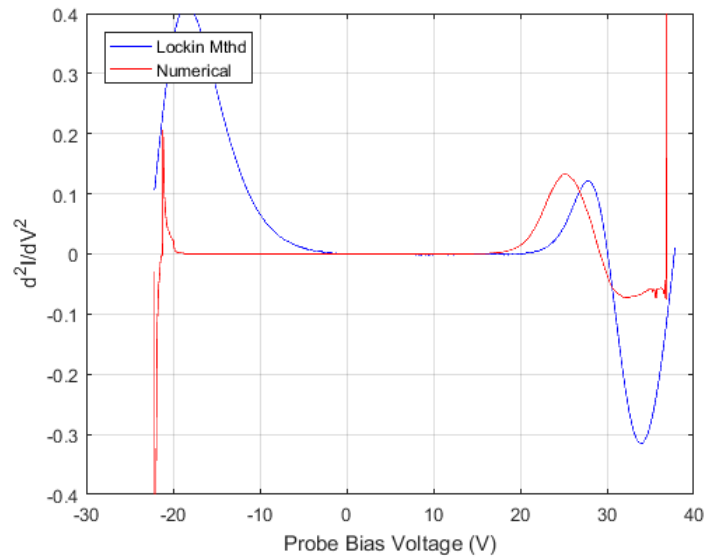


Figure 56: Second derivative using the second harmonic method and numerical differentiation

Figure 57 shows the second derivative, expanded to show the zero-crossing, which is used to determine the plasma potential. For the case shown in Figure 56, the plasma potential determined from the zero-crossing is found to be 28.5 V from the numerical derivative and 30.1 V using the second harmonic method. In other cases the numerical differentiation does not yield such consistent results, distorting the overall shape, not just under predicting the plasma potential. The second derivative is essential to determining the EEDF as it is directly proportional, making the second derivative the most important calculation for determining the EEDF.

Another criterion for determining the quality of the second derivative of the probe current is the voltage difference between the maximum of the second derivative and the zero-crossing. As described in Section 3.2, Godyak [115] states that this difference should be on the order of the electron temperature or less, for a pure Maxwellian distribution. Shown later, the EEDFs here are not pure Maxwellian distributions, but the basis of the theory still applies as it is an indicator of the response time of the measurement circuitry and diagnostic tool. Because even careful application of numerical filtering and smoothing techniques clearly distorted the I-V curve and led to an incorrect numerically differentiated second derivative, the

second harmonic method is the superior method for determining the second derivative of the probe current.

For Test 1:1:1, using the zero-crossing of the measured second derivative, the plasma potential is 30.1 V. As discussed in Section 3.2.5, an estimate of the uncertainty in this measurement is +/- 0.2 V. This is lower than the plasma potential as measured by the emissive probe (36.9 V) for the same operating conditions and configuration, but at a position slightly further downstream. The plasma potential in the cathode plume can change significantly with axial and radial position relative to the keeper orifice; therefore, difference in plasma potential can be attributed to the different axial location of each of the probes, 8 mm vs. 5 mm for the emissive probe and Langmuir probe, respectively. Because the two probes are not in exactly the same location, the plasma potential as calculated by the zero-crossing of the measured second derivative was used exclusively for subsequent analysis and calculation of the EEDF.

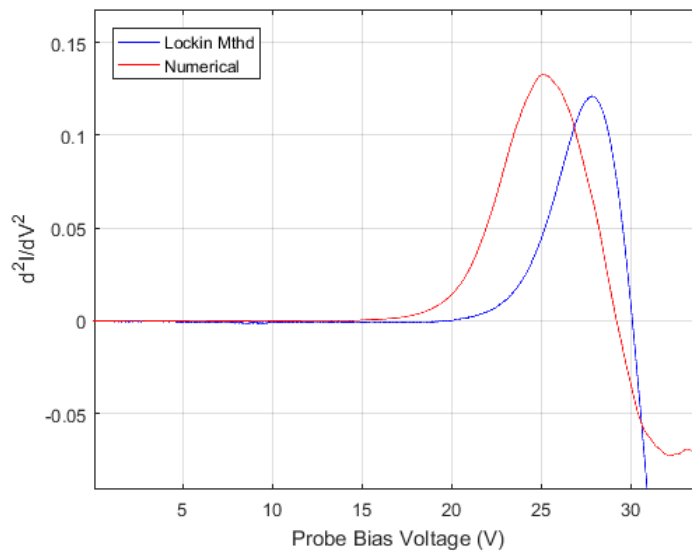


Figure 57: Expanded second derivative zero-crossing

Once the second derivative and plasma potential are known, the EEDF can be calculated. A typical EEDF is shown in Figure 58 and corresponds to Test 1:1:1 operating at the conditions listed in Table 12, below.

Table 12: Test 1:1:1 - LaB₆ cathode with 0.020” operating point for spot mode EEDF

Q (SCCM)	V _K (V)	I _K (A)	V _A (V)	I _A (A)
6	16	1.0	33	2.0

Two distributions are plotted in Figure 58. The solid curve is the EEDF calculated using the measured second derivative determined using the second harmonic method. The dashed line corresponds to a Maxwellian EEDF with a velocity (energy) shift, chosen to match the measured EEDF. The velocity shift could be caused by a double layer just downstream of the keeper exit plane [4]. The double layer is characterized by an increase in the local plasma potential (locally increasing downstream of the keeper exit) that causes the electrons to accelerate. The plasma remains collisionless through the double layer; therefore, the electrons do not thermalize and the Maxwellian distribution is maintained despite the increase in energy [60]. In Chapter 5, the uncertainties for electron temperature, electron drift energy and mean electron energy (calculated from the EEDF) are approximately $\pm 2\%$, $\pm 1\%$ and $\pm 1\%$, respectively.

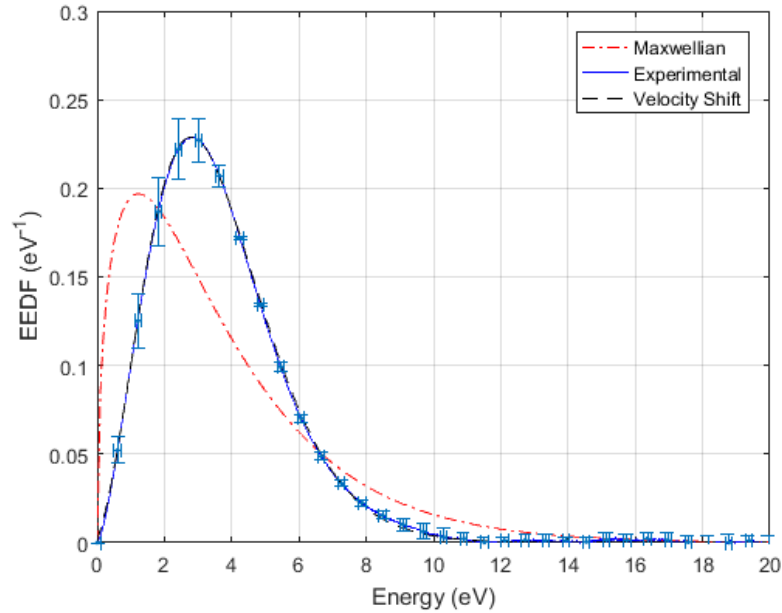


Figure 58: EEDF for LaB₆ cathode operating in spot mode (6 SCCM) with 0.020” orifice (Configuration 1:1:1)

Figure 58 shows the EEDF for the LaB₆ 0.020” orifice cathode operating on xenon (Test 1:1:1) – the corresponding electron temperature is 0.5 eV with a velocity shift of 2.7 eV (991.2 km/sec). The effective electron temperature is 2.5 eV from the integration of the distribution function and was used to plot the Maxwellian distribution in Figure 58. The uncertainty in the plasma potential for this case is approximately 0.1 V.

Reaction Rate Coefficients

The EEDF is a powerful tool and can be used to calculate a number of plasma parameters including the reaction rate coefficients for processes involving electron collisions. The measured EEDFs were used to calculate reaction rate coefficients for several known processes in the cathode plume. A list of these processes can be found in the first column of Table 13.

The reaction rate coefficient is given by the following integral, as described in Section 2.4.4, which can be calculated numerically:

$$\langle \sigma(\varepsilon)v_e(\varepsilon) \rangle = n_e^{-1} \int_0^{\varepsilon_{max}} \sigma(\varepsilon)v_e(\varepsilon)F(\varepsilon)d\varepsilon \quad (5-2)$$

Where σ is the cross section for a given process, F is the experimental EEDF and v_e is the electron velocity, which is expressed as a function of energy, ε as

$$v_e = \sqrt{\frac{2e\varepsilon}{m_e}} \quad (5-3)$$

Electron-xenon impact cross sections for several processes were obtained from the online cross section database, LxCAT [44] and have been reproduced in Figure 59.

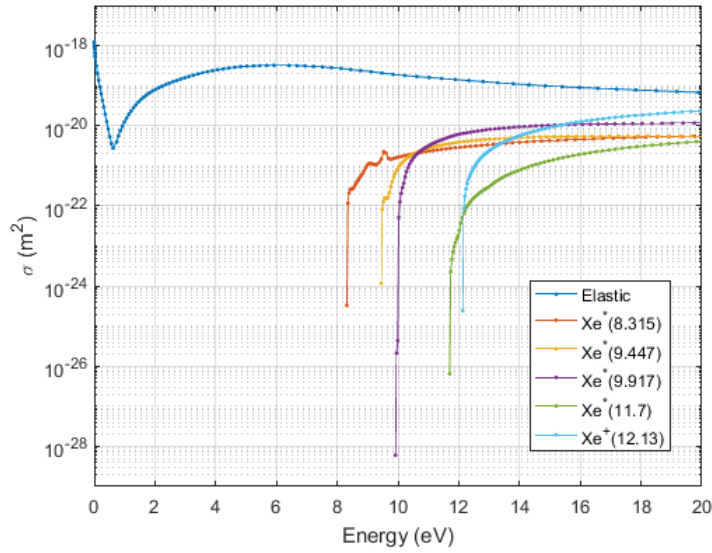


Figure 59: Electron-xenon cross sections for elastic, excitation and ionization [44]

Using the experimental EEDFs and cross section curves, the reaction rate coefficients were calculated by numerical integration in MATLAB. For the cathode operating in spot mode, with the keeper on, at nominal discharge power, the reaction rates for several electron-xenon processes are listed in Table 13.

Table 13: Calculated reaction rates for several electron-xenon processes.

Process	$\langle \sigma v_e \rangle$ (m ³ /sec)	Type
$e^- + Xe \rightarrow e^- + Xe$	$5.41 \cdot 10^{-13}$	Elastic
$e^- + Xe \rightarrow e^- + Xe^*$ (8.315 eV)	$1.27 \cdot 10^{-14}$	Excitation
$e^- + Xe \rightarrow e^- + Xe^*$ (9.447 eV)	$1.68 \cdot 10^{-14}$	Excitation
$e^- + Xe \rightarrow e^- + Xe^*$ (9.917 eV)	$3.29 \cdot 10^{-14}$	Excitation
$e^- + Xe \rightarrow e^- + Xe^*$ (11.7 eV)	$7.06 \cdot 10^{-15}$	Excitation
$e^- + Xe \rightarrow e^- + Xe^+$ (12.13 eV)	$4.48 \cdot 10^{-14}$	Ionization

It is important to highlight the first ionization energy for xenon is 12.13 eV; however, the EEDFs show that a very small fraction (if any) of the electrons have energies above 12.13 eV. The fraction of electrons above the ionization energy is responsible for ionizing the xenon neutrals in the cathode [4].

Plasma Density

Another important plasma parameter determined from the Langmuir probe trace is the plasma density. The method used to obtain the ion density involves the Langmuir probe with the ion current interpreted using Orbit Motion Limited (OML) theory (Section 3.2.2). The OML theory was applied to the current collected in the ion saturation region. Equation (5-4) is adapted from the current collected using OML theory (Section 2.4.3) and is used to determine the ion density using the slope of square of the collected current vs. probe bias potential in the ion saturation regime.

$$n_i = \sqrt{\frac{d(I^2)}{dV_p}} \sqrt{\frac{M_i \pi}{2e e S_p}} \quad (5-4)$$

The square of the current collected in the ion saturation region with linear curve fit is shown in Figure 60.

The slope from the linear fit is used to calculate the ion density.

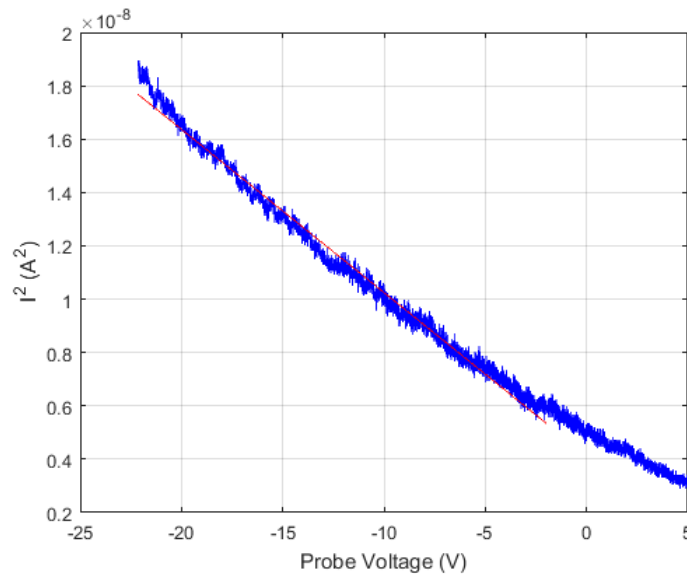


Figure 60: Linear fit to the square of the probe current

For the LaB₆ cathode operating in spot mode, at the nominal power (Test 1:1:1), the plasma density was calculated to be $4.2 \cdot 10^{17} \text{ m}^{-3}$. For this density and the measured electron temperature of 0.5 eV the Debye length is $8.1 \cdot 10^{-6} \text{ m}$. The electron-ion and electron-neutral mean free path compared to probe diameter ($3.1 \cdot 10^6$ and 28, respectively) show that the plasma is in the collisionless regime. The ratio of probe radius-to-Debye-length is 4.70; therefore, since this is close 3 and the plasma is collisionless OML is applicable. Since this ratio is less than 10, thin sheath theory is not applicable. The calculated plasma parameters are listed in Table 14. In Chapter 5, there is an uncertainty of approximately $\pm 20\%$ for all of the plasma density measurements unless otherwise specified.

Table 14: Plasma parameters for the LaB₆ cathode (Test 1:1:1) operating in spot mode

Q (SCCM)	T_e (eV)	$\Delta \epsilon$ (eV)	n_0 (m ⁻³)	λ_D (m)	$\frac{r_p}{\lambda_D}$	$\frac{\lambda_{ei}}{d_p}$	$\frac{\lambda_{en}}{d_p}$
6	0.5	2.7	$4.2 \cdot 10^{17}$	$8.1 \cdot 10^{-6}$	4.70	$3.1 \cdot 10^6$	$2.4 \cdot 10^3$

This is consistent with other density measurements and applicability of ion collection theories in the near keeper region, see Figure 61 [116].

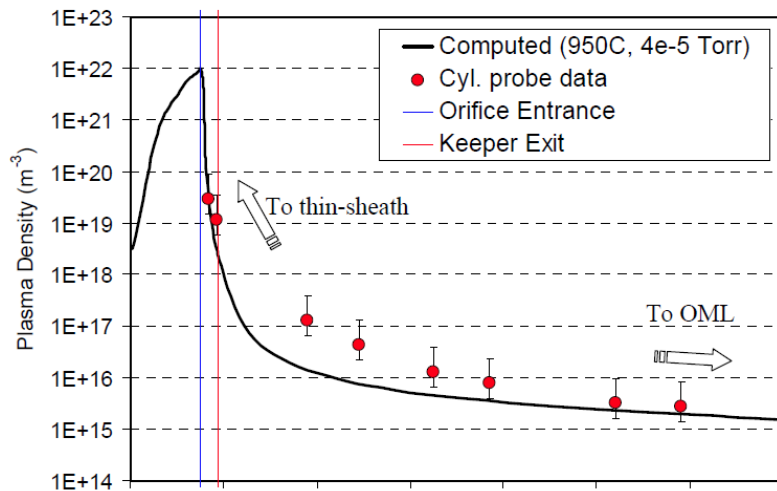


Figure 61: Comparison of the numerical simulation result with the plasma density along the axis of symmetry of the 20-HP cathode [116]

5.1.2 CeB₆ Emitter

This section presents the operating mode and plume characterization for the hexaboride cathode with CeB₆ emitter for three orifice sizes. The analysis follows the same procedure as described in the previous section.

Plume mode vs Spot mode

Three orifice diameters were tested at the same discharge power and the normalized RMS potential measured using a floating emissive probe as done with the LaB₆ cathode for Test 1:1:1. Figure 62 shows the normalized RMS potential for Tests 1:2:1, 1:2:2 and 1:2:3 operating on xenon. In Figure 62, the normalized RMS potential for Tests 1:2:1 (0.020") appears to behave similarly to Test 1:1:1, with the spot mode regime corresponding to a flow rate between 5 SCCM and 7 SCCM. As the orifice diameter increases, with all other operating conditions remaining the same, the flow rate at which the transition to spot mode occurs decreases; between 3 and 4 SCCM for Test 1:2:2 (0.035"), and between 2.25 and 2.75 SCCM for Test 1:2:3 (0.040").

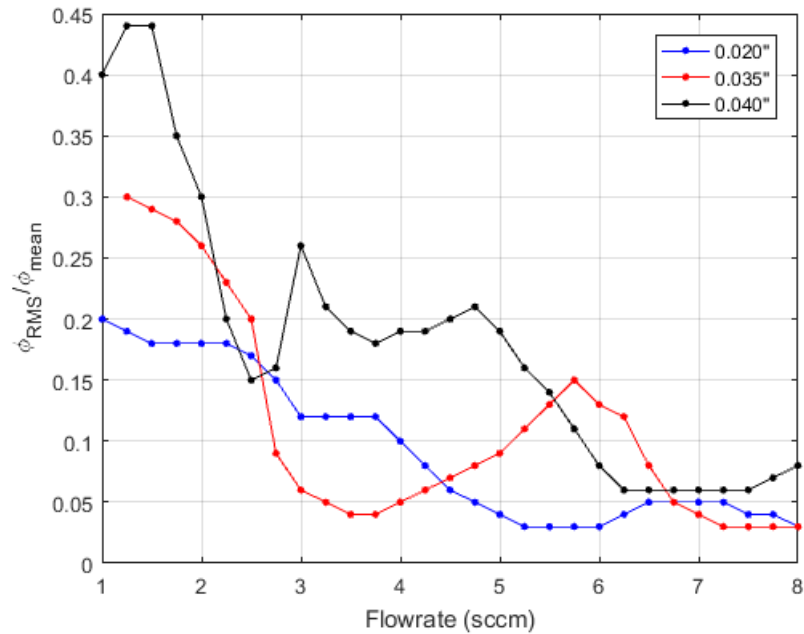


Figure 62: CeB₆ cathode plasma potential levels for various cathode tube orifice diameters operating on xenon

Although the spot mode flow rate transition point decreases as orifice size is increased, there appears to be a lower limit of approximately 2 SCCM where the magnitude of the plasma potential oscillations quickly become larger than the mean.

Langmuir Probe/EEDF

Figure 63 shows the EEDF for the CeB₆ insert with the 0.020"-diameter orifice (Test 1:2:1). The distribution is quite similar to the LaB₆, 0.020"-diameter orifice (Test 1:1:1). The calculated electron temperature is 0.4 eV and the apparent velocity shift corresponds to an energy of 2.7 eV. Again, the energy shift is most likely due to a double layer formed just downstream of the keeper exit plane. For this case the uncertainty in the measured distribution larger than the 0.040"-diameter orifice and the 0.020"-diameter orifice LaB₆ case (Test 1:1:1). The uncertainty in the plasma potential is ± 0.5 V. The larger uncertainty in this particular case could be due to actual fluctuations in the EEDF or a result of the choice of settings on the lock-in amplifier. For example, if one chooses a larger time constant for the low-pass filter this will increase the signal noise.

Figure 64 shows the EEDF for the CeB_6 insert with the 0.040"-diameter orifice. The distribution is similar to the 0.020"-diameter case and displays a velocity shift; however, the calculated electron temperature and velocity shift are slightly higher, 0.8 eV and 3.8 eV, respectively. The higher electron temperature may be due the lower pressure in the cathode orifice.

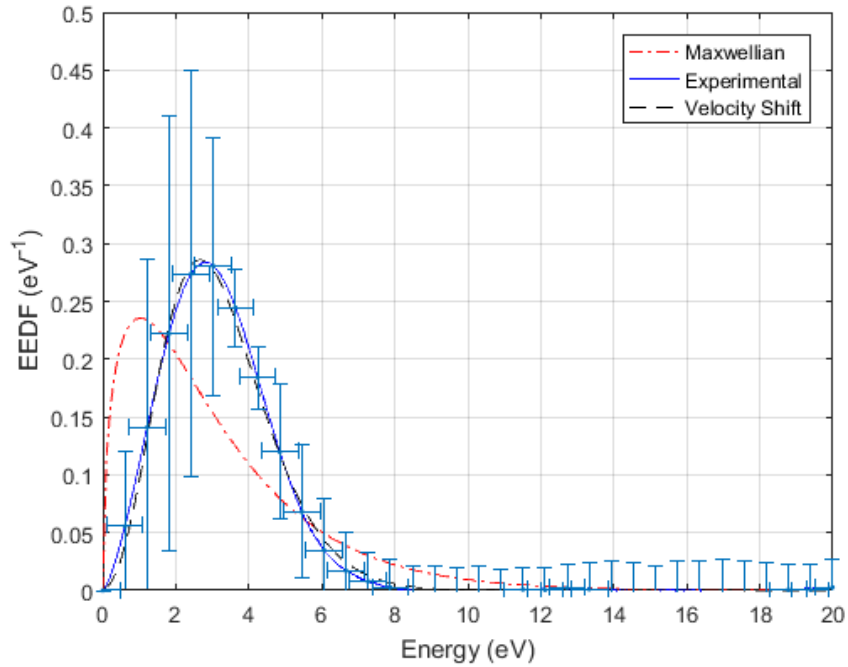


Figure 63: EEDF for CeB_6 cathode operating in spot mode (6 SCCM) with 0.020" orifice (Test 1:2:1)

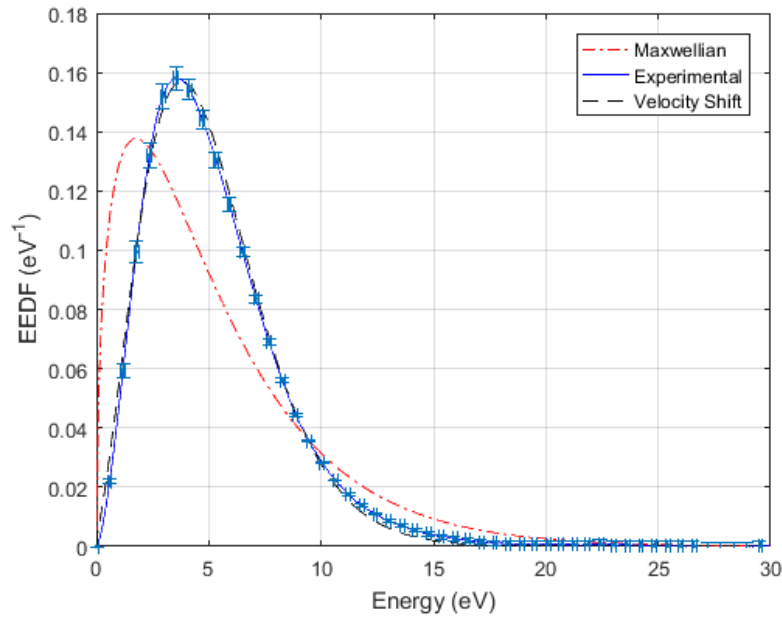


Figure 64: EEDF for CeB₆ cathode operating in spot mode (2.5SCCM) with 0.040” orifice (Test 1:2:3)

Plasma Parameters

Using the measured EEDFs and Langmuir probe IV curves the plasma parameters were calculated for the two extremes of the orifice diameters, corresponding to Tests 1:2:1 and 1:2:3. Table 15 shows the calculated plasma parameters for the CeB₆ cathode by orifice diameter. The plasma density was calculated using both OML and thin sheath collection theories. Both methods show that collisionality is met, but the ratio of the probe-radius-to-Debye-length shows that Thin Sheath Theory is not applicable since this value is less than 10. The plasma density is slightly higher for the larger diameter orifice.

Table 16 shows the calculated reaction rate coefficients for the CeB₆ cathode by orifice diameter. Although the EEDF for the larger diameter orifice has a lower probability at the most-probable electron energy, the reaction rate coefficients are slightly higher since the electron distribution is wider and has a high most-probable energy; therefore, it captures more, higher energy electrons.

Table 15: Plasma parameters for the CeB₆ cathode (Tests 1:2:1 and 1:2:3) operating in spot mode.

Orifice Diameter (in)	Q (SCCM)	T _e (eV)	Δε (eV)	n ₀ (m ⁻³)	λ _D (m)	r _p /λ _D	$\frac{\lambda_{ei}}{d_p}$	$\frac{\lambda_{en}}{d_p}$
0.020	6	0.4	2.7	3.6·10 ¹⁷	7.8·10 ⁻⁶	4.86	3.6·10 ⁶	2.4·10 ³
0.040	2.5	0.8	3.8	4.8·10 ¹⁷	9.6·10 ⁻⁶	3.97	2.7·10 ⁶	5.7·10 ³

Table 16: Reaction rate coefficients for the CeB₆ cathode

Process	0.020" Orifice $\langle\sigma v_e\rangle$ (m ³ /sec)	0.040" Orifice $\langle\sigma v_e\rangle$ (m ³ /sec)
$e^- + Xe \rightarrow e^- + Xe$	$5.42 \cdot 10^{-13}$	$5.57 \cdot 10^{-13}$
$e^- + Xe \rightarrow e^- + Xe^*$ (8.315 eV)	$1.25 \cdot 10^{-14}$	$1.85 \cdot 10^{-14}$
$e^- + Xe \rightarrow e^- + Xe^*$ (9.447 eV)	$1.78 \cdot 10^{-14}$	$2.15 \cdot 10^{-14}$
$e^- + Xe \rightarrow e^- + Xe^*$ (9.917 eV)	$3.51 \cdot 10^{-14}$	$4.47 \cdot 10^{-14}$
$e^- + Xe \rightarrow e^- + Xe^*$ (11.7 eV)	$7.92 \cdot 10^{-15}$	$1.70 \cdot 10^{-14}$
$e^- + Xe \rightarrow e^- + Xe^+$ (12.13 eV)	$5.14 \cdot 10^{-14}$	$1.03 \cdot 10^{-13}$

5.1.3 Discussion

The near-keeper region of a hexaboride (LaB₆ and CeB₆) cathode was interrogated using a floating emissive probe and single Langmuir probe to determine the plasma potential, EEDF, reaction rates for several processes and ion density. The plasma potential measurements using the emissive probe showed low frequency oscillations (<100 kHz) of the plasma potential at low cathode flow rates (<4 SCCM) and spot mode operation between approximately 5 SCCM and 7 SCCM for Tests 1:1:1 and 1:2:1 at the nominal discharge currents. The CeB₆ and LaB₆ emitters behave similarly in terms of discharge power (keeper and anode voltage) and plasma potentials, based on the 0.020"-diameter orifice case. Both emitters show almost identical operating conditions corresponding to the spot mode regime, reaction rates, and mean and RMS plasma potentials for the 0.020" orifice diameter at 6 SCCM at the same discharge current.

For Tests 1:2:1, 1:2:2 and 1:2:3, the CeB₆ emitter was used with three different orifice diameters. The spot-plume mode transition appears to occur at lower flow rates as orifice size is increased, but has a minimum flow rate. This suggests the spot/plume mode transition can be adjusted by cathode geometry; however, the data suggest a minimum flowrate for sustained, stable operation. For all these tests, the minimum flow rate for stable operation is approximately 2.5 SCCM regardless of the orifice diameter. These data suggest that the largest orifice can operate at the lowest flow rate for spot mode operation

based on the local minimum ratio of RMS plasma potential and mean plasma potential; however, the magnitude of this local minimum ratio is highest for the largest orifice. Thus, the optimum orifice diameter for a particular application may require a trade study which includes orifice diameter, discharge current and flow rate. This may have implications for cathode sizing at the systems level based on available power, propellant throughput, required discharge power, etc.

For Tests 1:2:1 and 1:2:3 the EEDF was measured in the near-plume region and reaction rate coefficients calculated for several xenon processes. The EEDFs show higher electron temperatures and drift velocities for the larger orifice diameter. The data also show lower reaction rate coefficients for transitions to the $5p^5(^2P_{3/2}^{\circ})8d$ electron configuration and ionization for the larger orifice diameter. Measurement of the plasma potential structure downstream of a hollow cathode was measured and showed a sharp (almost step-wise) increase in the plasma potential approximately 1.5 cm downstream of the keeper exit [17]. This stepwise increase was attributed to the potential difference across a double layer at that location. The magnitude of the stepwise increase was approximately 4.5-5 volts. The plasma across the double layer (and moving axially downstream of the cathode, towards the anode from the double layer to the anode) is assumed to be collisionless [4]. If the plasma is indeed collisionless, the potential difference across the double layer would accelerate the electrons to a velocity equal to that potential difference. These electrons would not thermalize and a bulk drift velocity would remain for the population of electrons. Thus, the measured stepwise 5 V potential difference would result in an electron drift energy of approximately 5 eV. These values (potentials and drift energies) are consistent with the measured electron drift energies measured in this work.

There exists a potential gradient between the keeper and anode, resulting in ions moving towards the keeper and electrons toward the anode. The keeper will have the lowest potential between the keeper and anode; however, the potential drop between a point in the near-keeper and the keeper will be relatively small compared to the total potential drop between the keeper and anode. The total flux of ions and electrons will adjust to maintain quasineutrality and ions traveling across the double layer will be

accelerated towards the keeper (just as electrons are accelerated away). (The space-charge-limited current across the double layer was described in Section 2.4.2.) Therefore, even in spot mode operation, ions are accelerated in near-keeper region towards the keeper. It is possible that when the cathode is operated with a HET the double layer will move further due to the higher neutral density provided by the HET. This may increase the potential drop between the double layer and the keeper, increasing the energy of the ions impacting the keeper and exacerbating erosion.

The drifting electron population may encourage IAT in the cathode plume, suggesting that cathode geometry plays a significant role in the formation of IAT. IAT occurs when the electron drift velocity exceeds the local ion velocity. It was observed that cathode orifice size has an effect on the magnitude of IAT, where a larger diameter orifice resulted in a lower magnitude of turbulence [27]. The suggested mechanism for the increase in the magnitude of the turbulence with smaller orifice diameter was an increase in the electron drift or “streaming velocity”. The current density is given by $j = nqv_{ave} = I/A$, where A is the cross sectional area and v_{ave} is the relative streaming velocity between ions and electrons. Measurements by Yanes et al. verified that the number density was the same for all three orifice diameters tested, thus a smaller orifice results in a higher streaming velocity for electrons [27].

It has been reported that CeB₆ becomes harder to start with continued use, possibly indicative of an increase in the work function, as evident by an increase in the keeper voltage required for ignition [117]. While this voltage was not explicitly recorded, this phenomenon was not observed with the LaB₆ or CeB₆ emitters.

5.2 BaO Cathode Study (Configuration 1)

The experimental setup for this configuration was described in Section 4.4.1. Several attempts to operate the cathode on iodine were made with each of the four inserts. Table 18 provides a complete summary of the testing and exposure history for each insert. The basic procedure was to condition and start the cathode normally using only xenon, and then introduce iodine. Table 17 provides complete conditioning

and starting procedures as prescribed by Busek Co. Inc. Once stable cathode operation on xenon was established, zones 2 and 3 would be heated above the scheduled pot temperature. Once the zone 2 and 3 temperatures were stable, the pot would be heated. Once the pot reached the desired temperature iodine was introduced (opening V1) while xenon was still flowing. This resulted in a xenon/iodine vapor mixture (of unknown concentration) supplied the cathode. Once stable cathode operation using the mixture was established, the xenon flow would be stopped, leaving the cathode to operate solely on iodine vapor.

Table 17: BaO cathode conditioning and starting procedures

- Conditioning -		
Duration (minutes)	Flow rate (SCCM)	Heater Current (A)
30	1.5	0
90	1.5	2
90	1.5	4
30	1.5	6
- Starting -		
5-20	1.0	6.5
Apply keeper voltage, 300-600V		

In most cases where iodine vapor was introduced to the propellant flow, the cathode plume would extinguish after a few moments of operating on a mixture. Typically, the cathode operation could be recovered by starting again with xenon only. The cathode did not consistently re-start after iodine exposure and sometimes required significant (15-60 minutes at 6A) heating before operation with xenon could resume. As the testing progressed, changes were constantly being made to the setup in order to improve the iodine delivery and ensure uncontaminated (i.e. oxygen free) propellant (xenon and iodine) was reaching the cathode insert.

Four, short BaO emitters were used in the same cathode, one for each Trial listed in Table 10, all sectioned from the same original full-length emitter. The inserts were numbered and tested separately corresponding to Tests 2:1:1, 2:1:2, 2:1:3 and 2:1:4. For each Test (or insert) multiple attempts were made to operate the cathode on xenon, iodine or both. Each attempt is identified by a letter. To reference

a specific attempt the Test label will be amended with a “-letter” corresponding the attempt. For example, for Test 2:1:1, attempt “G” the amended configuration would be 2:1:1-G. A complete test history for each insert is shown in Table 18. Briefly, the test history for each insert is listed here:

- Insert 1 (Test 2:1:1) may have been abandoned prematurely due to inexperience with hot insert exposure to iodine; since later tests showed normal cathode operation could be recovered after (sometimes lengthy) heating periods.
- Insert 2 (Test 2:1:2) was most likely poisoned with oxygen; since nominal cathode operation on xenon was never established.
- Insert 3 (Test 2:1:3) was the most successful in terms of running the cathode repeatedly and with iodine as the sole propellant. In one test in particular, 3A, the cathode ran stably on iodine vapor for several minutes.
- Insert 4 (Test 2:1:4) ran well on xenon and was exposed to iodine, but stopped responding (starting on xenon) before introducing iodine during normal operation. An effort to establish reliable, repeatable, stable cathode operation was made before making further adjustments to the iodine delivery system. These adjustments involved thoroughly insulating the iodine feed lines to ensure proper heating of the iodine within the lines. Since stable, repeatable operating appeared to be achievable, the adjustments were made to the iodine feed system. On the next test following the changes, the cathode no longer responded to xenon and normal cathode operation was never established again. A procedural change was also made during this test that involved evacuating the pot to low pressure (below 0.1 psia) and back filling with xenon to a few psia prior to cathode conditioning. This procedural change was an effort to eliminate or reduce the possibility of exposing the hot insert to oxygen upon introducing iodine.

Table 18: Complete BaO cathode testing summary

Insert No.	Test Case	Exposed to			Cathode status	Outcome/comments
		Xenon	Mixture	Iodine		
1	A	X			conditioned	Keeper interference, no attempt to start
	B	X			conditioned, ran	
	C	X			Cold, no heater	Pumping speed calculation
	D	X			cold, heater tape (HT) on	
	E	X			conditioned, ran, HT on	
	F				cold, HT on (I ₂ calibration)	No cathode, only calibration plug. Tubing melted on Calibration 2.
	G	X	X		conditioned, ran, HT on	Tubing melted (replaced with SS)
	H	X	X		conditioned, ran, HT on	
	I	X		X	conditioned	Cathode would not start, tried to start on iodine only
2	A	X			conditioned, no start	
	B	X			conditioned, no start	
	C	X			conditioned	Brief start but unstable
	D	X			conditioned, no start	
	E	X			conditioned, no start	
3	A	X	X	X	conditioned, ran, HT on	Ran stably on I₂ ONLY
	B	X	X		conditioned, ran, HT on	
	C	X	X		conditioned, ran, HT on	
	D	X	X		conditioned, ran, HT on	
	E	X			conditioned, no start	
	F	X			conditioned, no start	
4	A	X			conditioned, ran	HT failure
	B	X			conditioned, ran	Test aborted, failure to evacuate the Pot
	C	X	X		conditioned, ran	No restart after iodine introduced.
	D	X			conditioned, ran	Zone 3 HT failure
	E	X			conditioned, ran	Heater power supply malfunction
	F	X			conditioned, no start	
	G	X			conditioned, ran	
	H	X			conditioned, no start	
	I	X			conditioned, no start	
	J	X			conditioned, ran	
	K	X			conditioned (truncated), ran	
	L	X			conditioned (truncated), ran	
	M	X			conditioned, no start	
	N	X			conditioned, no start	

In Figure 65, the three states of cathode operation are presented corresponding to Test 2:1:3-A; at left, the cathode is operating on xenon only, at middle, operating on a xenon/iodine mixture, and at right, operating on only iodine vapor. A distinct plume color change is visible between xenon only and mixture operation. An even greater color change is visible from the mixture to iodine only operation. The cathode operated on iodine vapor for several minutes, it might have operated longer, however the keeper electrode melted due to the intense heat provided from the discharge. It was difficult to determine the temperature of the keeper electrode by visual inspection and no adjustment operating parameters was made since the cathode appeared to be running stably. At the time, it was assumed that subsequent testing of the cathode on iodine would allow for optimization of the cathode operating parameters and allow for longer cathode operation on iodine propellant.

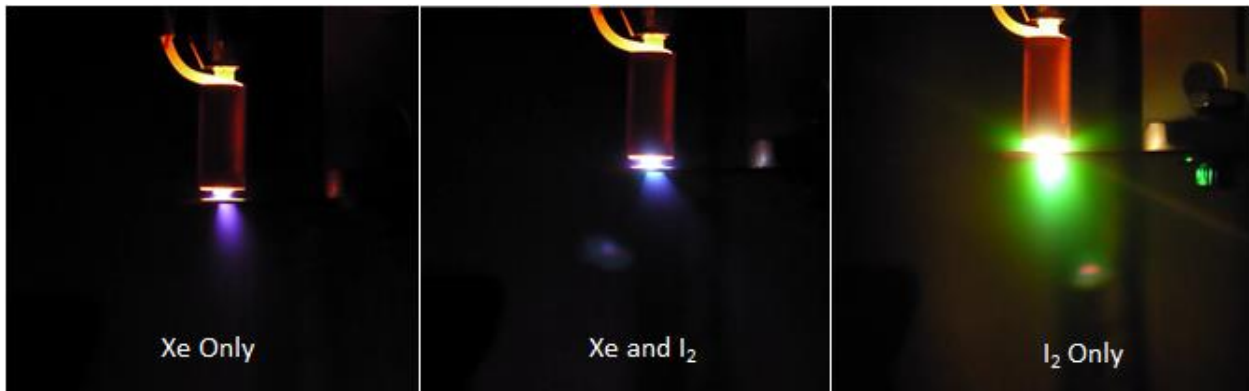


Figure 65: BaO cathode operating on xenon propellant (left), mixture of xenon (middle) and iodine, and iodine vapor (right)

From the images of the cathode in operation on both propellants (Figure 65), by visual inspection it is clear that the cathode is much hotter while operating on iodine propellant. Table 19 lists the cathode operating conditions for operation on both xenon (Figure 65, left) and iodine (Figure 65, right). During cathode operation, the keeper power supply was in current limited mode, while the anode was in voltage limited mode. The keeper voltage required to maintain 0.6 A of keeper current is larger with iodine compared to xenon. The anode current extracted from the cathode is much lower with iodine compared to xenon.

Table 19: BaO cathode (Configuration 1) operating parameters on xenon and iodine

Propellant	V_K (V)	I_K (A)	V_A (V)	I_A (A)	T_{pot} (°C)	P_L (torr)	Q (SCCM)
Xenon	11	0.6	40	0.127	-	-	3
Iodine	72	0.6	40	0.024	51	1	-

Energy Dispersive X-Ray Spectroscopy (EDS) was performed on each of the inserts a single time after tests in which the emitter had been exposed to various levels of xenon and/or iodine—these results are shown in the following figures. In each figure, the top image shows the location of interrogation as marked by marker at the upper left corner of the pink box. The lower image shows the spectrum at the interrogation location. In some cases, certain peaks have been identified and correspond to particular elements of interest. A large peak (significantly above the noise floor) is evidence of a strong signal from a particular element. Figure 66 shows the EDS interrogation locations at several points on the emitter.

Figure 67 shows the EDS results for Insert 1 (Test 2:1:1) at a location along the inside of the emitter (corresponding to location 1 in Figure 66), which had been cut in half lengthwise. At the time the analysis was performed Insert 1 had been run on xenon and exposed to iodine, but never ran stably on iodine. The EDS for Insert 1 shows several tungsten peaks.

Figure 68 shows the EDS results for Insert 2 (Test 2:1:2) at a location on the face of the emitter. Insert 2 was only exposed to xenon and likely poisoned early on in testing by inadvertent exposed to oxygen. The EDS for Insert 2 shows several peaks including tungsten, barium, tantalum, calcium and oxygen.

Figure 69 shows the EDS results for Insert 3 (Test 2:1:3) on the edge of the inside diameter. At the time of the analysis, Insert 3 had operated on xenon and iodine. The EDS for Insert 3 shows several strong peaks for tantalum.

Figure 70 shows the EDS results for Insert 4 (Test 2:1:4) at a location on the face of the emitter. At the time of the EDS analysis, Insert 4 had not been exposed to any propellant or inserted into the cathode. The EDS analysis for Insert 4 shows several peaks for tungsten.

The EDS analysis did not show any signs of iodine at any of the interrogation locations. This is surprising for the emitters which were exposed to iodine as some trace amounts were expected to exist on the emitter surface. It is possible that the emitter surfaces were too hot for any iodine to condense on the surface and thus, no iodine will be present. If iodine were to form a compound, which would likely have a higher vapor pressure than pure iodine since it would have condensed at the higher surface temperature, the EDS analysis would have detected an iodine peak.

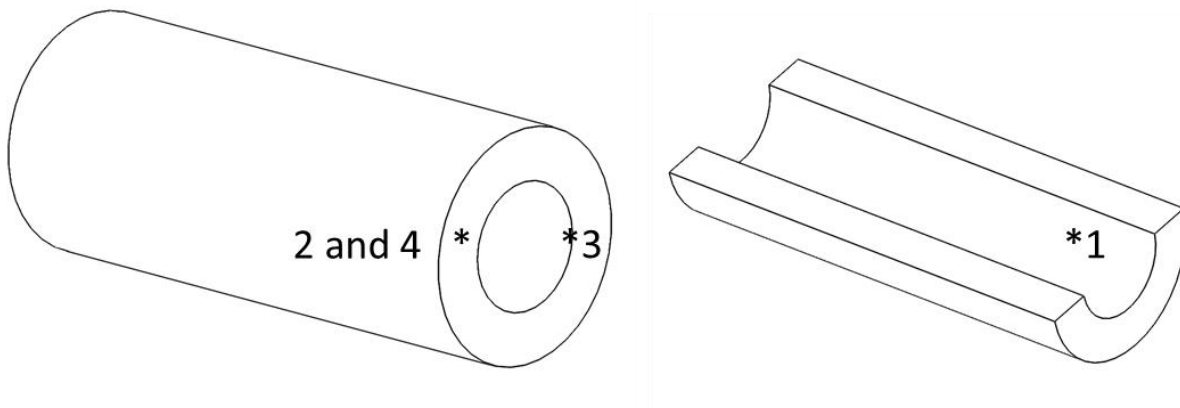


Figure 66: EDS interrogation locations.

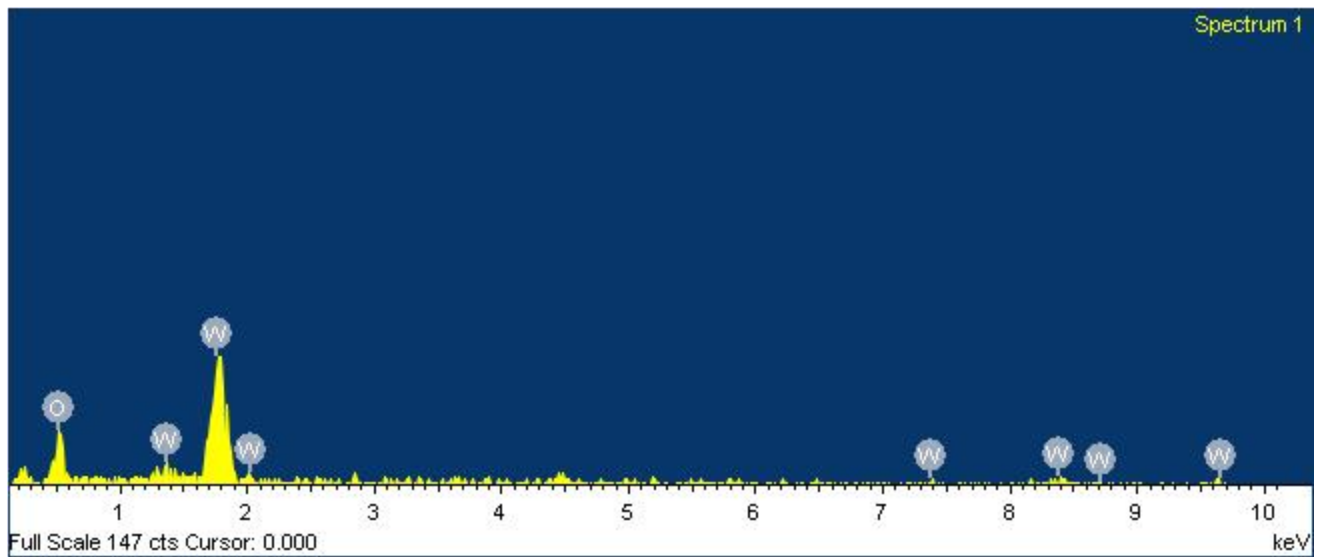
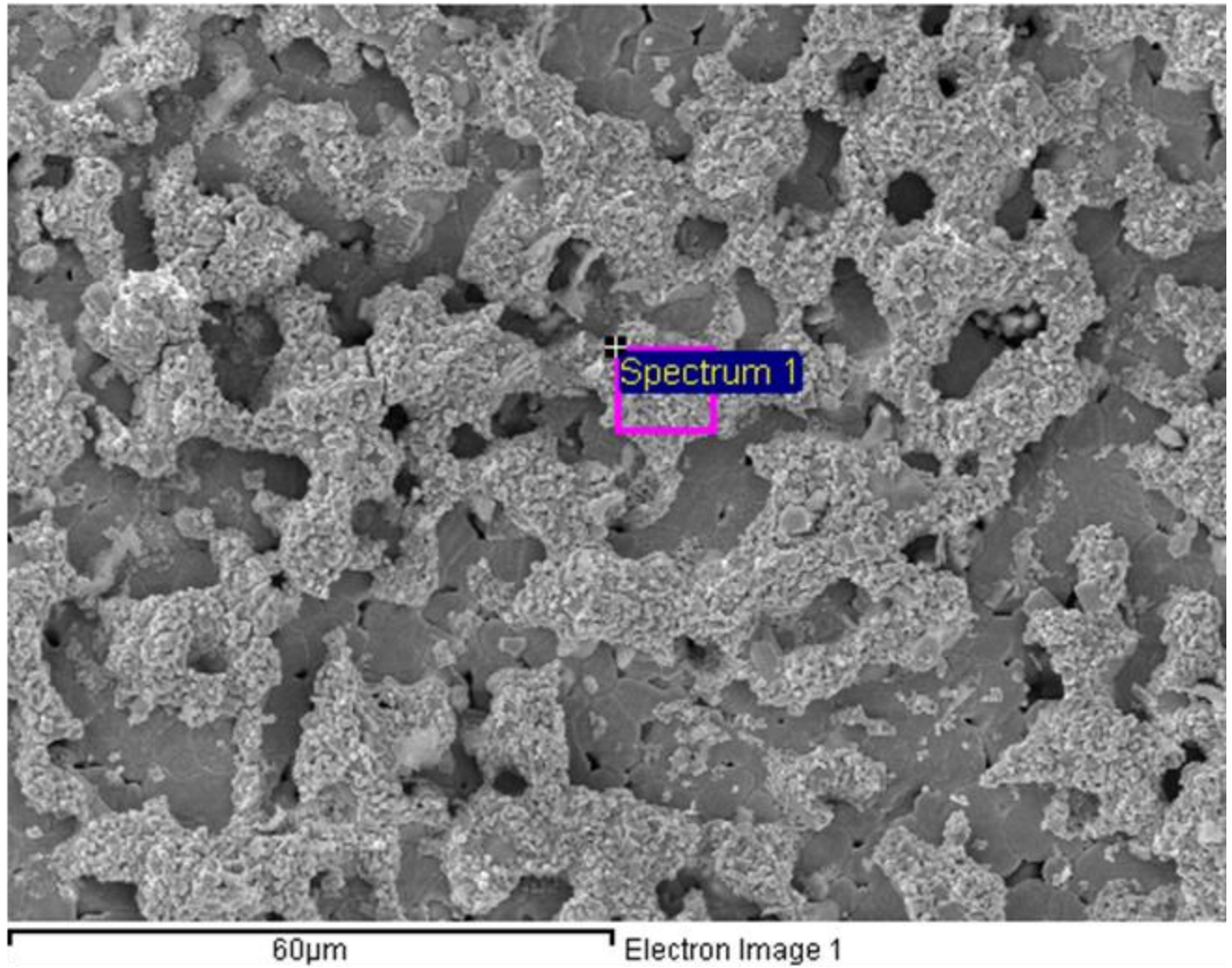


Figure 67: EDS of Insert 1 (Test 2:1:1) along inner diameter (cut in half lengthwise).

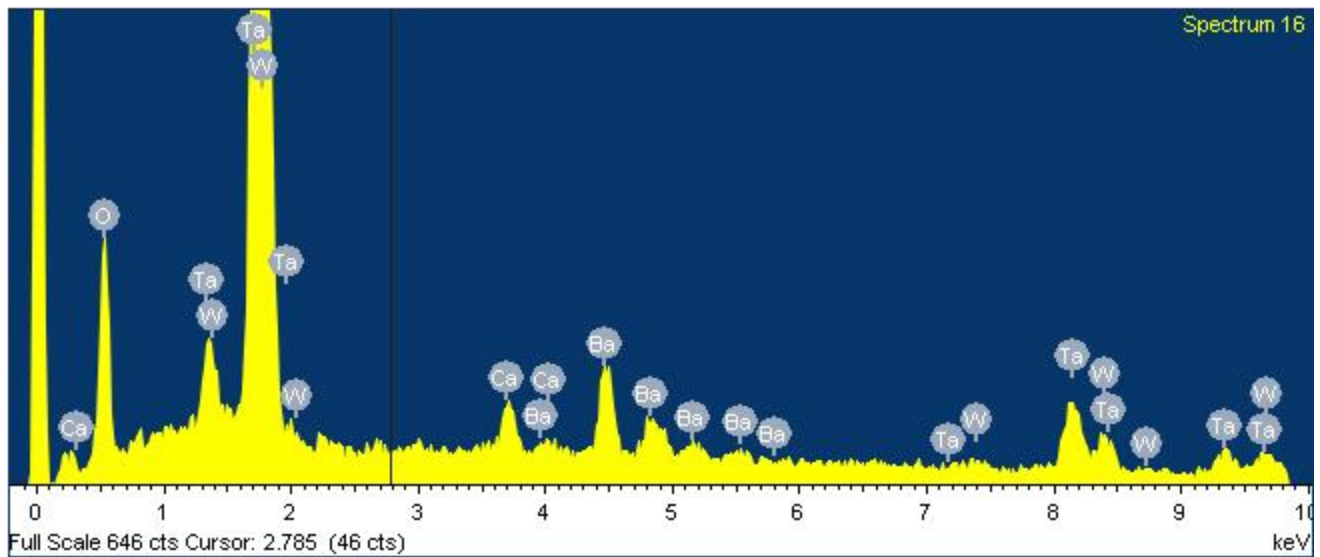
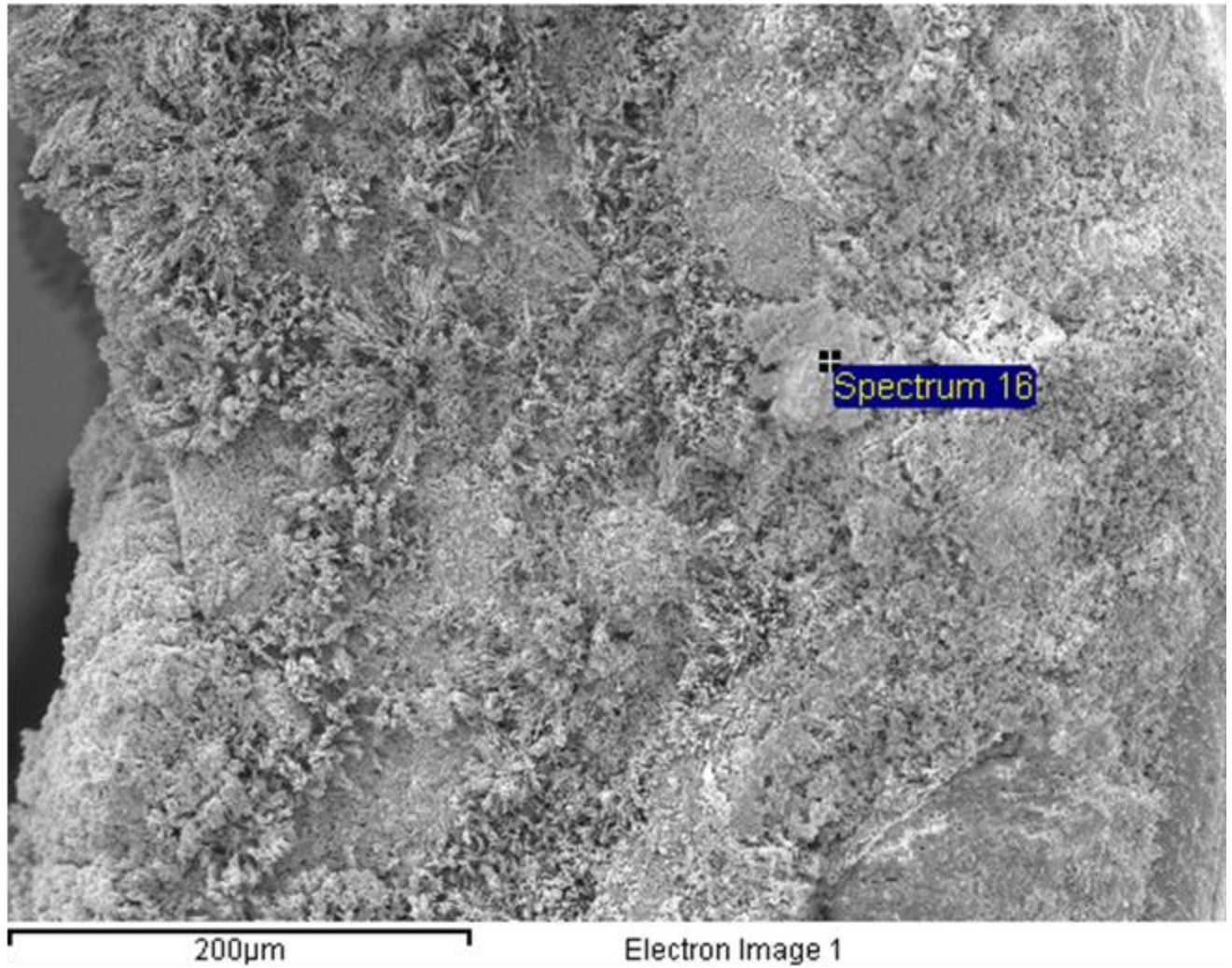


Figure 68: EDS for Insert 2 (Test 2:1:2) on front face of emitter.

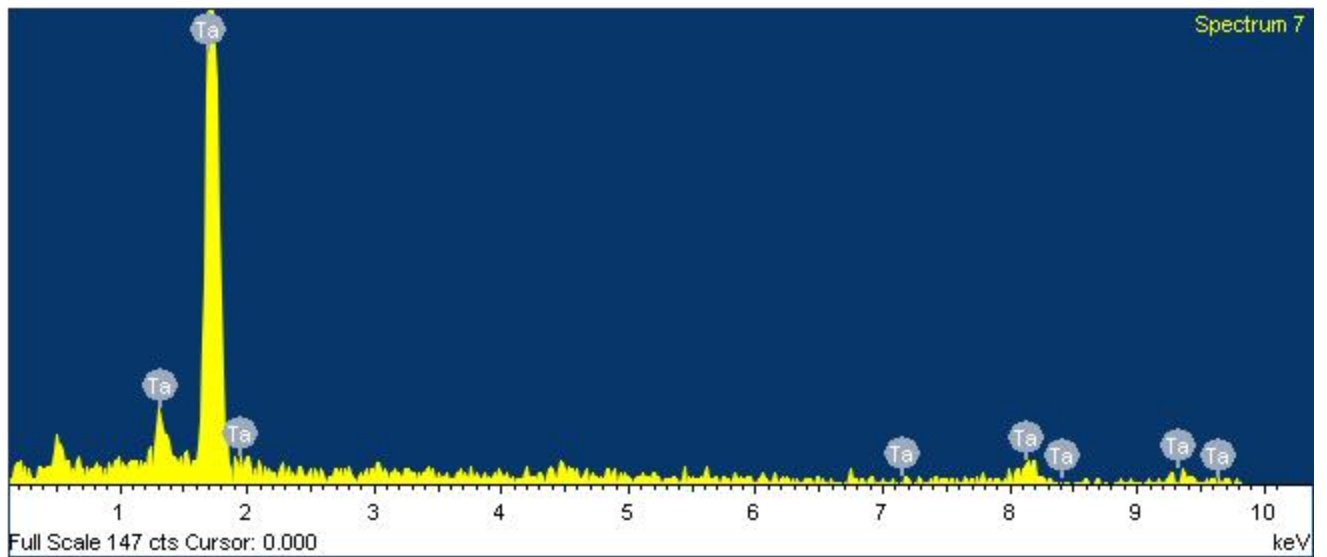
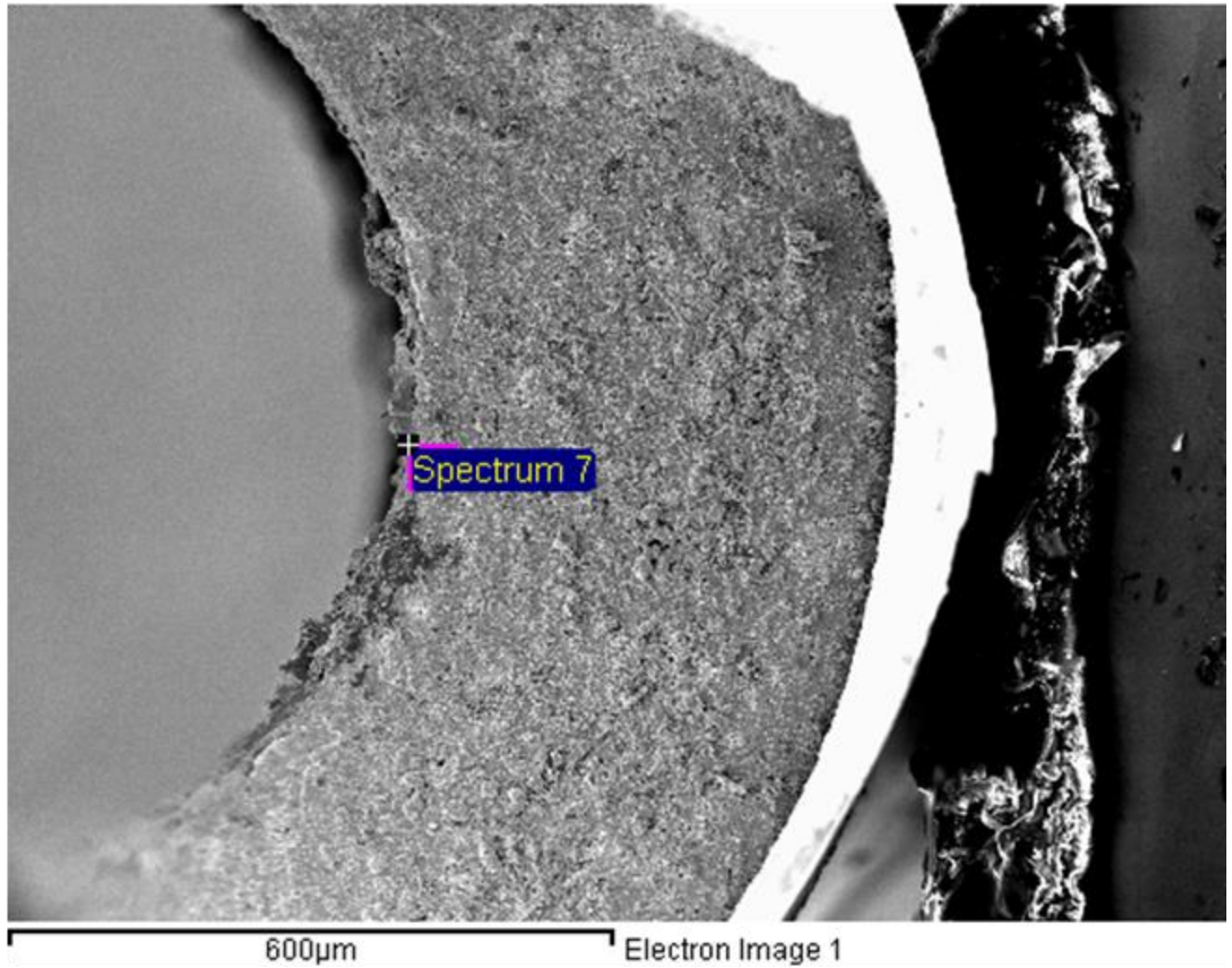


Figure 69: EDS for Insert 3 (Test 2:1:3) on inside edge of emitter.

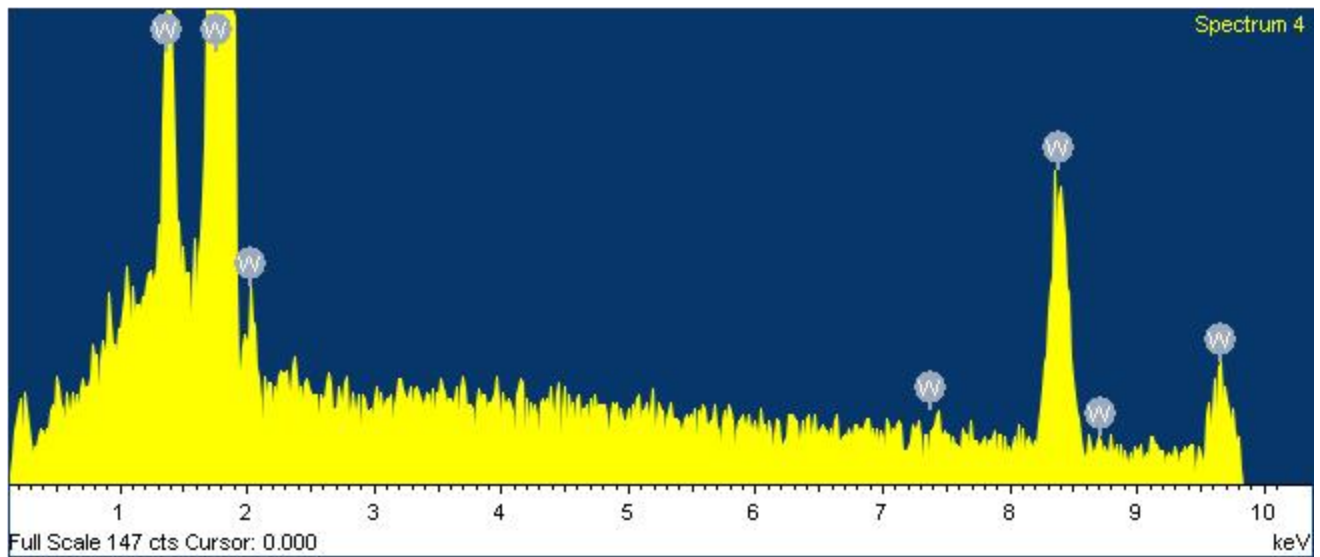
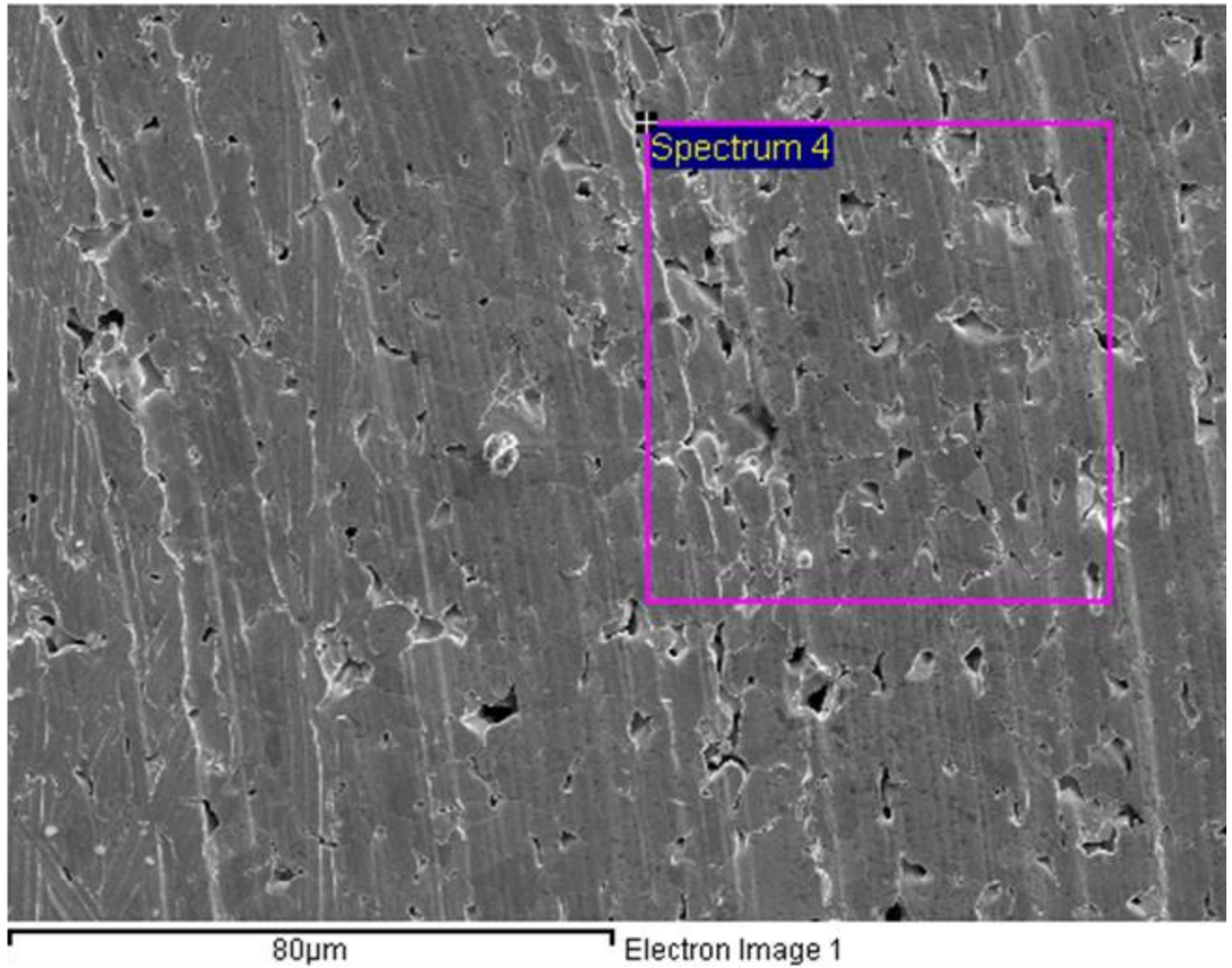


Figure 70: EDS for Insert 4 (Test 2:1:4) on front face of emitter.

5.3 BaO Cathode Study (Configuration 2)

This section presents the plume characterization for the BaO hollow cathode operating on xenon (Test 3:1:1) and iodine (Test 3:2:1). The experimental setup for this configuration was described in Section 4.4.2. For this experiment the cathode was operated at relatively high discharge current to maintain stable cathode operation. First the BaO cathode functionality was confirmed on xenon. Then the cathode was run on iodine and plume data was taken. Finally, the cathode was run again on xenon and plume data was taken. Table 20 shows the nominal cathode operating conditions for the xenon (Test 3:1:1) and iodine (Test 3:2:1) propellants for the plume characterization.

Table 20: BaO cathode (Configuration 2) operating conditions on xenon and iodine

Propellant	V_K (V)	I_K (A)	V_A (V)	I_A (A)	T_{pot} (°C)	P_{pot} (torr)	Q (SCCM)
Xenon	27	0.25	51	3.1	-	-	6
Iodine	30	0.25	65	3.1	52	8	-

For xenon, the iodine feed system was bypassed entirely to avoid contamination (cathode running on a mixture of residual iodine and xenon). A flow rate of 6 SCCM was selected for these tests. This was determined to be the minimum flow rate found for stable cathode operation. Figure 71 shows the cathode operating on xenon and iodine.



Figure 71: BaO hollow cathode in operation on xenon (left) and iodine (right).

5.3.1 Xenon Propellant

This section reports the plume data for Test 3:1:1 for a BaO operating on xenon propellant. The plasma potential was measured using a floating emissive probe, and plasma characteristics and EEDF measured using a single Langmuir probe.

Plasma Potential Measurements

Figure 72 shows the plasma potential time history as measured by a floating emissive probe for the nominal operating point listed in Table 20 for Test 3:1:1. The mean plasma potential was 29.2 V and the RMS 2.5 V. Figure 73 shows the PSD estimate for the plasma potential. A slight hump is noticeable around 100 kHz; however, a sharp peak is clear at 10 kHz. The 10 kHz mode observed and shown in Figure 73 is too low and coherent to be considered ion acoustic oscillations (50 to 1000 kHz), which are typically incoherent. Plasma potential fluctuations in this frequency range could be caused by ionization instabilities (50 to 250 kHz), which can be triggered by certain combinations of cathode operating conditions and geometry (i.e. orifice diameter, keeper-cathode spacing, etc.). The xenon plume shows strong oscillations around 10 kHz.

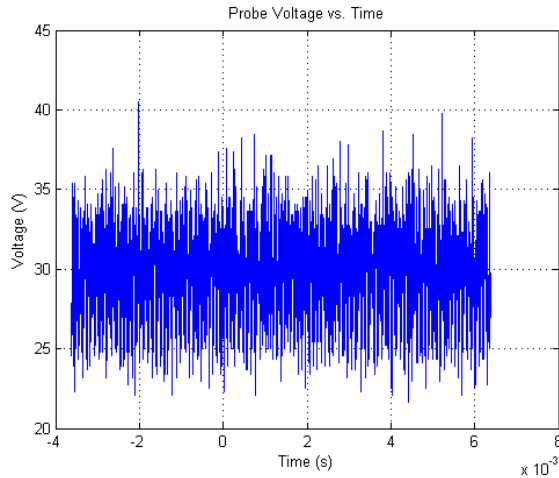


Figure 72: Emissive probe voltage (plasma potential) for BaO cathode operating on xenon

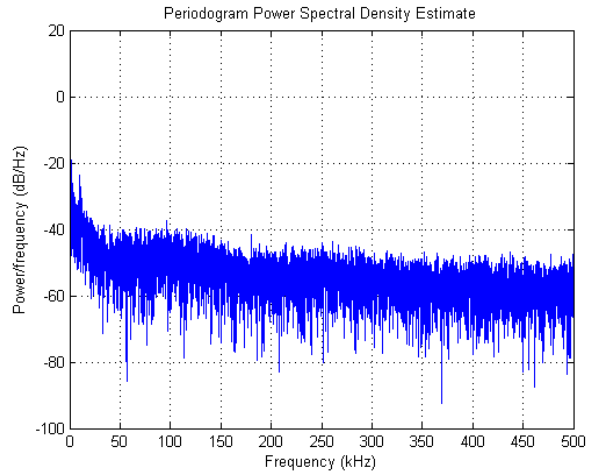


Figure 73: Power Spectral Density (PSD) of plasma potential in BaO cathode plume operating on xenon

Langmuir Probe/EEDF

The EEDF for the BaO cathode operating on xenon is well represented by a Maxwellian distribution with a velocity shift. Table 21 lists the calculated electron properties including electron temperature, velocity shift (determined to fit a Maxwellian to the measured EEDF), electron Mach number and mean electron energy based on the measured EEDF. Since there is a bulk electron drift, the mean electron energy cannot be used to calculate the electron temperature; however, the mean electron energy is an important parameter for comparing the EEDF of an atomic plasma (xenon) to a molecular plasma (iodine, I_2). Due to the bulk drift velocity, the Slope Method is also not an applicable method to calculate the electron temperature, and is derived from Thin Sheath Theory which is not applicable due to the ratio of probe-radius-to-Debye length being too large. There are a few ways to express an electron Mach number, but for this work it is defined as the ratio of the electron drift velocity over the electron thermal speed (or electron temperature). Another common definition is the ratio of the electron drift velocity over the ion temperature.

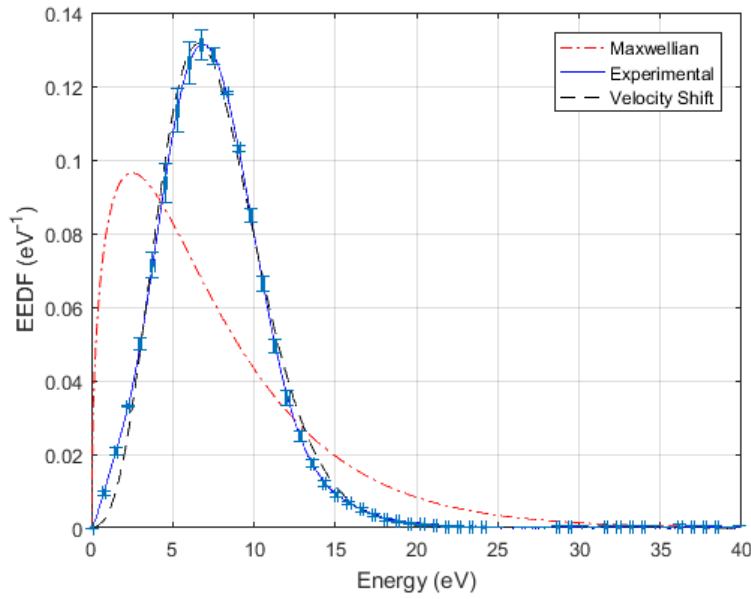


Figure 74: EEDF in BaO cathode plume operating on xenon

Table 21: Electron properties as calculated by several methods for xenon propellant

T_e (eV), Integration	Mean Energy (eV)	T_e (eV), Slope Method	T_e (eV), Floating Potential	T_e (eV)	$\Delta\varepsilon$ (eV)	Mach No
5.0	7.5	2.0	4.6	0.7	6.6	3.1

Plasma Density

The plasma density calculated using OML theory is $5.6 \cdot 10^{17} \text{ m}^{-3}$. Using the effective electron temperature from the integration of the EEDF the Debye length is $2.2 \cdot 10^{-5} \text{ m}$, which results in a probe-radius-to-Debye-length ratio of 1.72. Although the criterion for collisionality is met, this ratio is too low for Thin Sheath theory to be applicable for any plasma parameter calculations. Table 22 shows the plasma density and ion collection theory criteria for this case.

Table 22: Plasma density and ion collection theory criteria

Q (SCCM)	n_0 (m^{-3})	λ_D (m)	r_p/λ_D	$\frac{\lambda_{ei}}{d_p}$	$\frac{\lambda_{en}}{d_p}$
6	$5.6 \cdot 10^{17}$	$2.2 \cdot 10^{-5}$	1.72	$2.3 \cdot 10^6$	$2.4 \cdot 10^3$

Reaction Rates

Table 23 shows the reaction rate coefficients for several processes in a xenon plasma for Test 3:1:1. The reaction rates are calculated using the measured EEDF and cross section data using the process described in Section 5.1.1.

Table 23: Reaction rate coefficients for the BaO cathode operating on xenon

Process	$\langle\sigma v_e\rangle$ (m ³ /sec)	Type
$e^- + Xe \rightarrow e^- + Xe$	$4.44 \cdot 10^{-13}$	Elastic collisions
$e^- + Xe \rightarrow e^- + Xe^*$ (8.315 eV)	$1.66 \cdot 10^{-14}$	Excitation
$e^- + Xe \rightarrow e^- + Xe^*$ (9.447 eV)	$1.83 \cdot 10^{-14}$	Excitation
$e^- + Xe \rightarrow e^- + Xe^*$ (9.917 eV)	$3.87 \cdot 10^{-14}$	Excitation
$e^- + Xe \rightarrow e^- + Xe^*$ (11.7 eV)	$1.68 \cdot 10^{-14}$	Excitation
$e^- + Xe \rightarrow e^- + Xe^+$ (12.13 eV)	$1.01 \cdot 10^{-13}$	Ionization

5.3.2 Iodine Propellant

This section reports the plume data for Test 3:2:1 for a BaO operating on iodine propellant. The plasma potential was measured using a floating emissive probe and plasma characteristics and EEDF measured using a single Langmuir probe.

Plasma Potential Measurements

Figure 75 shows the time history of the plasma potential for the BaO cathode operating on iodine at the nominal operating point. For this case, the mean plasma potential was 43.7 V and the RMS was 0.76 V. The mean plasma potential is significantly higher with iodine than the case with xenon (29.2 V). Some high frequency oscillations can be seen in the PSD, but they are quite low in amplitude. The strong, low frequency oscillations seen with xenon are not present with iodine.

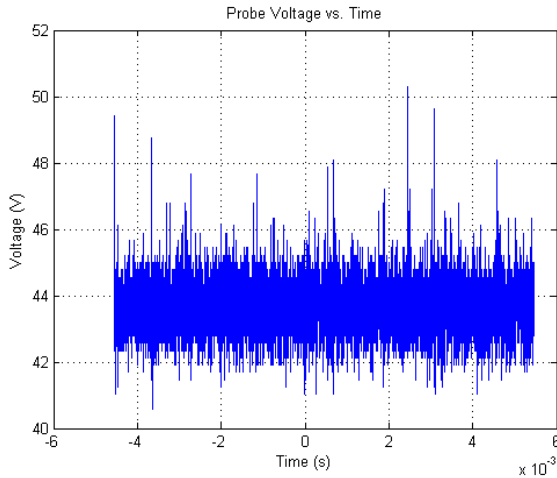


Figure 75: Emissive probe voltage (plasma potential) for BaO cathode operating on iodine

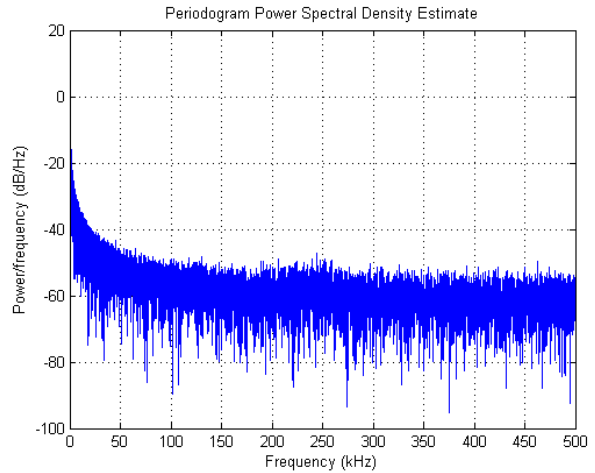


Figure 76: PSD of plasma potential in BaO cathode plume operating on iodine

Langmuir Probe/EEDF

Figure 77 shows the EEDF just downstream of the keeper exit for the cathode operating on iodine. The EEDF is more similar to a Maxwellian distribution than the EEDF for the cathode operating on xenon. This could be due to a higher flow rate resulting in a higher pressure and neutral density since it is difficult to precisely know the iodine flow rate. Later measurements of the iodine mass flow rate suggest that the iodine mass flow rate for this test was as high as 30% larger than the xenon mass flow rate (for 6 SCCM). Table 24 shows the electron properties calculated from several methods for Test 3:2:1. From the measured EEDF, the calculated electron temperature is 1.3 eV and the velocity shift corresponds to an energy of 4.2 eV.

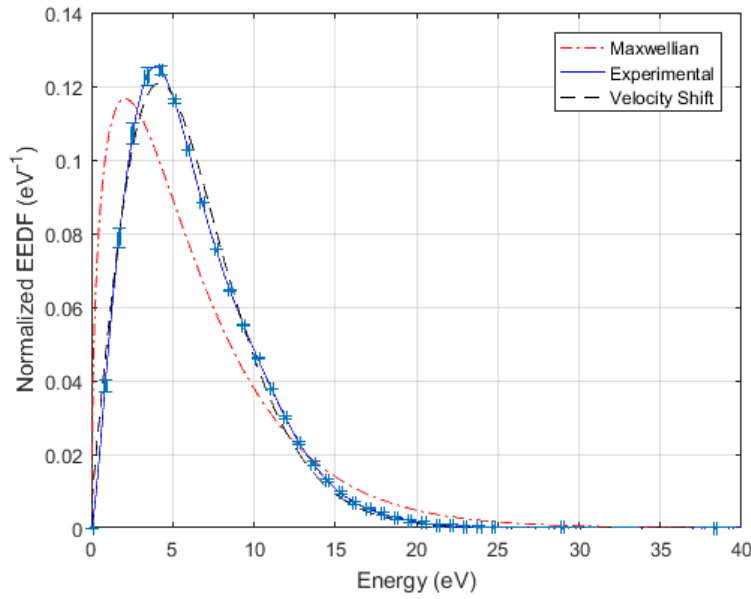


Figure 77: EEDF in BaO cathode plume operating on iodine

Table 24: Electron properties as calculated by several methods for iodine propellant

T_e (eV), Integration	Mean Energy (eV)	T_e (eV), Slope Method	T_e (eV), Floating Potential	T_e (eV)	$\Delta\epsilon$ (eV)	Mach No
4.2	6.2	3.2	5.0	1.3	4.2	1.8

Plasma Density

The plasma density calculated using OML theory is $6.8 \cdot 10^{17} \text{ m}^{-3}$. Using the electron temperature from the integration of the EEDF the Debye length is $1.9 \cdot 10^{-5} \text{ m}$, which results in a probe-radius-to-Debye-length ratio of 1.89. Although, the collisionality criterion is met, this ratio is too low for Thin Sheath theory to be applicable for any plasma parameter calculations. Table 25 shows the plasma density and ion collection theory criteria for this case. For this case, the iodine mass flow rate was set equal to the xenon mass flow rate.

Table 25: Plasma density and ion collection theory criteria

Q (SCCM)	n_0 (m^{-3})	λ_D (m)	r_p/λ_D	$\frac{\lambda_{ei}}{d_p}$	$\frac{\lambda_{en}}{d_p}$
-	$6.8 \cdot 10^{17}$	$1.9 \cdot 10^{-5}$	1.89	$1.9 \cdot 10^6$	$2.3 \cdot 10^3$

Reaction Rates

Cross sections for collisional processes in a xenon plasma are readily available in a number of sources and databases. Cross sections for iodine reactions were difficult to find in the literature, thus the literature review presented in Section 2.4.6 describes all of the cross sections found. These cross sections were digitized from the figures provided in each reference and interpolated, then used with the measured EEDF to calculate the reaction rate coefficient for the particular collisional process. These cross sections are reproduced in Figure 78.

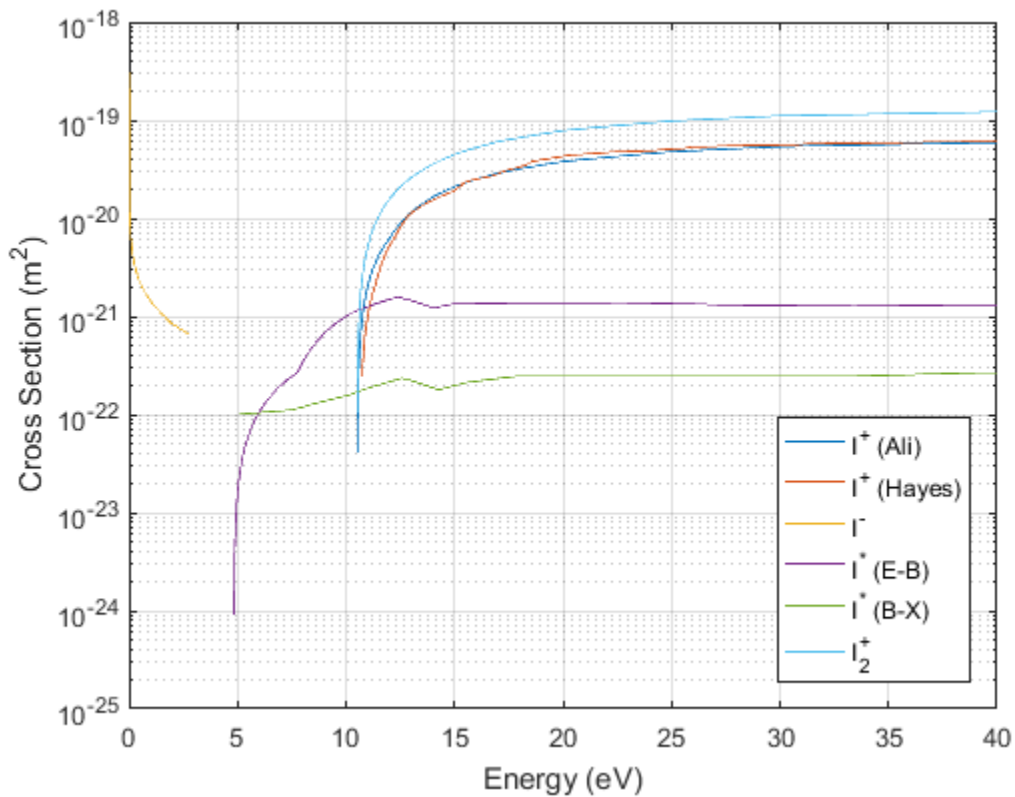


Figure 78: Cross sections for several collisional processes for iodine.

Table 26 shows the reaction rate coefficients for several processes in an iodine plasma for Test 3:2:1. The reaction rates are calculated using the measured EEDF and cross section data using the process described in Section 5.1.1.

Table 26: Reaction rate coefficients for the BaO cathode operating on iodine

Process	$\langle\sigma v_e\rangle$ (m ³ /sec)	Description
$e^- + I \rightarrow e^- + I^+$	$8.85 \cdot 10^{-14}$	Ionization from Ali [43]
$e^- + I \rightarrow e^- + I^+$	$9.63 \cdot 10^{-14}$	Ionization from Hayes [67]
$e^- + I \rightarrow I^-$	$1.09 \cdot 10^{-16}$	Dissociative Attachment
$e^- + I_2 \rightarrow e^- + I_2^*$ (E-B)	$2.59 \cdot 10^{-15}$	Excitation E-B
$e^- + I_2 \rightarrow e^- + I_2^*$ (B-X)	$4.56 \cdot 10^{-16}$	Excitation B-X
$e^- + I_2 \rightarrow e^- + I_2^+$	$1.85 \cdot 10^{-13}$	Molecular Ionization

5.3.3 Discussion

A low power, BaO-W hollow cathode was operated on xenon and iodine propellants. Its performance, power consumption and plume properties were reported for xenon and iodine with the cathode at similar operating conditions for each. The overall performance of the BaO cathode on iodine was comparable to xenon. The BaO cathode required slightly higher power for ignition and discharge maintenance, as evident by the slightly higher operating power. The cathode operated at slightly higher power for operation on iodine, requiring a keeper voltage of 30 V (27 V for xenon) and an anode voltage of 65 V (51 V for xenon). Since the iodine flow rate could not be determined, but it was corroborated with supplemental data that it was indeed higher than the xenon flow rate, the difference in operating power could simply be explained by difference in flow rate from xenon to iodine. One reason may be related to equivalent mass and volumetric flow rates of xenon and iodine. Since iodine is a molecular gas, an equivalent mass flow rate of iodine can be achieved at roughly half of the volumetric flow rate of iodine. However, because iodine may not be fully dissociated at the cathode emitter, there could be roughly half the number of candidates to ionize.

The ultimate cause of the higher required power is unknown; however, likely causes include kinetic processes associated with molecular plasmas. Two processes specific to molecular plasmas are rotational and vibrational excitation. These two processes do not provide a path to ionization in plasmas where excitation and ionization are driven by electron impact. Typically, in molecular plasmas, the number of

low energy electrons is much lower when compared to an equivalent atomic plasma. The reduction in the low energy population of electrons reflects the energy depletion due to rotational and vibrational excitation collisions. Therefore, the mean energy of electrons is smaller for molecular plasmas. Since the cathode could not be operated on pure, atomic iodine since iodine sublimates as a molecule, a reasonable comparison must be made to the atomic xenon case. At the same discharge conditions, the EEDFs for iodine show a lower mean electron energy than with xenon (6.2 eV for iodine and 7.5 eV for xenon), which is consistent with molecular plasmas.

Another process specific to certain molecular plasmas is dissociative attachment ($e^- + I \rightarrow I^-$). This process is specific to ions with an affinity to capture an electron and maintain a negative ion state. Examples include, but are not limited to hydrogen (H_2), oxygen (O_2), sulfur hexafluoride (SF_6) and iodine (I_2) discharges. Dissociative attachment results in the generation of a neutral atom and a negative ion. This could potentially be a significant electron loss mechanism since the product of the process does not include an electron. The significance of this reaction could be determined using the EEDF to calculate the reaction rate of this process; however, that would require knowledge of the negative ion number density. Negative ions generated in the near plume of the discharge will “see” a relatively large potential hill towards the anode and behave like electrons from the standpoint of an electrical circuit. If a significant population of negative ions exists in the near plume it could impact coupling to the anode and the local plasma.

As with the hexaboride cathode study, the measured EEDFs for both xenon and iodine propellants resemble a shifted Maxwellian distribution. When iodine is compared to xenon, the electron temperature is higher, but the energy corresponding to the shift is smaller in magnitude and relative to the respective electron temperature. This may be a result of low energy electrons being consumed by low energy processes such as dissociative attachment as already discussed. The shift in the Maxwellian may be caused by several factors including electron acceleration through a double layer and/or electron streaming (drift velocity). For electrons being accelerated across a double layer in an iodine plasma the presence of

negative ions will affect the double layer potential and effectively reduce the electron flux; thus, lowering the electron acceleration. For electron streaming, molecular processes could be inhibiting electron transport to the anode, effectively lowering the electron velocity. The reaction rate coefficient is small for the dissociative attachment process, but not small enough to be neglected entirely. Thus, negative ions may play a role in the operation of a cathode on iodine.

The reaction rate coefficient for ionization of atomic iodine is approximately an order of magnitude smaller than the reaction rate coefficient of ionization for xenon. Since it is likely that molecular iodine is mostly dissociated in the near-plume region, ionization of atomic iodine may be the dominant reaction for ion generation. However, electron energy will be lost to the dissociation process, lowering the probability of ionization.

The reaction rate coefficients for the electronic excitation reactions (Table 26) are small but non-negligible compared with the other reaction rate coefficients. The reaction rate coefficient for molecular ionization is at least an order of magnitude larger than the next smaller reaction rate coefficient. Since it is likely that most of the iodine has been dissociated by the time it has reached the near-plume region, these values may be artificially inflated since this calculation assumes a plasma of 100% molecular iodine. Therefore, although these processes may play a role in lowering the effective electron energy, their influence in the near plume region may be much reduced compared to their role in the insert plasma, where the degree of dissociation may be lower. Regardless of where they occur, these processes will reduce the effective electron energy, lowering the probability of ionization.

Low frequency (< 50 kHz) modes were not observed in the plasma potential measurements for iodine propellant as they were in measurements for xenon propellant. Coherent oscillations are commonly observed in the near-plume of hollow cathodes operating on xenon propellant [4]. The suppression of low-frequency oscillations with iodine may be a result of higher neutral density (if the iodine flow rate is higher than xenon), lower mean electron energy and/or molecular processes. These processes will lower

the mean energy of the electron population; they may inhibit the growth of plasma waves and suppress ion acoustic turbulence in the cathode plume.

Chapter 6 Conclusions and Future Work

Although hexaboride emitters have been used for decades in Russia, their use in the U.S. is still in its infancy and limited to laboratory testing. Furthermore, the performance CeB_6 is not well established but appears to be quite similar to LaB_6 for a given orifice and cathode geometry. Given the beneficial characteristics of CeB_6 , its lower evaporation rate for example, its use may have a significant impact on long duration missions and overall cathode lifetime. Further testing of LaB_6 and, specifically, CeB_6 emitters is necessary to understand the lifetime and performance.

Orifice geometry plays a significant role in determining the spot mode operation of a cathode. There does appear to be a minimum flow rate where plume mode is induced regardless of orifice geometry. Therefore, orifice geometry may drive efficient cathode-thruster coupling and lifetime. Further investigation of orifice geometry on spot/plume mode operation should include changes in discharge power since both discharge current and flow rate drive overall thruster performance.

In all cases, the measured EEDF in the near plume region displayed a distribution resembling a Maxwellian with a velocity shift. Lobbia and Beal [92] claim that a cylindrical Langmuir probe, when oriented parallel to the anisotropic drift component (of ions), can only measure the non-drifting EEDF component perpendicular to the probe surface. However, this claim is made in the context of a drifting ion population with a significant velocity above the Bohm speed, without any mention of the resulting effect on the EEDF. Future work must consider a drifting electron population and refine the measurement strategy to account for this phenomenon.

It is believed that electron drift velocity plays a role in the development of IAT in the near plume region, which may generate high-energy ions and lead to accelerated keeper erosion. Further investigation is required to confirm the measured electron drift velocity and to determine how the drift velocity and EEDF evolve in the rest of the cathode plume. The measured drift velocity should also be compared to the local ion temperature to determine how the local Mach number can influence IAT development.

To the best of the author's knowledge, a BaO hollow cathode was operated for the first time on iodine propellant, the plume interrogated with plasma probes, and its performance compared to operation on xenon. The introduction of iodine into the feed system of a running cathode is not trivial, and requires careful procedural and facility considerations to avoid insert contamination. For example, the initial procedure required the pot (reservoir) to be evacuated to low vacuum and then isolated prior to cathode conditioning. This introduced the possibility for contamination of the cathode by oxygen exposure since the pot is at low pressure during the lengthy conditioning and starting procedure. There is always the possibility that oxygen (air) will enter the pot since perfect vacuum is impossible. To prevent or reduce the likelihood of oxygen entering the pot, it was backfilled with xenon after the evacuation and sealed. This practice would also reduce or eliminate the pressure drop previously associated with opening the vapor supply line (from low vacuum) to introduce iodine vapor to the cathode. It is believed that the pressure drop associated with the transition from xenon to xenon/iodine mixture operation caused a loss of orifice pressure extinguishing the cathode discharge.

Precise iodine flow control is imperative for future cathode work with iodine vapor propellant. The pressure transducer intended to correlate line pressure with iodine flow rate was contaminated with iodine condensate and not reliable over the entire temperature range required to prevent under-heating of the feed lines. Commercial-off-the-shelf mass flow controllers are available for condensable gases and should be incorporated in future cathode tests with iodine propellant.

The cathode required higher discharge power to operate on iodine when compared to xenon propellant. This may be the result of a lower effective electron energy due to losses resulting from molecular processes such as electronic and vibrational excitation, and dissociation. This issue is exacerbated by electron attachment processes which cause the loss of an electron from the plasma and creation of a negative ion. The negative ion generation may have implications beyond simple performance (power) losses since it will be accelerated towards the keeper, possibly enhancing keeper erosion.

Future work should investigate the EEDF for a cathode operating in plume mode as the characterization of the plasma in plume mode may provide insight into plasma chemistry. Measuring the EEDF in plume mode is complicated by the strong oscillations of the plasma potential. These oscillations will cause a flattening of the Langmuir probe trace in the exponential region, much like the effect an RF plasma has on the probe trace. One option may be to characterize the plasma potential oscillations and electrically compensate for them, as is done in RF plasmas. In RF plasmas the fundamental frequency is known, in the case of a cathode operating in plume mode the identifying the fundamental frequency and underlying waveform will not be as straightforward.

In summary, this work improved the understanding of hexaboride cathode emitters and mechanisms that contribute to keeper electrode and cathode orifice erosion by demonstrating low-power cathode operation on two hexaboride emitters, including CeB_6 which has little published test results. The operational boundaries for spot mode operation were identified for several cathode orifice diameters, which showed the flow rate corresponding to spot mode operation decreases with increasing orifice diameter for a given discharge current. The EEDF was also measured in spot mode for two different cathode orifice diameters and reaction rate coefficients calculated. These distributions resemble a shift Maxwellian distribution suggesting there is a bulk electron drift velocity. They also show a lower electron temperature and drift velocity for a cathode with a small orifice at higher flow rate.

This work also improved the understanding of BaO hollow cathode operating on iodine propellant and plasma chemistry in the near-keeper plume by demonstrating a BaO hollow cathode operating on iodine propellant measuring the plume properties in the near-keeper region. The measurement of the EEDF in the near-keeper plume and the calculation of reaction rates provide understanding into dominant processes in the plume of a hollow cathode operating on iodine propellant. These measurements and calculations provide insight into possible mechanisms for the observed power loss for a cathode operating on iodine. To this end, a thorough literature review was conducted which resulted in a database of cross sections for collisional processes for iodine relevant to the EP community.

References

- [1] S. Hawking, "Wall Street Journal," 6 September 2013. [Online]. Available: <https://www.wsj.com/articles/SB10001424127887324577304579054903119099932>. [Accessed 18 March 2017].
- [2] G. P. Sutton and O. Biblarz, *Rocket Propulsion Elements*, Hoboken: John Wiley & Sons, Inc., 2010.
- [3] R. G. Jahn, *Physics of Electric Propulsion*, Mineola: Dover Publications, Inc., 2006.
- [4] D. M. Goebel and I. Katz, *Fundamentals of Electric Propulsion: Ion and Hall Thrusters*, Hoboken: Wiley, 2008.
- [5] P. A. Abell, D. D. Mazanek, D. M. Reeves, P. W. Chodas, M. M. Gates, L. N. Johnson and R. L. Ticker, "The Asteroid Redirect Mission (ARM)," in *47th Lunar and Planetary Science Conference*, The Woodlands, 2016.
- [6] E. Y. Choueiri, "A Critical History of Electric Propulsion: The First Fifty Years (1906-1956)," in *40th AIAA/ASME/SAE/ASEE Joint Propulsion Conference and Exhibit*, Ft. Lauderdale, 2004.
- [7] R. J. Cybulski, D. M. Shellhammer, R. R. Lovell, E. Domino and J. T. Kotnik, "Results from SERT I Ion Rocket Flight Test," NASA, Washington, D.C., 1965.
- [8] J. S. Sovey, V. K. Rawlin and M. J. Patterson, "Ion Propulsion Development Projects in U. S.: Space Electric Rocket Test 1 to Deep Space 1," *Journal of Propulsion and Power*, vol. 17, no. 3, pp. 517-526, 2001.
- [9] P. Chabert and N. Braithwaite, *Physics of Radio-Frequency Plasmas*, Cambridge: Cambridge University Press, 2011.
- [10] M. Domonkos, "A Particle and Energy Balance Model of the Orificed Hollow Cathode," in *38th AIAA/ASME/SAE/ASEE Joint Propulsion Conference & Exhibit*, Indianapolis, 2002.
- [11] J. Polk, C. Marrese, B. Thornber, L. Dang and L. Johnson, "Temperature Distributions in Hollow Cathode Emitters," in *Joint Propulsion Conference*, Fort Lauderdale, 2004.
- [12] D. M. Goebel and E. Chu, "High Current Lanthanum Hexaboride Hollow Cathodes for High Power Hall Thrusters," in *32nd International Electric Propulsion Conference*, Wiesbaden, 2011.
- [13] J. Polk, "The Effect of Reactive Gases on Hollow Cathode Operation," in *42nd AIAA/ASME/SAE/ASEE Joint Propulsion Conference & Exhibit*, Sacramento, 2006.

- [14] M. T. Domonkos and J. G. J. Williams, "Investigation of Keeper Erosion in the NSTAR Ion Thruster," in *27th International Electric Propulsion Conference*, Pasadena, 2001.
- [15] A. Sengupta, J. Brophy and K. Goodfellow, "Status of the Extended Life Test of the Deep Space 1 Flight Spare Ion Engine After 30,352 Hours of Operation," NASA, AIAA Paper 2003-4558, 2003.
- [16] I. Katz, J. R. Anderson, D. M. Goebel, R. Wirz and A. Sengupta, "Plasma Generation Near an Ion Thruster Discharge Chamber Hollow Cathode," in *39th Joint Propulsion Conference and Exhibit*, Huntsville, 2003.
- [17] I. M. I. G. Katz and D. M. Goebel, "Model of the Plasma Potential Distribution in the Plume of a Hollow Cathode," in *40th Joint Propulsion Conference*, Fort Lauderdale, 2004.
- [18] D. Herman, "The Use of Electrostatic Probes to Characterize the Discharge Plasma Structure and Identify Discharge Cathode Erosion Mechanisms in Ring-Cusp Ion Thrusters," University of Michigan, PhD Thesis-, 2005.
- [19] D. M. Goebel, K. K. Jameson, I. Katz and I. G. Mikellides, "Potential Fluctuations and Energetic Ion Production in Hollow Cathode Discharges," *Physics of Plasmas*, vol. 14, no. 10, p. doi: <http://dx.doi.org/10.1063/1.2784460>, 2004.
- [20] I. Katz, I. Mikellides, D. M. Goebel, K. K. Jameson and L. K. Johnson, "Production of High Energy Ions Near an Ion Thruster Discharge Hollow Cathode," in *42nd Joint Propulsion Conference and Exhibit*, Sacramento, 2006.
- [21] D. M. Goebel, K. Jameson, I. Katz and I. G. Mikellides, "Energetic Ion Production and Keeper Erosion in Hollow Cathode Discharges," in *29th International Electric Propulsion Conference*, Princeton, 2005.
- [22] I. G. Mikellides, D. M. Goebel, B. A. Jorns, J. E. Polk and P. Guerro, "Numerical Simulations of the Partially-ionized Gas in a 100-A LaB6 Hollow Cathode," in *33rd International Electric Propulsion Conference*, Washington D.C., 2013.
- [23] B. A. Jorns, I. G. Mikellides and D. M. Goebel, "Temporal Fluctuations in a 100-A LaB6 Hollow Cathode," in *33rd International Electric Propulsion Conference*, Washington D.C., 2013.
- [24] I. Mikellides, I. Katz, D. M. Goebel and K. K. Jameson, "Evidence of nonclassical plasma transport in hollow cathode for electric propulsion," *Journal of Applied Physics*, vol. 101, no. 6, p. 063301, 2007.
- [25] I. G. Mikellides, I. Katz, D. M. Goebel, K. K. Jameson and J. E. Polk, "Wear Mechanisms in Electron Sources for Ion Propulsion, II: Discharge Hollow Cathode," *Journal of Propulsion and Power*, vol. 24, no. 4, pp. 866-879, 2008.

- [26] A. L. Ortega and I. G. Mikellides, "The importance of the cathode plume and its interactions with the ion beam in numerical simulations of Hall thrusters," in *34th International Electric Propulsion Conference*, Hyogo-Kobe, 2015.
- [27] N. J. Yanes, P. Guerra-Vela, A. J. Friss, J. E. Polk, B. A. Jorns and J. Austin, "Ion Acoustic Turbulence and Ion Energy Measurements in the Plume of the HERMeS Thruster Hollow Cathode," in *52nd AIAA/SAE/ASEE Joint Propulsion Conference*, Salt Lake City, 2016.
- [28] K. R. Trent, M. S. McDonald, R. B. Lobbia and A. D. Gallimore, "Time-resolved Langmuir Probing of a New Lanthanum Hexaboride (LaB₆) Hollow Cathode," in *32nd International Electric Propulsion Conference*, Wiesbaden, 2011.
- [29] D. M. Goebel and R. M. Watkins, "Compact lanthanum hexaboride hollow cathode," *Review of Scientific Instruments*, vol. 81, p. 083504, 2010.
- [30] L. P. Rand and J. D. Williams, "Instant Start Electride Hollow Cathode," in *33rd International Electric Propulsion Conference*, Washington D.C., 2013.
- [31] M. Nakles, W. A. Hargus, J. Delgado and R. L. Corey, "A Performance Comparison of Xenon and Krypton Propellant on an SPT-100 Hall Thruster," in *International Electric Propulsion Conference*, Weisbaden, 2011.
- [32] A. Shabshelowitz, A. D. Gallimore and P. Y. Peterson, "Performance of a Helicon Hall Thruster Operating with Xenon, Argon and Nitrogen," in *48th AIAA/ASME/SAE/ASEE Joint Propulsion Conference & Exhibit*, Atlanta, 2012.
- [33] V. Hruba, B. Pote, T. Brogan, K. Hohman, J. Szabo and P. Rostler, "Air Breathing Electrically Powered Hall Effect Thruster". United States of America Patent US 6834492 B2, 28 December 2004.
- [34] J. Szabo, M. Robin, J. Duggan and R. R. Hofer, "Light Metal Propellant Hall Thrusters," in *31st International Electric Propulsion Conference*, Ann Arbor, 2009.
- [35] J. G. C. Szabo, V. Hruba and M. Robin, "Bismuth Hall Effect Thruster Development," in *JANNAF Propulsion Conference*, Monterey, 2005.
- [36] J. Szabo, B. Pote, S. Paintal, M. Robin, G. Kolencik, A. Hillier, R. D. Branam and R. E. Huffman, "Performance Evaluation of an Iodine Vapor Hall Thruster," in *47th AIAA/ASME/SAE/ASEE Joint Propulsion Conference & Exhibit*, San Diego, 2011.
- [37] O. S. Tverdokhlebov and A. V. Semenkin, "Iodine Propellant for Electric Propulsion--To Be or Not to Be," in *37th AIAA/ASME/SAE/ASEE Joint Propulsion Conference*, Salt Lake City, 2001.
- [38] R. Dressler, Y.-H. Chiu and D. Levandier, "Propellant Alternatives for Ion and Hall Effects

- Thrusters," in *28th Aerospace Sciences Meeting & Exhibit*, Reno, 2000.
- [39] S. 6. NIST Chemistry WebBook, "U.S. Department of Commerce," [Online]. Available: <http://webbook.nist.gov/chemistry/>.
- [40] S. George and N. Krishnamurthy, "Absorption spectrum of iodine vapor-An experiment," *American Journal of Physics*, vol. 57, no. 9, pp. 850-853, 1989.
- [41] A. C. Hillier, R. D. Branam, R. E. Huffman, J. Szabo and S. Paintal, "High Thrust Density Propellant in Hall Thrusters," in *49th AIAA Aerospace Sciences Meeting including the New Horizons Forum and Aerospace Exposition*, Orlando, 2011.
- [42] J. Szabo and M. Robin, "Plasma Species Measurements in the Plume of an Iodine Fueled Hall Thruster," *Journal of Propulsion and Power*, vol. 30, no. 5, pp. 1357-1367, 2014.
- [43] M. A. Ali and Y.-K. Kim, "Ionization cross sections by electron impact on halogen atoms, diatomic halogen and hydrogen halide molecules," *Journal of Physics B: Atomic, Molecular and Optical Physics*, vol. 41, no. 14, pp. 1-12, 2008.
- [44] "Biagi-v 7.1 (Magboltz version 7.1) database," [Online]. Available: <http://www.lxcat.net>. [Accessed 15 April 2015].
- [45] J. R. Wertz and W. J. Larson, *Space Mission Analysis and Design*, 3rd ed., Hawthorne: Microcosm Press, 1999.
- [46] D. Herman, W. Santiago, H. Kamhawi, J. Polk, J. Snyder, R. Hofer and J. Parker, "The Ion Propulsion System for the Solar Electric Propulsion Technology Demonstration Mission," in *Joint Conference of 30th ISTS, 34th IEPC and 6th NSAT*, Kobe-Hyogo, 2015.
- [47] J. W. Dankanich, M. Walker, M. W. Swaitek and J. T. Yim, "Recommended Practice for Pressure Measurement and Calculation of Effective Pumping Speed," *Journal of Propulsion and Power*, vol. 33, no. 3, pp. 668-680, 2017.
- [48] D. R. Lide, *Handbook of Chemistry and Physics*, 84th Edition ed., CRC Press, 2004.
- [49] L. P. Rand and J. D. Williams, "Instant Start Electride Hollow Cathode," in *33rd International Electrical Propulsion Conference*, Washington D.C., 2013.
- [50] K. M. Alexander and F. Fairbrother, "The Halides of Columbium (Niobium) and Tantalum. Part II. The Vapor Pressure of Tantalum Pentaiodide," *Journal of the Chemical Society*, pp. 2472-2476, 1949.
- [51] H. Kamhawi, T. Haag, G. Benavides, T. Hickman, T. Smith, G. William, J. Myers, K. Polzin, J. Dankanich, L. Byrne, J. Szabo and L. Lee, "Overview of Iodine Propellant Hall Thruster Development Activities at NASA Glenn Research Center," in *52nd AIAA/SAE/ASEE Joint*

Propulsion Conference, Salt Lake City, 2016.

- [52] K. Polzin, S. Peeple, A. Burt, A. Martin, A. Martinez, J. Seixal and S. Mauro, "Development, Demonstration, and Analysis of an Integrated Iodine Hall Thruster Feed System," in *52nd AIAA/SAE/ASEE Joint Propulsion Conference*, Salt Lake City, 2016.
- [53] J. W. Dankanich, M. Shelby, K. A. Polzin, H. Kamhawi, T. Hickman and Byrne, "The iodine satellite (iSat) Project Development towards Critical Design Review (CDR)," in *52nd AIAA/SAE/ASEE Joint Propulsion Conference*, Salt Lake City, 2016.
- [54] F. Chen, *Introduction to Plasma Physics and Controlled Fusion*, vol. 1, New York City, New York: Plenum Press, 1984.
- [55] J. Bittencourt, *Fundamentals of Plasma Physics*, 3rd ed., New York: Springer-Verlag, 2004.
- [56] M. A. Lieberman and A. J. Lichtenberg, *Principles of Plasma Discharges and Materials Processing*, Wiley: Hoboken, 2005.
- [57] J. John and T. Keith, *Gas Dynamics*, 3rd, Ed., Upper Saddle River, New Jersey: Pearson Education, Inc., 2006.
- [58] H. Gould and J. Tobochnik, *Statistical and Thermal Physics*, Princeton: Princeton University Press, 2010.
- [59] W. G. Vincenti and C. H. Kruger Jr., *Introduction to Physical Gas Dynamics*, Malabar: Krieger Publishing Company, 1965.
- [60] R. Shastry, A. D. Gallimore and R. R. Hofer, "Near-Wall Plasma Characterization of a 6-kW Hall Thruster," in *31st International Electric Propulsion Conference*, Ann Arbor, 2009.
- [61] Y. Itikawa, *Molecular Processes in Plasmas: Collisions of Charged Particles with Molecules*, New York: Springer, 2007.
- [62] A. Fridman, *Plasma Chemistry*, Cambridge: Cambridge University Press, 2008.
- [63] D. A. McQuarrie and J. D. Simon, *Physical Chemistry: A Molecular Approach*, Sausalito: University Science Books, 1997.
- [64] A. Moutinho, J. Aten and J. Los, "Temperature dependence of the total cross section for chemi-ionization in alkali halide-galogen collisions," *Physica*, vol. 53, pp. 471-492, 1971.
- [65] D. C. Frost and C. A. McDowell, "Formation of I- Ion from I₂ by Resonance Capture," *Journal of Chemical Physics*, vol. 29, no. 4, pp. 964-965, 1958.
- [66] B. D. Prince, R. J. Bemish and D. J. Levandier, "Application of a First Generation Collisional

Radiative Model for Iodine to Optical Emissions from the Plume of an Iodine Hall Effect Thruster," in *53rd AIAA/SAE/ASEE Joint Propulsion Conference*, Atlanta, 2017.

- [67] T. R. W. R. C. Hayes and R. S. Freund, "Absolute electron-impact-ionization cross section measurements of the halogen atoms," *Phys. Rev. A*, vol. 35, no. 2, p. 578, 1987.
- [68] K. N. Joshipura and C. G. Limbachiya, "heoretical total ionization cross-sections for electron impact on atomic and molecular halogens," *International Journal of Mass Spectrometry*, vol. 216, no. 3, pp. 239-247, 2002.
- [69] P. L. Bartlett and A. T. Stelbovics, "Electron-impact ionization cross sections for elements $Z=1$ to $Z=54$," *Atomic Data and Nuclear Data Tables*, vol. 86, no. 2, pp. 235-265, 2004.
- [70] W. Huo, "NASA website," [Online]. Available: <http://www.ipt.arc.nasa.gov/databasemenu.html>.
- [71] R. Buchdahl, "Negative Ion Formation in Iodine Vapor by Electron Impacts," *Journal of Chemical Physics*, vol. 9, no. 2, pp. 146-152, 1941.
- [72] R. H. Healey, "The behavior of electrons in iodine vapoir," *Philosophical Magazine and Journal of Science*, vol. 26, no. 179, pp. 940-953, 1938.
- [73] M. A. Biondi and R. E. Fox, "Dissociative Attachment of Electrons in Iodine. III. Discussion," *Physical Review*, vol. 109, no. 6, pp. 2012-2014, 1958.
- [74] D. C. Frost and C. A. McDowell, "The Ionization and Dissociation of some Halogen Molecules by Electron Impact," *Canadian Journal of Chemistry*, vol. 38, pp. 407-420, 1960.
- [75] W.-C. Tam and S. F. Wong, "Dissociative attachment of halogen molecules by 0-8 eV electrons," *Journal of Chemical Physics*, vol. 68, no. 12, pp. 5626-5630, 1978.
- [76] J. S. Snyder, "Investigation of the Feasibility of Fullerene Propellant for Ion Thrusters," NASA Technical Report, Jet Propulsion Laboratory, 1998.
- [77] J. R. Anderson and D. Fitzgerald, "Design and Testing of a Fullerene RF Ion Engine," *AIAA-95-2664*, 1995.
- [78] I. Langmiur, "The Pressure Effect and Other Phenomena in Gaseous Discharges," *Journal of the Franklin Institute*, vol. 196, no. 6, pp. 751-762, 1923.
- [79] R. F. Kemp and J. M. Sellen, "Plasma Potential Measurements by Electron Emissive Probes," *Review of Scientific Instruments*, vol. 37, p. 455, 1966.
- [80] J. P. Sheehan, Y. Raitses, N. Hershkowitz, I. Kaganovich and N. J. Fisch, "A comparison of emissive probe techniques for electric potential measurements in a complex plasma," *Physics of Plasmas*, vol. 18, no. 7, pp. 1-9, 2011.

- [81] V. A. Rozhansky and L. D. Tsendin, *Transport Phenomena in Partially Ionized Plasma*, London, New York: Taylor and Francis, 2001, p. 469.
- [82] K. U. Riemann, "Plasma-sheath transition in the kinetic Tonks-Langmuir model," *Physics of Plasmas*, vol. 13, no. 6, pp. 1-13, 2006.
- [83] F. Chen, "Electric Probes," in *Plasma Diagnostic Techniques*, New York, Academic Press, 1965, pp. 113-200.
- [84] G. D. Hobbs and J. A. Wesson, "Heat flow through a Langmuir sheath in the presence of electron emission," *Plasma Physics*, vol. 9, no. 1, 1967.
- [85] J. P. Sheehan, Y. Raites and N. Hershkowitz, "Accurately Determining the Plasma Potential Using Emissive Probes," in *International Electric Propulsion Conference*, Washington D.C., 2013.
- [86] J. P. Sheehan, Y. Raites, N. Hershkowitz and M. McDonald, "Recommended Practice for Use of Emissive Probes in Electric Propulsion Testing," *Journal of Propulsion and Power*, vol. 33, no. 3, pp. 614-637, 2017.
- [87] P. R. Bevington and D. K. Robinson, *Data Reduction and Error Analysis*, New York: McGraw-Hill Higher Education, 2003.
- [88] N. Hershkowitz, "How Langmuir Probes Work," in *Plasma Diagnostics*, vol. 1, O. Abciello and D. L. Flamm, Eds., San Diego, California: Academic Press, Inc., 1989, pp. 113-183.
- [89] J. E. Allen, "Probe Theory--The Orbital Motion Approach," *Physica Scripta*, vol. 45, pp. 497-503, 1991.
- [90] B. Lipschultz, I. Hutchinson, B. LaBombard and A. Wan, "Electric Probes in Plasmas," *Journal of Vacuum Science and Technology A: Vacuum, Surfaces and Films*, vol. 4, no. 3, pp. 1810-1816, 1986.
- [91] H. M. Mott-Smith and I. Langmuir, "The Theory of Collectors in Gaseous Discharges," *Physical Review*, vol. 28, no. 4, pp. 727-763, 1926.
- [92] R. B. Lobbia and B. B. E. Beal, "Recommended Practice for Langmuir Probes in Electric Propulsion Testing," *Journal of Propulsion and Power*, vol. 33, no. 3, pp. 566-581, 2017.
- [93] M. J. Druyvesteyn, "Der Niedervoltbogen," *Zeitschrift fur Physik*, pp. 781-797, 1930.
- [94] Z. C. Lu, J. E. Foster, T. G. Snodgrass, J. H. Booske and A. E. Wendt, "Measurement of electron energy distribution function in an argon/copper plasma for ionized physical vapor deposition," *Journal of Vacuum Science and Technology A: Vacuum, Surfaces and Films*, vol. 17, no. 3, p. 840, 1999.

- [95] K. F. Schoenberg, "Electron distribution function measurement by harmonically driven electrostatic probes," *Review of Scientific Instruments*, vol. 51, no. 9, p. 1159, 1980.
- [96] S. W. Rayment and N. D. Twiddy, "Time-resolved measurements of electron energy distributions," *British Journal of Applied Physics*, vol. 2, no. 2, p. 1747, 1969.
- [97] J. E. Heidenreich III, J. R. Paraszczak, M. Moisan and G. Sauve, "Electron energy distributions in oxygen microwave plasmas," *Journal of Vacuum Science and Technology B*, vol. 6, no. 1, p. 288, 1988.
- [98] H. W. Rundle, D. R. Clark and J. M. Deckers, "Electron Energy Distribution Functions in an O₂ Glow Discharge," *Canadian Journal of Physics*, vol. 51, p. 144, 1973.
- [99] J. D. Swift and M. J. R. Schwar, *Electric Probes for Plasma Diagnostics*, London: Iliffe Books Ltd, 1970.
- [100] K. A. Graf and J. H. De Leeuw, "Comparison of Langmuir Probe and Microwave Diagnostic Techniques," *Journal of Applied Physics*, vol. 38, no. 11, pp. 4466-4472, 1967.
- [101] H. M. J. Kinderdijk and J. Van Eck, "Comparison of Electron Densities Measured with Langmuir Probes and with Two Different Microwave Devices," *Physica*, vol. 59, no. 2, pp. 257-284, 1972.
- [102] L. J. Overzet and M. B. Hopkins, "Comparison of Electron Density Measurements Made Using a Langmuir Probe and Microwave Interferometer in the Gaseous Electronics Conference Reference Reactor," *Journal of Applied Physics*, vol. 74, no. 7, pp. 4323-4330, 1993.
- [103] S. Knappmiller, S. Robertson and Z. Sternovsky, "Comparison of Two Microwave and Two Probe Methods for Measuring Plasma Density," *IEEE Transactions on Plasma Science*, vol. 34, no. 3, pp. 786-791, 2006.
- [104] M. Tuszewski and J. A. Tobin, "The Accuracy of Langmuir Probe Ion Density Measurements in Low-Frequency RF Discharges," *Plasma Sources Science and Technology*, vol. 5, no. 4, pp. 640-647, 1996.
- [105] S. A. Self and C. H. Shih, "Theory and Measurement for Ion Collection by a Spherical Probe in a Collisional Plasma," *Physics of Fluids*, vol. 11, no. 7, pp. 1532-1545, 1968.
- [106] L. H. Brace, "Langmuir Probe Measurements in the Ionosphere," *Measurement Techniques in Space Plasmas: Particles*, pp. 23-35, 1998.
- [107] R. F. Benson, P. Bauer, L. H. Brace, H. C. Carlson, J. Hagen, W. B. Hanson, W. R. Hoegy, M. R. Torr, R. H. Wand and V. B. Wickwar, "Electron and Ion Temperatures--A Comparison of Ground-Based Incoherent Scatter and AE-C Satellite Measurements," *Journal of Geophysical Research, Space Physics*, vol. 82, no. 1, pp. 36-42, 1977.

- [108] M. D. Bowden, M. Kogano, Y. Suetome, T. Hori, K. Uchino and K. Muraoka, "Comparison of Electron Property Measurements in an Inductively Coupled Plasma Made by Langmuir Probe and Laser Thomson Scattering Techniques," *Journal of Vacuum Science and Technology A*, vol. 17, no. 2, pp. 493-499, 1999.
- [109] D. M. Goebel, "Emissive Probe Circuit," October 8, Email to: Blandino, J. (blandino@wpi.edu), 2009.
- [110] D. J. Asselin, *Characterization of the Near-Plume Region of a Low-Current Hollow Cathode*, Worcester: Worcester Polytechnic Institute, 2011.
- [111] V. A. Godyak and V. I. Demidov, "Probe measurements of electron-energy distributions in plasmas: what can we measure and how can we achieve reliable results?," *Journal of Physics D: Applied Physics*, vol. 44, p. 30, 2011.
- [112] V. Kim, "Electric Propulsion Activity in Russia," in *27th International Electric Propulsion Conference*, Pasadena, 2001.
- [113] D. M. Goebel and J. Polk, "Lanthanum Hexaboride Hollow Cathode for the Asteroid Redirect Robotic Mission 12.5 kW Hall Thruster," in *34th International Electric Propulsion Conference*, Hyogo-Kobe, 2015.
- [114] F. F. Chen, "Langmuir Probe Diagnostics, Mini Course of Plasma Diagnostics," in *IEEE International Conference on Plasma Science (ICOPS)*, Jeju, 2003.
- [115] V. A. Godyak and V. I. Demidov, "Probe measurements of electron-energy distributions in plasmas: what can we measure and how can we achieve reliable results?," *Journal of Physics D: Applied Physics*, vol. 44, pp. 1-30, 2011.
- [116] I. G. Mikellides, D. M. Goebel, J. S. Snyder and I. Katz, "Neutralizer Hollow Cathode Simulations and Validation with Experiments," in *45th AIAA/ASME/SAE/ASEE Joint Propulsion Conference*, Denver, 2009.
- [117] D. J. Warner, R. D. Branam and W. A. Hargus Jr., "Ignition and Plume Characteristics of Low-Current Cerium and Lanthanum Hexaboride Hollow Cathodes," *Journal of Propulsion and Power*, vol. 26, no. 1, pp. 130-134, 2010.
- [118] I. H. Hutchinson, "Chapter 3: Plasma Particle Flux," in *Principles of Plasma Diagnostics*, 2nd Edition ed., Cambridge, Cambridge University Press, 2002, pp. 55-103.

Appendix A

Electron Energy Distribution Function – Main Script

```
% Date: 7/18/2013
% Author: Zach Taillefer
% Purpose: Calculate plasma parameters for IonTech Cathode with data
%          collected using KEPCO Bipolar Amp, Measurement Box, Lock-in and
%          NI USB X-Series DAQ.
% Version: R2012a
% Last edited: 12/1/2017
%          by: Zach Taillefer

%clean up
close all; clear all; clc

%% Constants

e = 1.60217646e-19;           %Elementary Charge (Coulombs)
kb = 1.3806503e-23;          %Boltzmann Constant (m^2*kg)/(s^2*K)
epsilon = 8.85418782e-12;    %Permittivity of Freespace
(s^4*A^2)/(m^3*kg)
m_e = 9.10938188e-31;        %Mass of electron (kg)
m_Xe = 2.17975e-25;          %Mass of xenon atom (kg)
Dp = 0.003*0.0254;           %Probe Diameter (m)
Lp = 0.004;                  %Probe Length (m)
Sp = pi*Dp*Lp+pi*Dp^2/4;     %Probe Area (m^2)
rp = Dp/2;                   %Probe Radius (m)
dn = 1.1e-10;                %Covalent diameter of Hydrogen atom (m)

%% Code Controls and Inputs

%plots (1) ON, (0) OFF
PlotData = 1;                %raw data versus time
PlotPeaks = 1;                %test peak detect with plot
PlotSweeps = 0;               %specific sweep or multiple raw sweeps
PlotSweepsInterp = 0;         %specific sweep or multiple interp sweeps
PlotAveragedSweep = 1;        %averaged current and Xsig
PlotLogA2 = 0;                %ln(A)
PlotEEDF = 1;                 %eedf
Maxwellian = 1;               %plot maxwellian over eedf
MaxwellianEnergyShift = 1;
MaxwellianVelocityShift = 1;
Druyvesteyn = 1;
PlotEETF = 0;                 %eetf
IonCurrentFit = 0;            %Ion current fit and electron current
PlotExponentialFit = 1;       %linear fit to exponential region of Ie.
OML = 1;                       %OML fit
ReactionRateCalc = 1;         %preform Cross section fit
PlotCrossSection = 1;         %plot cross section data
PlotCrossSectionFit = 0;      %plot the cross section fit and original data
```



```

%inputs
filename =
char('Collection1a_600_025A_3A_041516.csv');%,'Collection11j_52_cycle3_040616
.csv'); %all files to be analyzed
DeleteSweeps = 1;      %delete single sweeps (1), span (2) or both (3)
Single = 4;           %single sweep to delete
SpanStart = 172;     %first sweep in span to delete (inclusive)
SpanEnd = 187;       %last sweep in span to delete (inclusive)

V_IonSatEnd = 10;     %voltage to stop linear fit of ion saturation region
V_expStart = 27;      %start voltage for exponential region
V_expEnd = 31;        %end voltage for exponential region

Vp_guess = 50;        %guess the plasma potential
Vf_guess = 30;        %guess the floating potential

%output
WriteToFile = 0;      %write outputs to .csv

%% Data Management

[DataSets,~] = size(filename);

%load data
if DataSets == 1
    data = csvread(filename(1,:),1,1);

elseif DataSets == 2
    data1 = csvread(filename(1,:),1,1);
    data2 = csvread(filename(2,:),1,1);

    total = length(data1) + length(data2);
    data = zeros(total,4);
    for r = 1:length(data1)
        data(r,:) = data1(r,:);
    end

    for r = 1:length(data2)
        data(r+length(data1),2:4) = data2(r,2:4);
        data(r,1) = data2(r,1) + data1(length(data1),1);
    end

elseif DataSets == 3
    data1 = csvread(filename(1,:),1,1);
    data2 = csvread(filename(2,:),1,1);
    data3 = csvread(filename(3,:),1,1);

    total = length(data1) + length(data2) + length(data3);
    data = zeros(total,4);
    for r = 1:length(data1)
        data(r,:) = data1(r,:);
    end

    for r = 1:length(data2)

```

```

        data(r+length(data1),2:4) = data2(r,2:4);
        data(r,1) = data2(r,1) + data1(length(data1),1);
    end

    for r = 1:length(data3)
        data(r+length(data1)+length(data2),2:4) = data3(r,2:4);
        data(r,1) = data3(r,1) + data2(length(data2),1);

    end
end
end
%assign raw voltage data
time = data(:,1);
Vvs = data(:,3);
Vcs = data(:,4);
Xsig = data(:,2);

%counter array
count = 1:length(Vvs);

%initialize arrays
voltage = zeros(length(Vvs),1);
current = zeros(length(Vcs),1);

%apply calibration curves from 6/23/15 (Rs = 80ohm)
for i = 1:length(Vvs)
    voltage(i) = 11.192*Vvs(i) - 0.0875;
    current(i) = 23.893*Vcs(i) - 0.1441;
end

Vcs = detrend(Vcs);

Fs = 100000;
T = 1/Fs;
L = length(Vcs);
NFFT = 2^nextpow2(L);
VcsFreq = fft(Vcs,NFFT)/L;
F = Fs/2*linspace(0,1,NFFT/2+1);

figure
plot(F,2*abs(VcsFreq(1:NFFT/2+1)))
xlabel('Frequency (kHz)')
ylabel('|Vcs(f)|')
title('Current Sense in frequency domain')
grid

if PlotData == 1
    figure
    ax(1) = subplot(3,1,1);plot(count,voltage)
    ylabel('Probe Voltage (V)');grid
    ax(2) = subplot(3,1,2);plot(count,current)

```

```

ylabel('Collected Current (mA)');grid
ax(3) = subplot(3,1,3); plot(count,Xsig)
xlabel('Index');ylabel('Xsig (V)');grid

linkaxes(ax,'x');
end

%% Parse the data to extract individual sweeps

voltagePks = smooth(voltage,100); %smooth data for Peak Detect
MinPeakDistance = round((max(voltage) - min(voltage)) - 5);%min distance
between peaks
Vmax = max(voltagePks);           %find max voltage
Vmin = min(voltagePks);           %find min voltage
MinPeakHeightHigh = Vmax - 0.5;   %min peak height for high voltage
MinPeakHeightLow = abs(Vmin + 3); %min peak height for low voltage

%detect peaks
[Maxpks,Maxlocs] = findpeaks(voltagePks,'MINPEAKHEIGHT',MinPeakHeightHigh,...
    'MINPEAKDISTANCE',MinPeakDistance);
[Minpks,Minlocs] = findpeaks(-voltagePks,'MINPEAKHEIGHT',MinPeakHeightLow,...
    'MINPEAKDISTANCE',MinPeakDistance);

if PlotPeaks == 1
    figure
    plot(count,voltagePks); hold on;
    % offset values of peak heights for plotting
    plot(count(Maxlocs),Maxpks+0.05,'k^','markerfacecolor',[1 0 0]);
    plot(count(Minlocs),-Minpks-0.05,'k^','markerfacecolor',[1 0 0]);
end

%initialize arrays for chopping parameters
CountSpan = zeros(1,length(Maxlocs));
DiffSpan = zeros(size(1,length(Maxlocs)));

%ignore first, partial voltage sweep
if Minlocs(1)>=Maxlocs(1)
    Maxlocs(1)=[];
end

%delete partial voltage sweep at end of data collection
voltage(Maxlocs(end):end) = [];

%chop data into sweeps and build arrays
for L = 2:length(Maxlocs)

    CountSpan(L-1) = Maxlocs(L-1) - Minlocs(L-1);
    CountSpan(L) = Maxlocs(L) - Minlocs(L);
    DiffSpan(L-1) = CountSpan(L) - CountSpan(L-1);

    Minlocs(L) = Minlocs(L) + DiffSpan(L-1);

    VoltageSweeps(:,L-1) = voltage(Minlocs(L-1):1:Maxlocs(L-1));
    CurrentSweeps(:,L-1) = current(Minlocs(L-1):1:Maxlocs(L-1));
end

```

```

XsigSweeps(:,L-1) = Xsig(Minlocs(L-1):1:Maxlocs(L-1));

%linear fit for each voltage sweep (eliminate ac flucs in voltage)
Xfit(:,L-1) = 1:1:length(VoltageSweeps(:,L-1));
Yfit(:,L-1) = VoltageSweeps(:,L-1);
P(:,L-1) = polyfit(Xfit(:,L-1),Yfit(:,L-1),1);

%update individual voltage sweeps with linear sweeps
VoltageSweeps(:,L-1) = polyval(P(:,L-1),Xfit(:,L-1));

end

if PlotSweeps == 1;
    for n = 1:6
        figure(n)
        plot(VoltageSweeps(:,n),CurrentSweeps(:,n),'r')
        hold on
        plot(VoltageSweeps(:,n),CurrentSweeps(:,n),'b')
        % axis([-100,100,-5.5e-4,15e-4])
        grid
        xlabel('Probe Bias Voltage (V)')
        ylabel('Current (mA)')
        %         hold on
        %         plot(VoltageSweeps(:,n+200),CurrentSweeps(:,n+200),'r')
    end
end

%% Remove bad sweeps

%single sweep
if DeleteSweeps == 1
    VoltageSweeps(:,Single) = [];
    CurrentSweeps(:,Single) = [];
    XsigSweeps(:,Single) = [];

    %span of sweeps
elseif DeleteSweeps == 2
    VoltageSweeps(:,SpanStart:SpanEnd) = [];
    CurrentSweeps(:,SpanStart:SpanEnd) = [];
    XsigSweeps(:,SpanStart:SpanEnd) = [];

    %single and span
elseif DeleteSweeps == 3
    VoltageSweeps(:,Single) = [];
    CurrentSweeps(:,Single) = [];
    XsigSweeps(:,Single) = [];
    VoltageSweeps(:,SpanStart:SpanEnd) = [];
    CurrentSweeps(:,SpanStart:SpanEnd) = [];
    XsigSweeps(:,SpanStart:SpanEnd) = [];
end

%% Averaging all Sweeps

%generate voltage vector for interp
Vimax = min(max(VoltageSweeps));

```

```

Vimin = max(min(VoltageSweeps));
dV = (Vimax - Vimin)/(length(VoltageSweeps));
Vi = Vimin:dV:Vimax;
Vi = Vi(2:1:length(Vi));

%initialize arrays
Ii = zeros(size(VoltageSweeps));
Xi = zeros(size(VoltageSweeps));

[~,NumSweeps] = size(VoltageSweeps); %for interpt loop

%interpolate current and Xsig
for n = 1:NumSweeps
    Ii(:,n) = interp1(VoltageSweeps(:,n),CurrentSweeps(:,n),Vi,'linear');
    Xi(:,n) = interp1(VoltageSweeps(:,n),XsigSweeps(:,n),Vi,'linear');
end

%plot interpolated sweeps
if PlotSweepsInterp == 1;
    for n = 210:220
        figure(n)
        plot(Vi,Ii(:,n),'-')
        grid
    end
end

%redefine voltage array
V = Vi;

%average all current and Xsig sweeps
I = mean(Ii,2);
A = mean(Xi,2);

%smooth averaged current sweep
%Define a butterworth filter (ninth order low-pass)
[z,p,k]=butter(9,800/10000,'low');
[sos,g]=zp2sos(z,p,k);
Hd=dfilt.df2tsos(sos,g);

Ifiltered = filter(Hd,I);

Ismooth = smooth(V,Ifiltered,400);
dI = diff(Ismooth);
dI = smooth(dI,400);
dI2 = diff(dI);
dI2 = smooth(dI2,300);

%plot averaged current, averaged Xsig and smoothed average current
if PlotAveragedSweep == 1;
    figure
    subplot(2,1,1)
    plot(V,I)

    hold on
    plot(V,Ismooth,'r')%,'LineWidth',1)

```

```

ylabel('Current (mA)')
legend('Averaged Current','Smoothed Average Current','Location','Best')
grid
subplot(2,1,2)
plot(V,A)
hold on
plot(V(3:1:end),dI2*2e4,'r')
ylabel('A')
xlabel('Probe Bias Voltage (V)')
axis([-30 60 -0.5 0.5])
grid
legend('Lock-In Mthd','Numerical','Location','Southwest')

figure
plot(V(2:end),dI)
end

```

```
%% Ion Anaylysis (OML)
```

```
[Ni,X,Y] = DensityOML(I./1000, V, 25, m_Xe, Sp);
```

```
figure
plot(V(V<45), (I(V<45)./1000).^2, '-b');
hold on
plot(X,Y, '-r');
xlabel('Probe Voltage (V)')
ylabel('I^2 (A^2)')
grid

```

```
%% Floating potential
```

```
%find zero crossings
I_zeros = I(1:end-1) .* I(2:end);
IDXf0 = find(I_zeros < 0);
```

```
%find probe voltages at zero crossings
Vf_zeros = V(IDXf0);
%compare guess to probe voltage at all zero crossings
[~,IDXf] = min(abs(Vf_zeros-Vf_guess));
%select probe voltage at zero crossing closest to guess
Vf = Vf_zeros(IDXf);
```

```
%% Plasma Potential
```

```
%~~~~~ Determine zero crossing of second derivative ~~~~~%
```

```
%find zero crossings
A_zeros = A(1:end-1) .* A(2:end);
IDXp0 = find(A_zeros < 0);
```

```
%find probe voltages at zero crossings
Vp_zeros = V(IDXp0);
```

```

%compare guess to probe voltage at all zero crossings
[~,IDXp] = min(abs(Vp_zeros-Vp_guess));

%select probe voltage at zero crossing closest to guess
phi = Vp_zeros(IDXp); %plasma potential

%Te from floating potential (assumes Maxwellian)
Te_float = (phi - Vf)/3.35;

%generate Energy array
E = phi - V;

%define Energy array limits
Emax = 40;
Emin = 0;

%clean up Energy and A arrays
A(E<Emin)=[];
E(E<Emin)=[];
A(E>Emax)=[];
E(E>Emax)=[];

%re-arrange A and E
E = fliplr(E);
A = flipud(A);

%average tail and shift
E_avgCut = Emax - 2;
Tail_Average = mean(A(E>E_avgCut));
A_AvgShift = A + abs(Tail_Average);

figure
plot(E,A,'LineWidth',2)
xlabel('E');ylabel('A just before EEDF calc')
hold on
plot(E,A_AvgShift,'r')
grid

if PlotLogA2 == 1
    A2 = log(A);
    figure
    plot(E,A2)
    grid
end

%% Distribution Function

%function proportional to EEDF
h = sqrt(E).*A';

%normalization constant
H = trapz(E,h);

```

```

%normalized EEDF
g = h./H;

%check normalized EEDF (should = 1)
NormCheck = trapz(E,g);

%Average electron energy
Eavg = trapz(E,E.*g);

%electron temperature
Te = (2/3)*Eavg; % eV

%'shifted' EEDF
hs = sqrt(E).*A_AvgShift';
Hs = trapz(E,hs);
gs = hs./Hs;
Eavgs = trapz(E,E.*gs);
Tes = (2/3)*Eavgs; % eV

%~~~~~ Maxwellian EEDFs ~~~~~%

if Maxwellian == 1;

    dE_Maxwellian = 0.1;
    E_Maxwellian = Emin:dE_Maxwellian:Emax; %energy array [eV]
    Te_Maxwellian = Tes; %electron temperature [eV]

    %calculate energy distribution function
    F = zeros(size(E_Maxwellian));
    for i = 1:length(E_Maxwellian)
        F(i) = (2/((Te_Maxwellian)^(3/2)))*sqrt(E_Maxwellian(i)/pi)...
            *exp(-(E_Maxwellian(i)/Te_Maxwellian));
    end

end

if MaxwellianEnergyShift == 1;

    E_MaxEnergyShift = Emin:0.1:Emax;
    Te_MaxEnergyShift = 2.13;
    del_E = 12.98;

    F_MaxEnergyShift = zeros(size(E_MaxEnergyShift));
    for i = 1:length(E_MaxEnergyShift)
        F_MaxEnergyShift(i) = 8232*(1/pi)*(1/Te_MaxEnergyShift)*...
            exp(-(E_MaxEnergyShift(i)+del_E)/Te_MaxEnergyShift)*...
            (sqrt((E_MaxEnergyShift(i)+del_E)/Te_MaxEnergyShift) -...
            sqrt(del_E/Te_MaxEnergyShift));
    end

end

% Fit Maxwellian with velocity shift to experimental EEDF:

```



```

if MaxwellianVelocityShift == 1;

    % Prepare data to be fit
    [xData, yData] = prepareCurveData( E, gs );

    % Set up fitype and options
    ft = fitype( 'sqrt(1/(pi*Tvs*dE))*exp(-
(xdata+dE)/Tvs)*sinh(2*sqrt(xdata*dE)/Tvs)', 'independent', 'xdata',
'dependent', 'y' );
    opts = fitoptions( 'Method', 'NonlinearLeastSquares' );
    opts.Display = 'Off';
    opts.Lower = [0 0];
    opts.StartPoint = [0.1 0.1];
    opts.Upper = [5 15];

    % Fit model to data.
    [fitresult, gof] = fit( xData, yData, ft, opts );

    E_vs = coeffvalues(fitresult);

    v_drift = sqrt(2*E_vs(2)*e/m_e);
    v_th = sqrt(2*E_vs(1)*e/m_e);
    MachNo = v_drift/v_th;

end

if PlotEEDF == 1
    figure

    % plot(E,g,'LineWidth',1.5)
    plot(E_Maxwellian,F,'-.r')
    hold on
    plot(E,gs,'b')%,'LineWidth',1.5
    %plot(E_MaxEnergyShift,F_MaxEnergyShift,'k')
    plot(fitresult,'--k')
    xlabel('Energy (eV)')
    ylabel('EEDF (eV^-^1)')
    legend('Maxwellian','Experimental','Velocity Shift')

    grid

    axis([0 Emax 0 0.14])
end

%% Probability Distribution Function

gp = (1./sqrt(E)).*g;
gp_log = log(gp);

gp_shift = (1./sqrt(E)).*gs;
gp_log_shift = log(gp_shift);

Fp = (1./sqrt(E_Maxwellian)).*F;

```

```

if PlotEPPF == 1
    figure
    plot(E, gp_log)
    hold on
    plot(E, gp_log_shift, 'r')
    ylabel('log(EPPF)')
    %     axis([0 15 -12 0])
    %     axis autoy
    figure
    %     semilogy(E, gp)
    %     hold on
    semilogy(E_Maxwellian, Fp, 'r')
    hold on

    semilogy(E, gp_shift, 'b')
    ylabel('EPPF (eV-3/2)')
    xlabel('Energy (eV)')
    legend('Maxwellian', 'Experimental')
    grid
end

%% Electron Temperature (Slope Method/Thin Sheath)

%define range for Ion Saturation region
V_Ion = V(V<V_IonSatEnd);
I_IonRaw = I(1:length(V_Ion));

%linear fit for Ion Saturation region
IonFitCoeff = polyfit(V_Ion, I_IonRaw, 1);
I_IonFit = IonFitCoeff(1).*V + IonFitCoeff(2);

%subtract off ion contribution to get electron current
I_Electron = I' - I_IonFit;

%define range for electron temperature fitting
V_slope = V(V>V_expStart & V<V_expEnd);
lnI_Electron = log(I_Electron);
I_slope = lnI_Electron(V>V_expStart & V<V_expEnd);

%linear fit of exponential region
ElectronTempFitCoeff = polyfit(V_slope, I_slope, 1);
ElectronLinearFit = ElectronTempFitCoeff(1)*V + ElectronTempFitCoeff(2);
ExponentialLinearFit = exp(ElectronLinearFit);

%electron temperature (Slope method)
Te_slope = 1/ElectronTempFitCoeff(1);

%plot Ion saturation curvefit and electron current
if IonCurrentFit == 1
    figure
    plot(V, I_IonFit, V, I)
    hold on
    plot(V, I_Electron, 'r')
    xlabel('Probe Voltage (V)'); ylabel('Current (mA)');

```

```

    title('Ion Saturation Fit')
    legend('Ion Current Fit','Raw Probe Current','Electron Current')
    grid
end

%plot linear fit to exponential region
if PlotExponentialFit == 1
    figure
    semilogy(V,I_Electron*1000,V,ExponentialLinearFit*1000);
    xlabel('Probe Voltage (V)');ylabel('Current (mA)')
    legend('I_e','Linear Fit')
end

%% Reaction Rate

if ReactionRateCalc == 1
    %import Cross Section data -- Note: format for the cross section
    %spreadsheet should be as follows --> E1,CS1, E2,CS2, etc.
    filename = 'Xenon Cross Section Data.xlsx';
    Sheet = 'Sheet1';
    Range = 'A4:L201';
    CrossSectionData = xlsread(filename,Sheet,Range);

    E_cs = 0:0.01:Emax; %define overall energy array for interpolation
    Fi = interp1(E_Maxwellian,F,E_cs,'pchip');

    Eidx = zeros(1,length(CrossSectionData(1,:))/2);
    for ii = 1:length(CrossSectionData(1,:))/2
        jj = 2*ii-1;

        %find indices for energy range of interest
        [~,Eidx(ii)] = min(abs(CrossSectionData(:,jj)-Emax));

        %parse Cross Section data
        Ecs{ii} = CrossSectionData(1:Eidx(ii),jj);
        CS{ii} = CrossSectionData(1:Eidx(ii),jj+1);

        %interpolate CS data
        Ei{ii} = E_cs(E_cs > CrossSectionData(1,jj));
        CSi{ii} = interp1(Ecs{ii}(:),CS{ii}(:),Ei{ii}(:),'pchip');
    end

    if PlotCrossSection == 1
        figure
        semilogy(CrossSectionData(:,1:2:end),CrossSectionData(:,2:2:end),'.-')
        axis([0 Emax 10^-29 10^-17])
        title('Electron-Xenon Cross Sections')
        ylabel('\sigma (m^2)')
        xlabel('Energy (eV)')
    end
end

```

```

legend('Elastic', 'Xe^(8.315)', 'Xe^(9.447)', 'Xe^(9.917)', ...
      'Xe^(11.7)', 'Xe^(12.13)', 'Location', 'Best')
grid

if PlotCrossSectionFit == 1
    hold on
    for iii = 1:length(Ei)
        semilogy(Ei{iii}(:), CSi{iii}(:), '-k')
    end
end

end

%calculate reaction rates
gi = gs/e;
Fi = Fi/e;
for mm = 1:length(Ecs)
    RxRate{mm} = ReactionRate(Ei{mm}(:), gi, CSi{mm}(:));
    %reaction rates with maxwellian eedf
    RxRate_Maxwellian{mm} = ReactionRate(Ei{mm}(:), Fi, CSi{mm}(:));
end

end

%% Output relevant values to CW

clc; %clear the negative data warnings from Te Slope method log plot

disp(['Te (raw) = ', num2str(Te), ' eV'])
disp(['Te (vert shift) = ', num2str(Tes), ' eV'])
disp(['Te (slope) = ', num2str(Te_slope), ' eV'])
disp(['Te (Vf) = ', num2str(Te_float), ' eV'])
disp(['Te (vel shift) = ', num2str(E_vs(1)), ' eV'])
disp(['dE (vel shift) = ', num2str(E_vs(2)), ' eV'])
disp(' ')
disp('Velocities: ')
disp(['v_e (drift vel) = ', num2str(v_drift*10^-3), ' km/sec'])
disp(['v_th (thermal vel) = ', num2str(v_th*10^-3), ' km/sec'])
disp(['Mach No = ', num2str(MachNo)])
disp(' ')
disp(['Vp = ', num2str(phi), ' V'])
disp(['Vf = ', num2str(Vf), ' V'])
disp(' ')
if ReactionRateCalc == 1
    disp('Reaction rates:')
    disp(['elastic = ', num2str(RxRate{1}), ' m^3/sec'])
    disp(['excite (8.315) = ', num2str(RxRate{2}), ' m^3/sec'])
    disp(['excite (9.447) = ', num2str(RxRate{3}), ' m^3/sec'])
    disp(['excite (9.917) = ', num2str(RxRate{4}), ' m^3/sec'])
    disp(['excite (11.7) = ', num2str(RxRate{5}), ' m^3/sec'])
    disp(['ionization (12.13) = ', num2str(RxRate{6}), ' m^3/sec'])
    disp(' ')
end

```

```
disp('Reaction rates (Maxwellian):')
disp(['elastic = ', num2str(RxRate_Maxwellian{1}), ' m^3/sec'])
disp(['excite (8.315) = ', num2str(RxRate_Maxwellian{2}), ' m^3/sec'])
disp(['excite (9.447) = ', num2str(RxRate_Maxwellian{3}), ' m^3/sec'])
disp(['excite (9.917) = ', num2str(RxRate_Maxwellian{4}), ' m^3/sec'])
disp(['excite (11.7) = ', num2str(RxRate_Maxwellian{5}), ' m^3/sec'])
disp(['ionization (12.13) = ', num2str(RxRate_Maxwellian{6}), ' m^3/sec'])
end
```

ReactionRate.m

```
function [ RxRate ] = ReactionRate( Energy, DistFunc, CS_fit )
%The function ReactionRate calculates the reaction rate constant for a
%given species for a given excitation state.

% INPUTS:
% Energy      --> energy array for cross section fit
% DistFunc    --> distribution function (J^-1)
% CS_fit      --> Cross Section fit

%OUTPUTS:
% RxRate      --> Reaction rate constant

e = 1.60217646e-19;           %Elementary Charge (Coulombs)
m_e = 9.10938188e-31;       %Mass of electron (kg)
dE = 0.01;                  %step size for integration
E = Energy;
RxRate = 0;                  %initialize integral

for i = 1:length(E)
    [b,m,~] = unique(E);
    F = interp1(b,DistFunc(m),E(i),'pchip');
    RxRate = RxRate + dE*e*CS_fit(i)*F*sqrt(2*E(i)*e/m_e);
end

end
```

Plasma Potential – Main Script

```
clear all; clc; close all;

%Load the preamble and waveform files
data=load(['Waveform4_Ch1.txt']);
preamble=load(['Preamble4_Ch1.txt']);

%Store plotting parameters
xzero=preamble(1,1);
xincr=preamble(2,1);

yzero=preamble(3,1);
ymult=preamble(4,1);
yoff=preamble(5,1);

Fs= 1/xincr; %2.5e9; %Sampling frequency

time=zeros(length(data),1);
voltage=zeros(length(data),1);

%Calculate time and voltage from raw waveform data
for i=1:length(data)
    time(i)=xzero+xincr*i;
end

for i=1:length(data)
    voltage(i)=yzero+ymult*(data(i)-yoff);
end

%calibration curve from 7/2/14
for j = 1:length(voltage)
    voltage(j) = 11.061*voltage(j) + 1.4226;
end

Vmean = mean(voltage);
Vmin = min(voltage);
Vmax = max(voltage);

dV = abs(Vmax - Vmin);
dVmean = dV/Vmean;

disp(['dV = ' num2str(dV) ' V'])
disp(['Vmean = ' num2str(Vmean) ' V'])
disp(['dV/Vmean = ' num2str(dVmean)])

%Plot voltage
figure(1)
plot(time,voltage)
title('Probe Voltage vs. Time')
```

```

xlabel('Time (s)')
ylabel('Voltage (V)')
grid

%Calculate frequency spectrum
N=length(voltage); %Number of samples
T=N/Fs; %Total time length of record
df=1/T; %Frequency resolution
F=0:df:Fs-df; %Frequency vector

%Calculate frequency spectrum
%Fs=1000000;
NFFT = 2^nextpow2(length(voltage)); % Next power of 2 from length of voltage
figure(2)
%Periodogram
periodogram(voltage, [],NFFT,Fs);

%remove offset
voltage = detrend(voltage);

Vrms = rms(voltage);
disp(['Vrms = ' num2str(Vrms) ' V'])

figure(3)
V=fft(voltage); %Fourier transform of the voltage signal
PSD=1/(Fs*N)*abs(V).^2; %PSD power spectral density function

F = F/1000; % frequency Hz --> kHz
plot(F,PSD) %Could also do this as a loglog plot
xlabel('Frequency (kHz)')
ylabel('|V(f)|')
% hold on;
% % offset values of peak heights for plotting
% plot(F(freqs),pks+0.000000005,'k^','markerfacecolor',[1 0 0]);
axis([0 F(0.5*length(F)) 0 150])
axis autoy
grid

```

Appendix B

This section describes the setting up the lock-in amplifier, recommended settings, how to detect the second harmonic of the superimposed ac signal and some general recommendations regarding use and

acquiring reliable measurements. It is recommended to try this with a dummy circuit with known second derivative representing the plasma such as a resistor and Zener diode.

Set up the lock-in amplifier, signal generator, measurement circuit, etc. according the schematic below and described in Section 4.2.

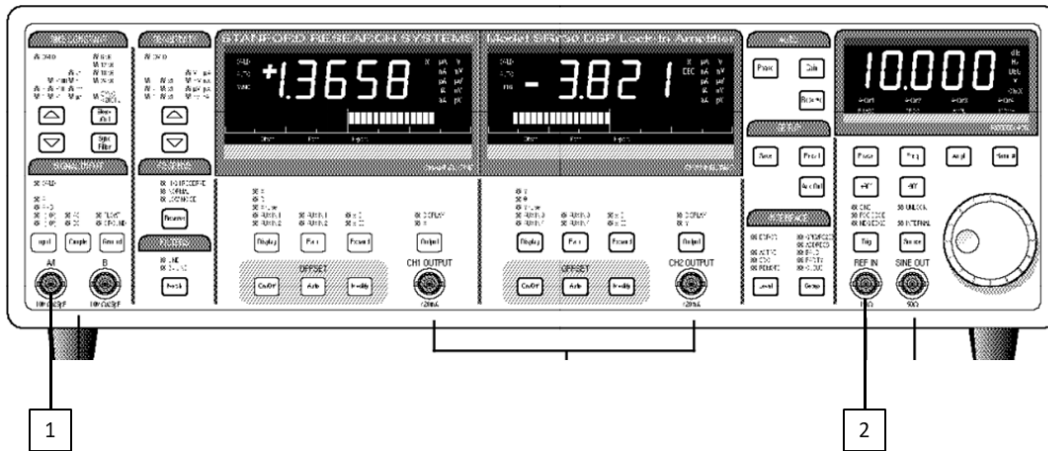


Figure 79: Lock-in amplifier front panel

Connect the “Current Sense” output from measurement circuit box to #1, “A/I Input”. Connect the TTL output from signal generator (ac signal generator) to #2, “Ref IN”.

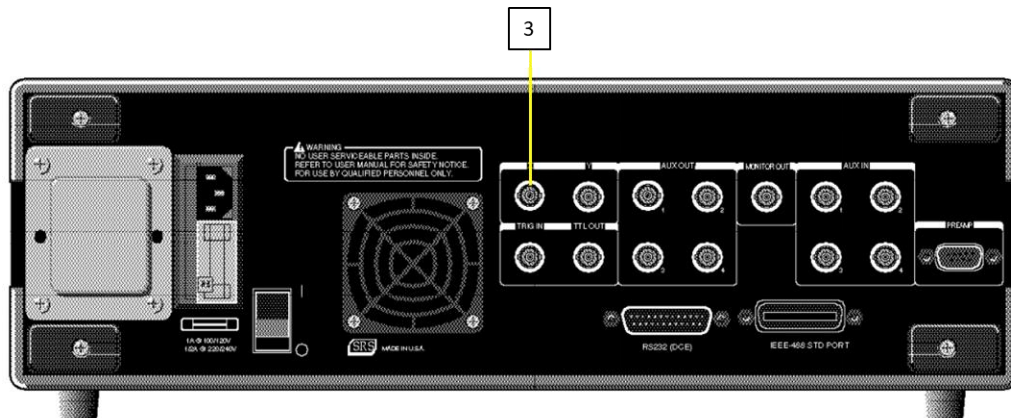


Figure 80: Lock-in amplifier rear panel

Connect #3, “X Output”, from the rear panel of the lock-in amplifier to the DAQ. (This is the signal proportional to the second derivative of the probe current.) It is recommended to tee into this signal and display it on the oscilloscope.

Set the input to “A” and “DC Coupled”.

Start the Langmuir probe trace by turning on both signal generators.

The Lock-in amp should confirm the ac signal is coupled when the “unlock” light is not illuminated. Press “Freq” to display the ac signal frequency on the “Reference” read out (digital display on the RHS). Adjust the ac signal frequency on at the signal generator if necessary. Press “Harm #” to display the harmonic number. Turn the number until the harmonic number changes to “2”. (Option: press Freq to display the ac signal frequency again.)

Reduce the “Slope/Oct” to 24 dB and turn on “SYNC < 200 Hz” and monitor the signal on the oscilloscope. With each reduction in the time constant the second derivative signal will become more clear. Proceed to reduce the “Time Constant” until the signal distorts and return to the previous time constant setting. The distortion mentioned here will be evident by a distinct change in the signal. It will change from a low noise signal closely resembling the second derivative to a signal with large amplitude high frequency noise. This will make the cutoff frequency the lowest value possible without distorting the second derivative signal.

Increase the “Sensitivity” if necessary to increase the signal magnitude.